

**Probing Transition Metal Dichalcogenide
Monolayers and Heterostructures by Optical
Spectroscopy and Scanning Tunneling
Spectroscopy**

Heather M. Hill

Submitted in partial fulfillment of the
requirements for the degree
of Doctor of Philosophy
in the Graduate School of Arts and Sciences

COLUMBIA UNIVERSITY

2016

©2016

Heather M. Hill

All Rights Reserved

Abstract

Probing Transition Metal Dichalcogenide Monolayers and Heterostructures
by Optical Spectroscopy and Scanning Tunneling Spectroscopy

Heather M. Hill

Atomically thin two-dimensional materials, such as graphene and semiconductor transition metal dichalcogenides (TMDCs), exhibit remarkable and desirable optical and electronic properties. This dissertation focuses on the excitonic properties of monolayer TMDCs taken first in isolation and then in contact with another material.

We begin with a study of the exciton binding energy in two monolayer TMDCs, WS_2 and MoS_2 . We observe excited states of the exciton by two different optical spectroscopy techniques: reflectance contrast and photoluminescence excitation (PLE) spectroscopy. We fit a hydrogenic model to the energies associated with the excited states and infer a binding energy, which is an order of magnitude higher than the bulk material.

In the second half of this work, we study two types of two-dimensional vertical heterostructures. First, we investigate heterostructures composed of monolayer WS_2 partially capped with graphene one to four layers thick. Using reflectance contrast to measure the spectral broadening of the excitonic features, we measure the decrease in the coherence lifetime of the exciton in WS_2 due to charge and energy transfer when in contact with graphene. We then compare our results with the exciton lifetime in MoS_2/WS_2 and $\text{MoSe}_2/\text{WSe}_2$ heterostructures. In TMDC/TMDC heterostructures,

the decrease in exciton lifetime is twice that in WS₂/graphene heterostructures and due predominantly to charge transfer between the layers.

Finally, we probe the band alignment in MoS₂/WS₂ heterostructures using scanning tunneling microscopy (STM) and spectroscopy (STS). We confirm the monolayer band gaps and the predicted type II band alignment in the heterostructure. Drawing from all the research presented, we arrive at a favorable conclusion about the viability of TMDC based devices.

Contents

List of Figures	v
1 Introduction to TMDCs and Graphene	1
1.1 Physical Structure	1
1.1.1 Chemical Components	2
1.1.2 Lattice Structure	2
1.2 Band Structure	5
1.3 Optical Response in TMDCs and Graphene	7
1.3.1 Raman Scattering	7
1.3.2 Linear Absorption	12
1.3.3 Photoluminescence in TMDCs	15
2 Experimental Techniques	17
2.1 Raman Spectroscopy	17
2.1.1 Concept	18
2.1.2 Experimental Setup	19
2.2 Reflectance Contrast	21
2.2.1 Reflectance Contrast and Absorption	21

2.2.2	Experimental Setup	21
2.2.3	Measurement Procedure	22
2.3	Photoluminescence Spectroscopy	23
2.3.1	Photoluminescence in Semiconductors	23
2.3.2	Experimental Setup	24
2.4	Photoluminescence Excitation Spectroscopy	25
2.4.1	Concept	25
2.4.2	Experimental Setup	26
2.4.3	Measurement Procedure	27
2.5	STM and STS	28
2.5.1	Concept	28
2.5.2	Experimental Setup	29
2.5.3	Data Processing	29
3	Exciton Binding Energy in Monolayer MoS₂ and WS₂	30
3.1	Modeling the Exciton	30
3.1.1	Hydrogenic Model	31
3.1.2	Nonlocal Screening Model	33
3.2	Experimental Observation	36
3.2.1	Reflectance Contrast of TMDCs	37
3.2.2	Reflectance Contrast of WS ₂	40
3.2.3	PLE of TMDCs	45
3.3	Conclusions	57
3.3.1	Summary	57
3.3.2	Comparison with Other Works	57

3.3.3	Impact and Future Work	60
4	Interlayer Interactions in WS₂/Graphene Heterostructures	61
4.1	Samples	62
4.2	Experimental Results	62
4.2.1	Photoluminescence Quenching	64
4.2.2	Raman Spectroscopy of Graphene	66
4.2.3	Reflectance Contrast of WS ₂ /Graphene Heterostructures . . .	68
4.2.4	Graphene Thickness Dependence	74
4.2.5	Reflectance Contrast of TMDC/TMDC Heterostructures . . .	75
4.3	Sources of Broadening	77
4.3.1	Energy Transfer	78
4.3.2	Charge Transfer	80
4.4	Conclusions	81
5	Scanning Tunneling Microscopy and Spectroscopy of MoS₂/WS₂ Heterostructures	82
5.1	Samples	83
5.1.1	Sample Preparation	83
5.2	STS Model	86
5.2.1	Model of Tunneling Current	87
5.2.2	Thermal Broadening	90
5.2.3	Tip-Induced Band Bending	91
5.3	Experimental Results	91
5.3.1	STM Results	92

5.3.2	STS Results	92
5.3.3	Band Alignment	96
5.4	Conclusions	98
5.4.1	Summary	98
5.4.2	Comparison with Other Works	99
5.4.3	Impact and Future Work	99
6	Conclusion	101
6.1	Summary	101
6.2	Ongoing and Future Experiments	103
6.2.1	Dielectric Environment and Binding Energy	103
6.2.2	Charge vs. Energy Transfer in Heterostructures	104
6.2.3	Interlayer Excitons	104
6.2.4	Other Layered Materials	105
6.3	Final Remarks	105
	Bibliography	107
	Appendix A Effective Mass Approximation	118
	Appendix B Polymer Transfer Technique	120

List of Figures

1.1	Periodic table	3
1.2	Qualitative image of the lattice structure of graphene	3
1.3	Qualitative image of the lattice structure of TMDCs	4
1.4	Band structure of monolayer graphene and bulk MoS ₂	5
1.5	Layer dependence of the Raman modes of graphene	8
1.6	Raman spectroscopy of MoS ₂	9
1.7	Raman spectroscopy of WS ₂	10
1.8	Raman spectroscopy of MoSe ₂	11
1.9	Raman spectroscopy of WSe ₂	12
1.10	Optical absorption of monolayer graphene	13
1.11	Optical absorption of monolayer TMDCs	14
1.12	Photoluminescence of monolayer TMDCs	15
1.13	Photoluminescence of MoS ₂ as a function of sample thickness	16
2.1	Qualitative image of Stokes and anti-Stokes Raman scattering	19
2.2	Schematic depiction of a Raman spectroscopy setup	20
2.3	Schematic depiction of a reflectance contrast setup	22

2.4	Qualitative depiction of photoluminescence in semiconductors	24
2.5	Schematic depiction of a photoluminescence spectroscopy setup	25
2.6	Schematic depiction of a photoluminescence excitation setup	27
3.1	Qualitative depiction of the interaction between an electron and hole in a 2D layer	33
3.2	Table of calculated TMDC exciton parameters	36
3.3	Qualitative graph of the absorption from a semiconductor with excitons	38
3.4	Absorption spectrum of monolayer MoS ₂	39
3.5	Derivative of the reflectance contrast spectrum of monolayer WS ₂	41
3.6	Transition energies of the excited states of the monolayer WS ₂ A exciton	43
3.7	Thickness dependence of the band gap and exciton binding energy in WS ₂	44
3.8	PLE, absorption, and relative QE of monolayer MoS ₂ and WS ₂	46
3.9	Power and sample dependence of PL and PLE	48
3.10	Absorption, PLE, and relative QE for monolayer MoS ₂ on BN	49
3.11	PLE of monolayer WS ₂	51
3.12	PLE and derivative of the reflectance contrast of monolayer WS ₂	51
3.13	Excited exciton transition energies in monolayer MoS ₂ from PLE and from theory	52
3.14	Experimental and theoretical transition energies for the alternate as- signment of the Rydberg series of monolayer MoS ₂	55
3.15	Lorentzian fits to the PLE of monolayer MoS ₂	56
4.1	Schematic depiction of the polymer transfer technique	63

4.2	Quenching of monolayer WS ₂ PL when capped with graphene	64
4.3	Raman spectroscopy of graphene in WS ₂ /graphene heterostructures	66
4.4	Change in the peak position and width of the Raman modes of graphene in WS ₂ /graphene heterostructures	67
4.5	Low temperature reflectance contrast of a WS ₂ /graphene heterostructure	68
4.6	Room temperature reflectance contrast of a WS ₂ /graphene heterostructure	69
4.7	Calculated reflectance contrast of a WS ₂ /graphene heterostructure	70
4.8	Summed individual layer and heterostructure reflectance contrast of a WS ₂ /graphene heterostructure	71
4.9	Derivative of the reflectance contrast of monolayer WS ₂ and the heterostructure	72
4.10	Heterostructure reflectance contrast and the summed individual layer reflectance contrast convoluted with a Lorentzian	73
4.11	Redshift of the WS ₂ A and B exciton reflectance contrast peaks in the heterostructure	74
4.12	Broadening of the WS ₂ A and B exciton reflectance contrast peaks in the heterostructure	75
4.13	Reflectance contrast of TMDC/TMDC heterostructures	76
4.14	Relative energy transfer rate for monolayer WS ₂ on graphene	79
5.1	Optical image and schematic depiction of the STM/STS samples	84
5.2	AFM image of a MoS ₂ /WS ₂ heterostructure	85
5.3	Schematic depiction of the process used to create gold contacts on our STM/STS samples	86

5.4	Region of the STS data to which the tunneling current model is fitted	89
5.5	Parameters used for tip-induced band bending calculations	92
5.6	STM image of monolayer WS ₂	93
5.7	Monolayer and heterostructure STS experimental data	94
5.8	Experimental band gaps and band alignment in MoS ₂ /WS ₂ heterostructures	97
B.1	Schematic depiction of exfoliating onto PPC for the polymer transfer technique	121

Acknowledgments

This dissertation never could have happened without the help and support of so many people. First, I might never have become interested in physics without the enthusiasm that Dr. Neznanski brought to class every day at Bishop Kelly High School. I appreciate Prof. Daniel Gauthier encouraging me to pursue experimental physics as my undergraduate advisor at Duke University. Special thanks to the Columbia Physics Department administrators: Michael Adan, Joey Cambareri, Randy Torres, and Yasmin Yabyabin. Additionally, my research never could have happened if not for the financial support from the NSF IGERT Graduate Fellowship.

I am honored to have collaborated with Prof. Jim Hone, Prof. David Reichman, Dr. Mark Hybertsen, and Prof. Louis Brus. Particular thanks to my graduate advisor, Prof. Tony Heinz. An additional thank you to all my post-doctoral collaborators: Cyrielle Roquelet, Alexey Chernikov, Tim Berkelbach, Kika Ernst, Claudia Ruppert, Arend van der Zande, Ghidewon Arefe, Yilei Li, and Kwang Taeg Rim. Finally, I could not have accomplished these research goals without the companionship and advice of: Ozgur Burak Aslan, Archana Raja, Albert Rigosi, Suk Hyun Kim, and all the other Heinz group members with whom I did not have an opportunity to collaborate directly.

On a personal note, I have been so lucky to have some of the most amazing friends including Ashina Sipiora, Amanda Smith, Allie Morgan, Lauren Bratney, Bryndl Barter, Greg McGlynn, Catherine Lee, and Molly Cooper. Thank you to my entire extended family especially Uncle Craig and Aunt Dorothy, Uncle Gary and Aunt Marie, Uncle Duncan and Aunt Pam, Uncle Jeff and Aunt Brenda, Great Aunt Mary, and Aunt Karen and Uncle Sam. To my fiancé, Albert Rigosi, your love,

support, and research collaboration has been beyond integral to my research, my graduate school experience, and my life. Finally, I cannot thank my family enough: my brother, Grant Hill, and my incomparable parents, Nancy and William Hill. Mom and Dad, your love and encouragement have made me who I am.

Dedicated to my wonderful family: Grant, Nancy, and William Hill

Chapter 1

Introduction to TMDCs and Graphene

In this chapter, we will discuss some of the basic properties of transition metal dichalcogenides (TMDCs) and graphene. These properties include the physical structure of the lattice, the chemical components, the band structure, and some fundamental optical properties, namely Raman modes, absorption, and photoluminescence. This chapter will give all the necessary ground work to understand the remainder of this dissertation.

1.1 Physical Structure

Since the first isolation of a single layer of graphene [1], many of its remarkable physical and electronic properties have been documented (see Chapter 1 Sections 2.1 and 3). Building off of the incredible success of graphene, a whole host of quasi-two-dimensional materials have become the focus of much theoretical and experimental

investigation. Transition metal dichalcogenides, one such class of layered 2D materials, will be our primary focus.

In this section we will describe the physical structure of TMDCs and graphene. First, we will briefly review the chemical components of TMDCs and graphene. We will then explain the lattice structure of both materials.

1.1.1 Chemical Components

The term transition metal generally refers to elements in the “d-block” of the periodic table, thus named because the highest energy electrons reside in the d-orbital. In Figure 1.1, transition metals are indicated on the periodic table by a dark blue outline, with molybdenum and tungsten outlined in cyan. The atomic number for molybdenum and tungsten are 42 and 74, respectively. Chalcogens, also known as the oxygen family, are group 16 of the periodic table. In Figure 1.1, chalcogens are indicated on the periodic table by a red outline, with sulfur and selenium outlined in pink. Sulfur and selenium have atomic numbers 16 and 34, respectively. Additionally, carbon, the atom that comprises graphene, is marked in green and has atomic number 6. Transition metal dichalcogenides (TMDCs) have the general chemical formula MX_2 [2], where M can be either molybdenum, Mo, or tungsten, W, and X either sulfur, S, or selenium, Se.

1.1.2 Lattice Structure

Graphene is a hexagonal honeycomb lattice of carbon that is one atom thick [3], see Figure 1.2. Each carbon atom is covalently bonded with its three nearest neighbors, with one loose bond out-of-plane [4]. The distance between adjacent carbon atoms

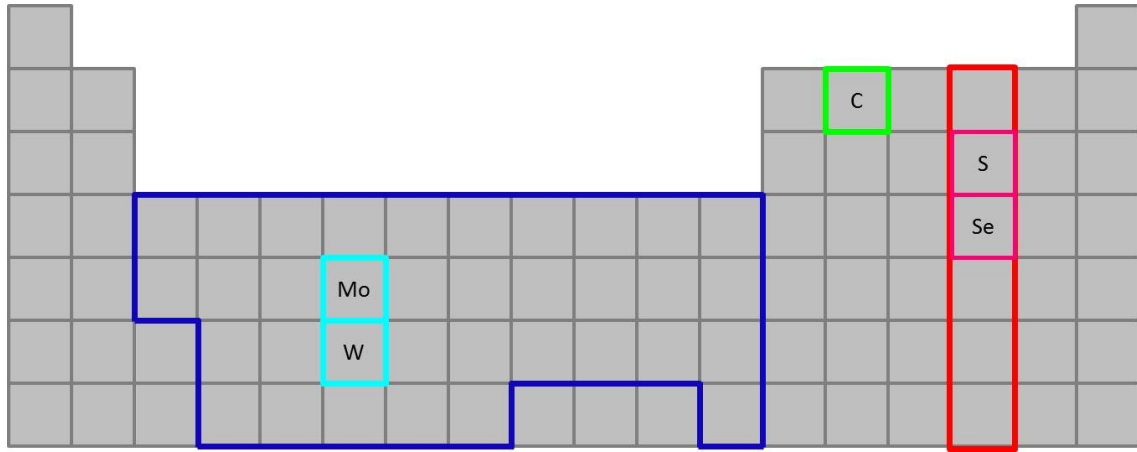


Figure 1.1: Simplified periodic table. Transition metals are outlined in dark blue, with molybdenum and tungsten outlined in cyan. Chalcogens are outlined in red, with sulfur and selenium outlined in pink. Carbon is also outlined in green.

is approximately 1.42 \AA [4]. In thicker samples, the individual layers of are bonded to one another by weak van der Waals interactions [1]. These weak interlayer bonds allow for layers to be readily cleaved through methods such as mechanical exfoliation.

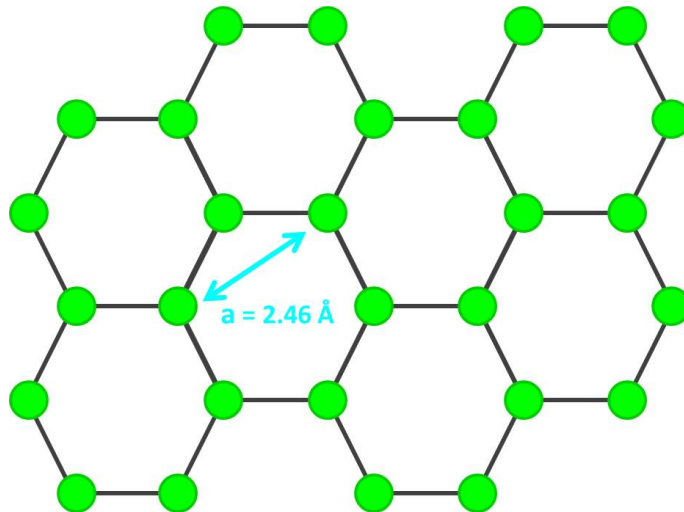


Figure 1.2: Qualitative image of the lattice structure of graphene. The green dots represent carbon atoms, and the lattice constant, a , is labeled.

Viewed from above, TMDCs are also a hexagonal honeycomb lattice composed of alternating M type (transition metal) and X type (chalcogen) atoms, see Figure 1.3. However, any lattice point seemingly filled by a single chalcogen atom is actually two chalcogen atoms one atop the other in a trigonal prismatic configuration. The spacing between the stacked chalcogens is about 3.11 \AA [5]. A top and side view of the lattice are shown schematically in Figure 1.3, with the transition metal atoms in blue and the chalcogen atoms in red.

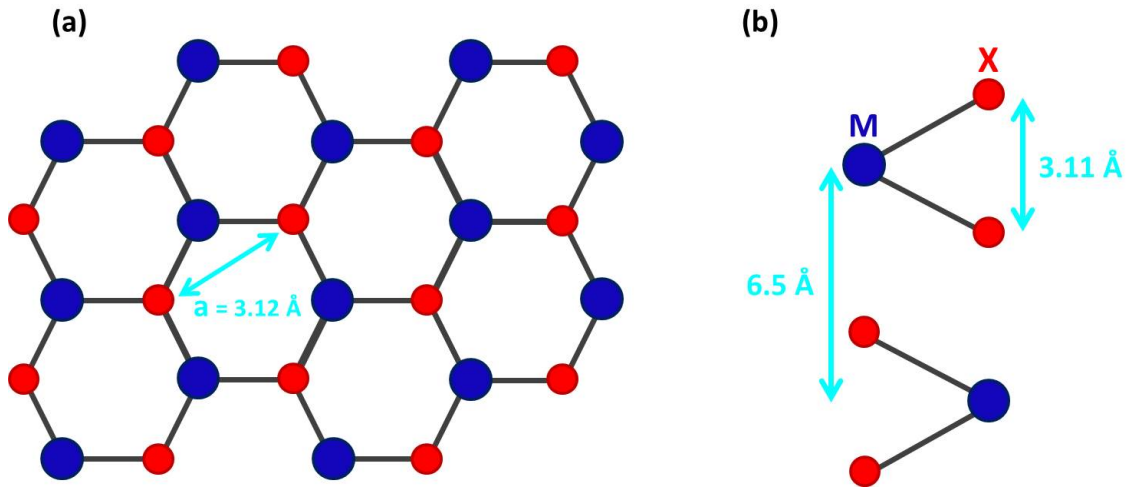


Figure 1.3: Qualitative image of the lattice structure of TMDCs. The blue dots represent the transition metal atoms, and the red dots represent the chalcogen atoms. **(a)** The lattice viewed from above. The lattice constant, a , is labeled. **(b)** The lattice viewed from the side for a bilayer TMDC. The interlayer spacing and the distance between chalcogen atoms are both labeled.

In thicker TMDCs, individual layers are held to one another by van der Waals forces, much like graphene [6]. The layers are oriented in 2H stacking [7], *i.e.* the chalcogens of one layer are aligned with the transition metal of the next layer (see Figure 1.3(b)). The interlayer spacing has been measured to be 6.5 \AA [8].

1.2 Band Structure

Calculating the energy of the lattice as a function of k , reciprocal space or lattice momentum, can be done in a few different ways. One option is the tight-binding model. Another prevalent method is computational density functional theory (DFT). For our purposes the details of these calculations are not essential; it is sufficient that these calculations can be done with reasonable levels of accuracy. In this section, we will present the band structure of graphene and MoS₂. We will also discuss some general properties of the band structure in semiconductors.

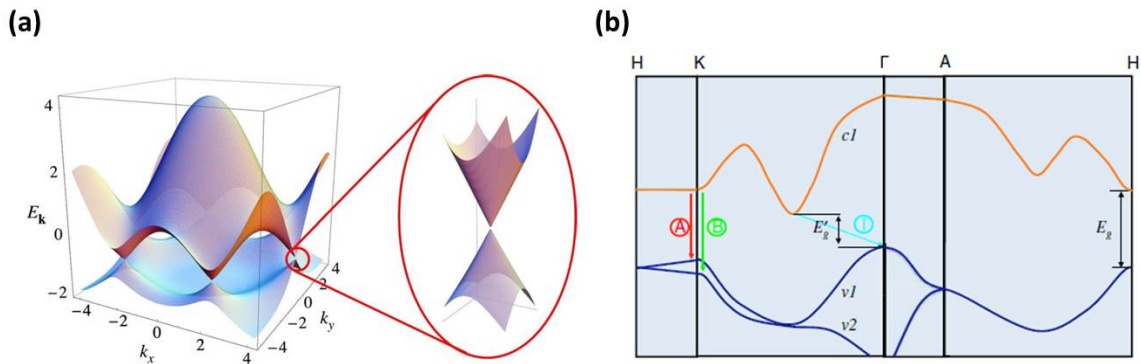


Figure 1.4: Band structure of monolayer graphene and bulk MoS₂. **(a)** The band structure of monolayer graphene, from [9], with a magnified view of the K-point. **(b)** Simplified band structure of bulk MoS₂, from [6].

In Figure 1.4 we provide the band structure of monolayer graphene and bulk MoS₂. We will give a more detailed discussion of the band structure of TMDCs in later sections and chapters. For now, we will focus predominantly on properties common to all band structures, using the information provided in [10].

The lower band is called the valence band, and, in an undoped sample, this band is filled with electrons. The conduction (upper) band is empty in an undoped

sample. The electrons in the valence band have limited movement within the band as all of the energy states are filled. Electrons in the conduction band are able to move fairly easily as the majority of the band is unfilled.

The band structure reveals the available transitions between the valence and conduction bands. If we look at the band structure of graphene, the conduction band and valence bands connect at the K-point, *i.e.* graphene is a semimetal. This Dirac cone allows electrons to move from the valence to conduction band quite easily. Generally, transitions can be made between any valence band local maximum and any conduction band local minimum. A few such transitions are indicated by arrows in the band structure of MoS₂. A direct transition, such as the transitions marked A and B in Figure 1.4(b), occurs between a valence band maximum and a conduction band minimum at the same point in k -space. An indirect transition, like the transition labeled I in MoS₂, occurs between a maximum and minimum at different points in k -space. Direct transitions are favorable, because they do not require phonons (lattice vibrations).

The band gap of a material is the energy difference between the valence band maximum and conduction band minimum. Generally, a material with a band gap, E_g , that takes the values $0 \text{ eV} < E_g \leq 4 \text{ eV}$ is called a semiconductor. If the lowest energy transition is a direct transition, it is called a direct-gap semiconductor. Similarly, if the lowest energy transition is an indirect transition, it is called an indirect-gap semiconductor. If the band gap is larger than 4 eV, the material is called an insulator.

The band structure dictates quite a few of the optical properties. For this reason, it is important to understand the band structure before we delve into the specific optical properties of TMDCs.

1.3 Optical Response in TMDCs and Graphene

In this section, we will discuss the basic optical properties of TMDCs and graphene. Specifically, we will review the Raman scattering and linear absorption of monolayer, few-layer, and bulk TMDCs and graphene. We will also examine the layer dependence of the photoluminescence in TMDCs. These optical properties are essential to the work investigated in depth in this dissertation. However, there are many other fascinating optical properties that will, sadly, not be covered, *e.g.* second harmonic generation, valley-spin coupling, *etc.*

1.3.1 Raman Scattering

The Raman spectrum of a material gives insight into the vibrational modes of the material. The Raman modes in graphene are often used to characterize the thickness of few-layer samples [11], since the modes are quite sensitive to the number of layers. The three important Raman peaks are the D, G, and 2D peaks; the G and 2D features are shown in Figure 1.5. In monolayer graphene, the G and 2D peaks occur at 1587 cm^{-1} and 2658 cm^{-1} , respectively. The D peak is often known as the defect peak, and its presence is an indication of inhomogeneities and residue on the sample [11]. With increasing layer number, the G peak increases in magnitude, while the 2D decreases in height, broadens, and blueshifts. An easy metric for determining the thickness of a few-layer graphene sample is the ratio of the intensity of the G and 2D peaks. The G to 2D ratio is about 1:2 for monolayer [12], 1:1 for bilayer, and 2:1 for trilayer. The graphene Raman spectra are shown in Figure 1.5 for monolayer, bilayer, trilayer, and a thicker few-layer sample.

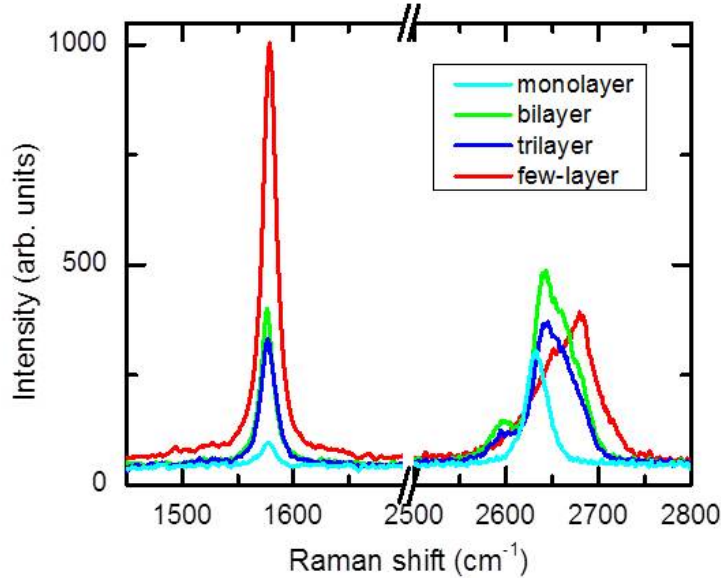


Figure 1.5: Layer dependence of the Raman modes of graphene. The peak on the left is the G mode, and the right is the 2D mode. The Raman spectra are shown for monolayer, bilayer, trilayer, and a thicker few-layer sample of about 5 layers thick.

The Raman modes in TMDCs have been thoroughly measured and reported [13, 14, 15]. We will begin with the Raman modes of MoS_2 and then address the similarities and differences amongst the Raman spectra of the other TMDCs.

In MoS_2 , we observe two Raman modes: the E_{2g}^1 and A_{1g} [13]. The Raman modes are depicted in terms of atomic vibrations in Figure 1.6(c). E_{2g}^1 is an in-plane vibrational mode, and A_{1g} is an out-of-plane vibrational mode. Figure 1.6(a), from [13], shows the Raman spectrum of MoS_2 as the layer number increases. For monolayer MoS_2 , E_{2g}^1 has a frequency of 384 cm^{-1} , and A_{1g} has a frequency of 403 cm^{-1} . With increasing sample thickness, the E_{2g}^1 mode redshifts, and the A_{1g} mode blueshifts (see Figure 1.6(b)). The difference in frequency of the two modes is a particularly useful metric for distinguishing flake thickness. Additionally, the intensity

of the Raman modes are stronger for monolayer samples than bulk. This is likely due to the substrate interference from the SiO_2 layer on top of the silicon [13].

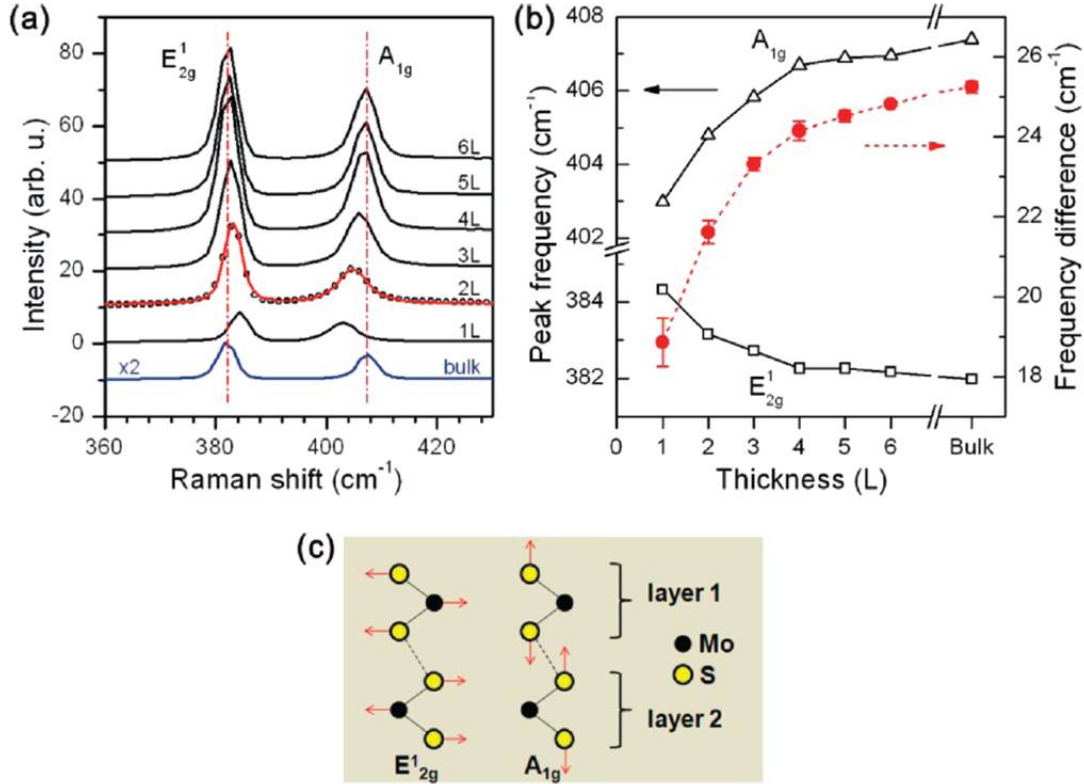


Figure 1.6: Raman spectroscopy of MoS₂ [13]. (a) Raman spectra for samples from one to six layers (1L to 6L) thick and bulk. (b) Peak frequency and frequency difference between the two modes as a function of sample thickness, given in number of layers (L). (c) Depiction of the atomic vibrations of the Raman modes.

In WS₂, we see the same two vibrational modes, E_{2g}¹ and A_{1g}, at 356 cm⁻¹ and 417 cm⁻¹, respectively, in monolayer samples (see Figure 1.7 from [14]). We observe a redshift for E_{2g}¹ and a blueshift for A_{1g} with increasing sample thickness (Figure 1.7(d)). One notable feature of the Raman spectrum of WS₂ is the resonant Raman scattering when excited with 514.5 nm light [14]. We can see in Figure 1.7(b) that there are many new features in the spectrum. The most notable is a longitudinal

acoustic mode, 2LA(M), which overlaps with the E_{2g}^1 mode such that the E_{2g}^1 no longer discernible in the spectrum. The 2LA(M) redshifts with increasing number of layers similar to the E_{2g}^1 , see Figure 1.7(d). For 647 nm excitation, the Raman modes increase in intensity as the sample thickness increases suggesting that the Raman mode intensity depends predominantly on scattering volume. For 488 nm excitation, the Raman modes increase for monolayer through trilayer, but the bulk intensities are lower than those for the monolayer. This is likely due to substrate interference. For 514.5 nm excitation, the modes all increase with decreasing number of layers reaching a maximum intensity at monolayer thickness.

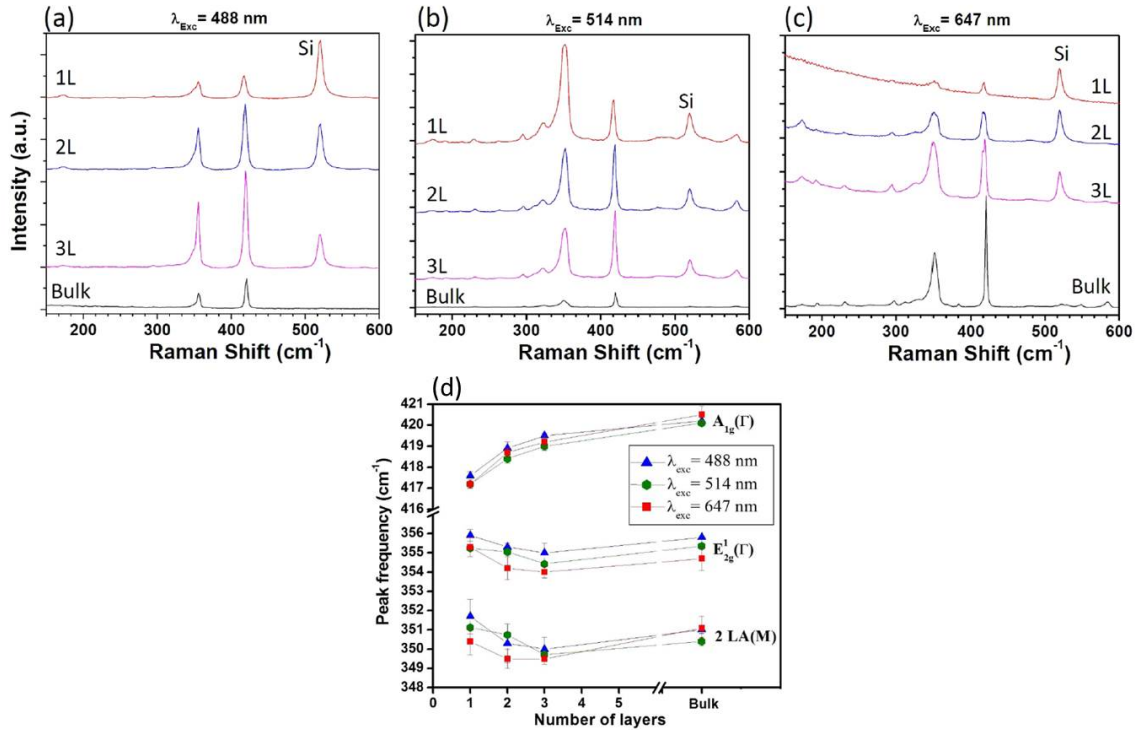


Figure 1.7: Raman spectroscopy of WS₂ [14]. Raman spectra for samples from one to three layers (1L to 3L) thick and bulk when excited by 488 nm (a), 514 nm (b), and 647 nm (c) laser light. (d) Peak frequency of the E_{2g}^1 , A_{1g} , and 2LA(M) modes as a function of sample thickness for the different excitation wavelengths.

In MoSe_2 , there are three Raman modes, see Figure 1.8. The A_{1g} mode occurs at about 240 cm^{-1} for monolayer samples and undergoes a 2 cm^{-1} blueshift for bilayer. The E_{2g}^1 mode is found at 287.2 cm^{-1} for monolayer MoSe_2 and redshifts with increasing thickness. Finally, one out-of-plane mode, B_{2g}^1 , that is inactive in bulk becomes active for thinner layers at 353 cm^{-1} [15].

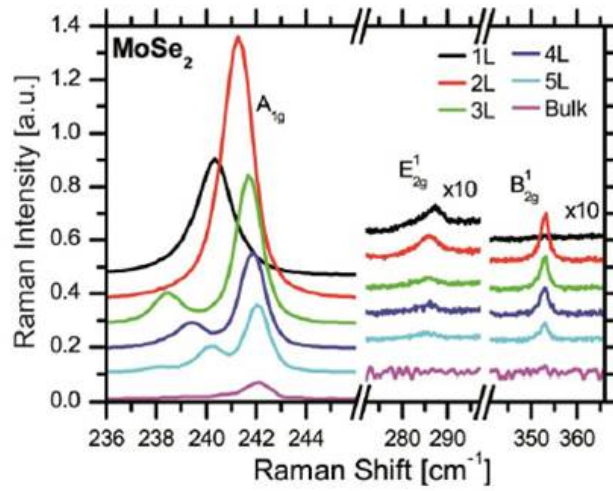


Figure 1.8: Raman spectroscopy of MoSe_2 [15]. Raman spectra are plotted for samples from monolayer (1L) to five-layers (5L) thick.

In bulk WSe_2 , two clear peaks are visible in the Raman spectrum at 248 cm^{-1} and 250.8 cm^{-1} corresponding to the E_{2g}^1 and A_{1g} modes, respectively (see Figure 1.9). However, in thinner flakes, there is only one peak in the same frequency range. This peak could be one of the modes or both modes at nearly degenerate frequencies. As in MoSe_2 , thinner layers have a B_{2g}^1 mode at 309 cm^{-1} that is inactive in bulk [15].

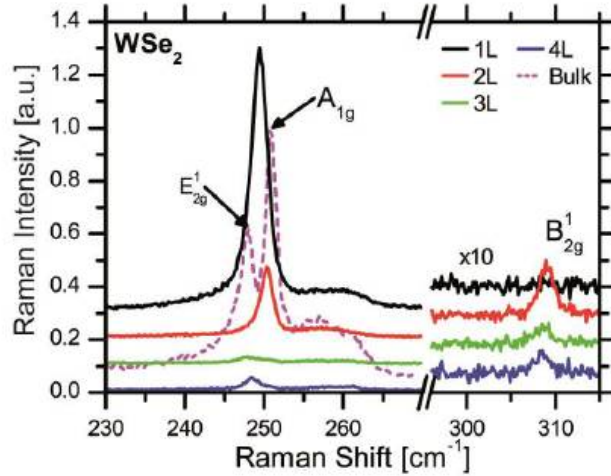


Figure 1.9: Raman spectroscopy of WSe_2 [15]. Raman spectra are plotted for samples from monolayer (1L) to five-layers (5L) thick.

1.3.2 Linear Absorption

The linear absorption of a material allows us to probe the band structure. The onset of absorption can reveal information about the band gap and excitons, a bound state electron-hole pair that will be described in detail in Chapter 2.3.1 and Chapter 3. In this section, we will describe the basic properties of the absorption of graphene and TMDCs. In later chapters, the absorption will be used to probe a few different material properties.

Over a fairly wide spectral range, the absorption of graphene is nearly a flat 2.3%, in agreement with modeling the system as massless Dirac fermions [16]. This approximation is valid in the energy range from 0.5 to 1.2 eV, as shown in Figure 1.10(a). However, at lower and higher energies, this approximation breaks down. At lower energies, there is a dip in the absorption (see Figure 1.10(b)) that can be modeled with inter- and intra-band transitions for noninteracting massless fermions,

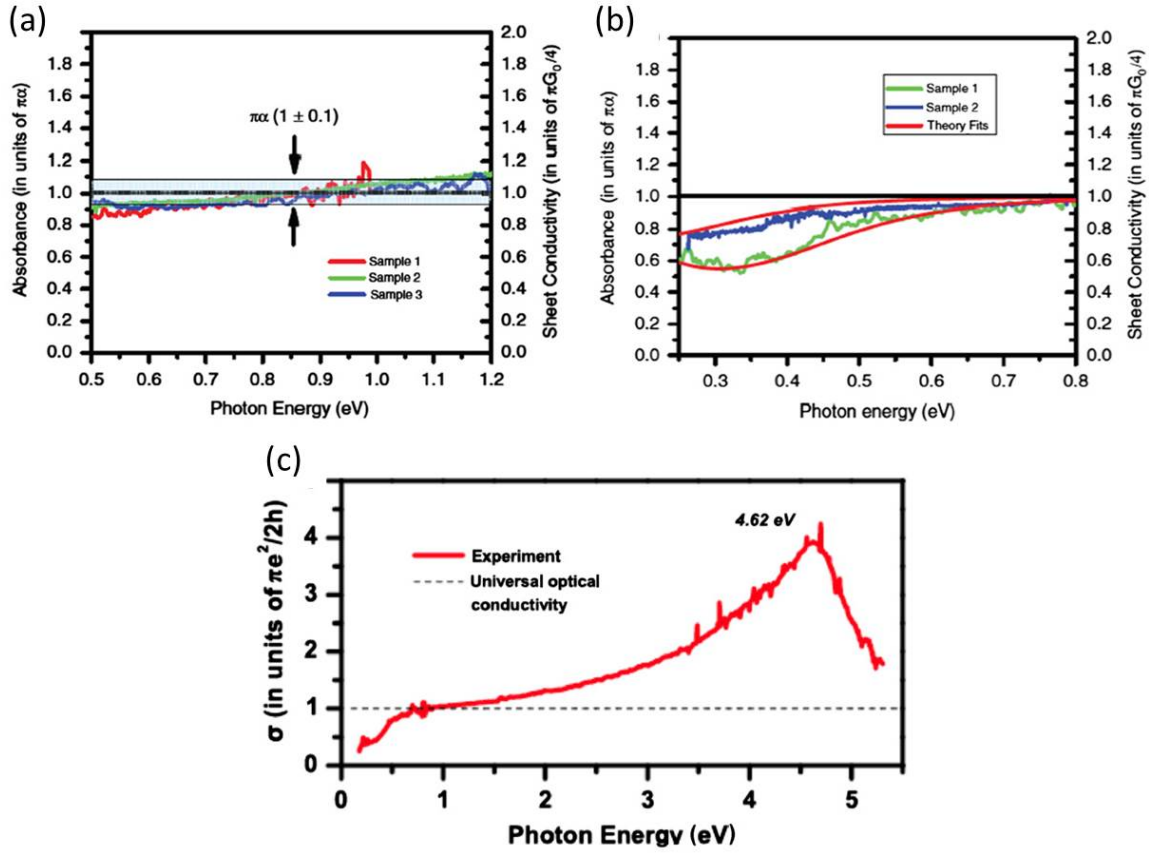


Figure 1.10: Optical absorption of monolayer graphene [17]. (a) Absorption of graphene from 0.5 eV to 1.2 eV, where the absorption is approximately flat as predicted for a massless Dirac fermion. (b) Absorption of graphene from 0.25 eV to 0.8 eV, where the dip depends on the temperature and doping. (c) Absorption of graphene over a wide energy range from 0.25 eV to 5.25 eV. A broad exciton peak can be seen centered at 4.62 eV.

where the magnitude of the dip will depend on temperature and doping [16]. At higher energies, we excite an exciton that is formed at a saddle point in the band between adjacent K points. Thus, the higher energy absorption is dominated by a broad excitonic absorption peak. Figure 1.10(c) is the full absorption spectrum of monolayer graphene with a clear signature of the exciton at 4.62 eV [17].

In TMDCs, the linear absorption is dominated by excitons from various points

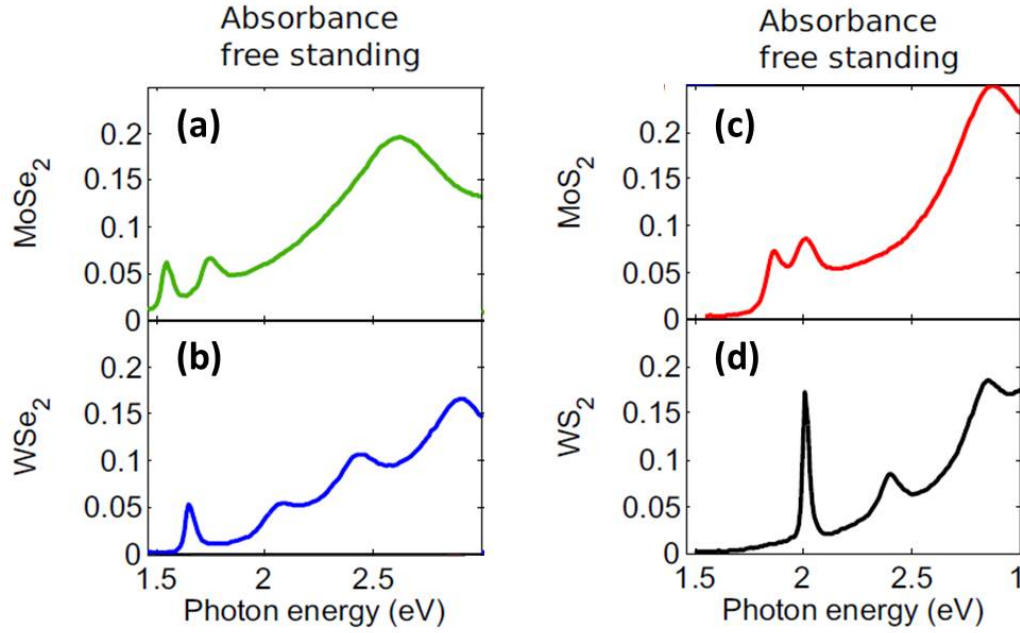


Figure 1.11: Optical absorption of monolayer TMDCs [18]. Absorption of monolayer MoSe₂ (a), WSe₂ (b), MoS₂ (c), and WS₂ (d). The A and B peaks, from excitons at the K-point of the Brioullin zone, are labeled for all four materials. The unlabeled C peaks (C and D for WSe₂) are seen at higher energies around 2.5-3 eV.

in the band. The absorption for monolayer MoS₂, MoSe₂, WS₂, and WSe₂ are given in Figure 1.11 (from [18]). For all four materials, the lowest energy peak is known as the A exciton, a direct transition that occurs at the K-point in the band [6] (see Figure 1.4(b)). The next lowest energy transition, the B peak, also occurs at the-K point. The energy difference between these two peaks arises due to splitting of the valence band at the K-point from spin-orbit coupling. The higher energy broad C peak, or the C and D peak in WSe₂, comes from several different transitions around the Γ point of the band [19, 20].

1.3.3 Photoluminescence in TMDCs

TMDCs are often noted because of their highly efficient photoluminescence (PL) [6]; photoluminescence is described in detail in Chapter 2.3.1. For now, we will simply recall that PL is the light emitted when an exciton radiatively recombines. The photoluminescence from a monolayer TMDC is dominated by the A exciton PL, as shown in Figure 1.12. In monolayer PL, there is also a weak higher energy feature associated with the B exciton and a lower energy shoulder on the A exciton peak from the trion, an exciton with an extra bonded electron.

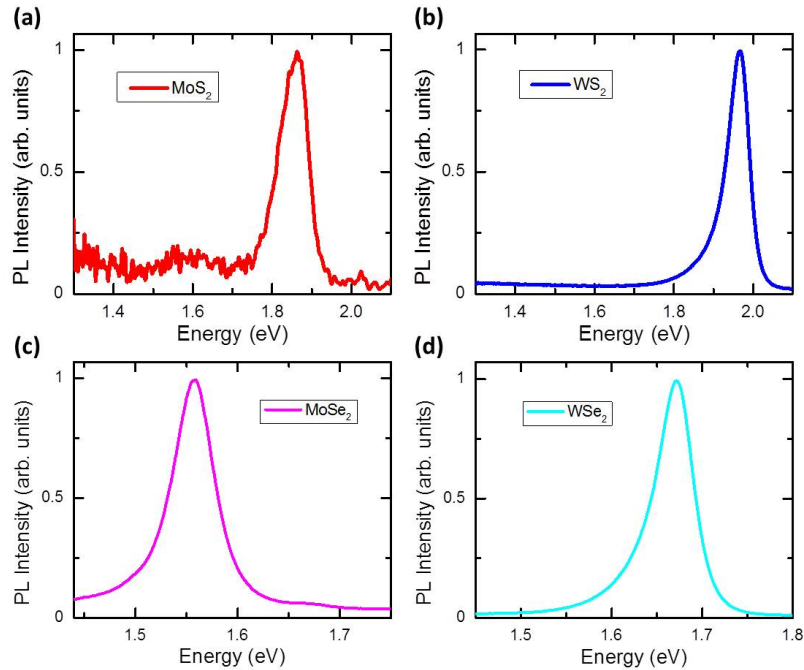


Figure 1.12: Photoluminescence of monolayer TMDCs. Normalized PL of (a) MoS₂, (b) WS₂, (c) MoSe₂, and (d) WSe₂. The PL spectra are dominated by the A exciton for each material.

As the thickness of a TMDC flake increases, the interlayer interactions cause changes in the band structure. With the addition of one layer, TMDCs evolve from

a direct gap semiconductor in monolayer to an indirect gap semiconductor in bilayer [6]. With increasing sample thickness, the valence band Γ point increases in energy as the conduction band minimum associated with the indirect transition (unlabeled Q point) decreases in energy, see Figure 1.4(b). Thus, the energy of the indirect transition decreases as the thickness increases. This trend is seen very clearly in the PL of MoS₂, Figure 1.13(a), where the PL from the indirect transition becomes visible in bilayer and continues to decrease in energy for thicker samples. The A exciton only experiences a slight redshift with increasing sample thickness, but there is a marked decrease in intensity most notable from monolayer to bilayer, as shown in Figure 1.13(b). The intensity decreases because the A transition is no longer the lowest energy transition.

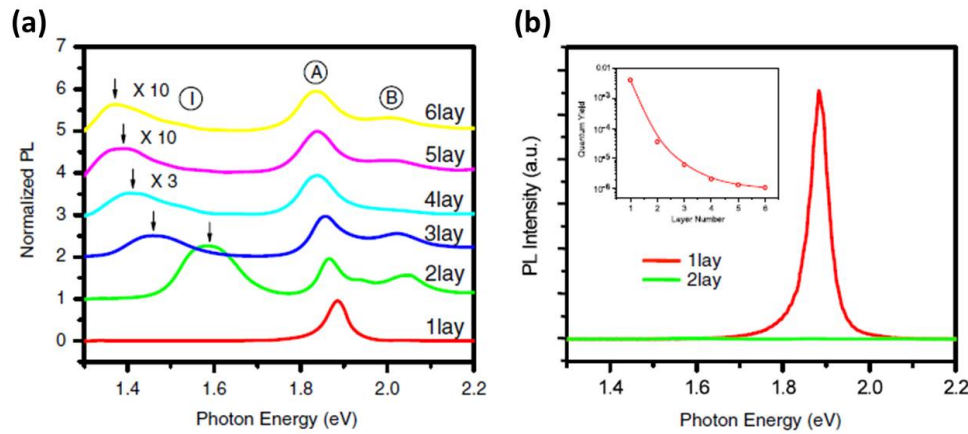


Figure 1.13: Photoluminescence of MoS₂ as a function of thickness [6]. **(a)** Normalized PL for MoS₂ from one to six layers thick (1lay to 6lay). PL peaks originating from the A, B, and indirect (I) transitions are labeled. The spectra are offset for clarity, and, in the thicker samples, the indirect PL is multiplied by the factor shown. **(b)** PL of monolayer and bilayer MoS₂ demonstrating the decrease in the A peak PL intensity. The inset shows the PL quantum yield (QY) for 1 to 6 layer thick MoS₂.

Chapter 2

Experimental Techniques

In this chapter, we will cover the experimental techniques featured in the forthcoming chapters. We aim to provide the essential details, such that a graduate student just starting in the field could build the setups and perform the measurements. The techniques are all optical, except scanning tunneling microscopy/spectroscopy (STM/STS) addressed in the last section of this chapter. First, we will discuss the physics behind the measurement, then the experimental setup, and, finally, any special procedure necessary to perform the measurements or analyze the data. The techniques we will cover are Raman spectroscopy, reflectance contrast, photoluminescence (PL) spectroscopy, photoluminescence excitation (PLE) spectroscopy, and STM/STS.

2.1 Raman Spectroscopy

One of the most fundamental optical techniques is Raman spectroscopy. There is commercial equipment made specifically for Raman spectroscopy, and the technique

is starting to be used in fields as diverse as archeology [21]. However, Raman spectroscopy is perhaps the most essential in materials science. In particular, crystalline solids are marked by very specific Raman signals making Raman spectroscopy an excellent method for characterization. In this section, I will describe the concept behind Raman spectroscopy and the fundamentals of an experimental setup.

2.1.1 Concept

Lattices have vibrational modes called phonons, and Raman spectroscopy allows us to experimentally measure these phonons. Imagine that a material is in its vibrational ground state. When the material absorbs a photon, it is excited into a short lived excited state (virtual energy state), then it relaxes down in energy. If the material returns to the ground vibrational state, the photon emitted has the same wavelength as the photon absorbed. However, if the material relaxes to a vibrational energy state higher in energy, the light emitted will have lower energy than the absorbed light. This case is known as Stokes Raman scattering [10] and is shown schematically in Figure 2.1. If we excite a material that is already in an excited vibrational state, then the system can relax down to the ground vibrational state after absorbing the photon. In this case, the photon energy emitted will be higher than the incident photon energy (anti-Stokes Raman scattering [10]), see Figure 2.1.

If we know the energy of the incident light and measure the energy of the emitted light, we can find the energy of the phonons in the material. The energy of a phonon is given by the equation [10]:

$$E_{phonon} = |E_{\gamma_{inc}} - E_{\gamma_{emit}}| \quad (2.1)$$

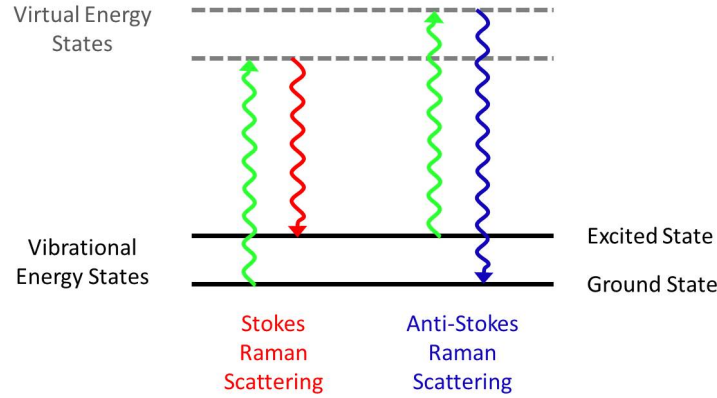


Figure 2.1: Qualitative image of Stokes and anti-Stokes Raman scattering. The incident light (green) excites the material from the vibrational ground state (Stokes) or an excited vibrational state (anti-Stokes) to a virtual energy state. When the material relaxes, it emits light that can have energy equal to the incident light (not shown), less than the incident light (Stokes), or more than the incident light (anti-Stokes).

Where the phonon energy, E_{phonon} , is given in terms of the absolute value (to account for Stokes and anti-Stokes scattering) of the difference in energy between the incident, $E_{\gamma_{inc}}$, and emitted, $E_{\gamma_{emit}}$, light. This quantity is often expressed in terms of wavenumbers in units of inverse centimeters, cm^{-1} . The wavenumber for a phonon, Δw , is defined in terms of the wavelength of the excitation light, λ_{inc} , and the wavelength of the emitted light, λ_{emit} :

$$\Delta w = \frac{1}{\lambda_{inc}} - \frac{1}{\lambda_{emit}} \quad (2.2)$$

2.1.2 Experimental Setup

In this section, we provide the essential elements for a Raman spectroscopy setup, excluding elements purely for alignment, *e.g.* mirrors, or necessary only for specific

types of experiments, *e.g.* polarizers. In a generic Raman setup, a laser is focused onto the sample with an objective, and the light from the sample is collected with the same objective, *i.e.* backscattering geometry. The collected light passes through a filter that blocks the laser but transmits the signal from the sample, which has a wavelength very close to that of the laser. A few different types of filters can be used. If we only want to measure Stokes (anti-Stokes) scattering, we can use a long (short) pass filter with a sharp edge close to the wavelength of the laser. To measure both the Stokes and anti-Stokes scattering we must use a notch filter that transmits higher and lower wavelength light blocking only a narrow band about the wavelength of the laser. After the filter, the light enters a spectrometer with a high line-density grating; the spectrally dispersed light is then measured by a charge-coupled device (CCD). Figure 2.2 is a schematic diagram of a Raman spectroscopy setup with all the elements described. Our Raman measurements were performed on a Renishaw inVia-Raman microscope.

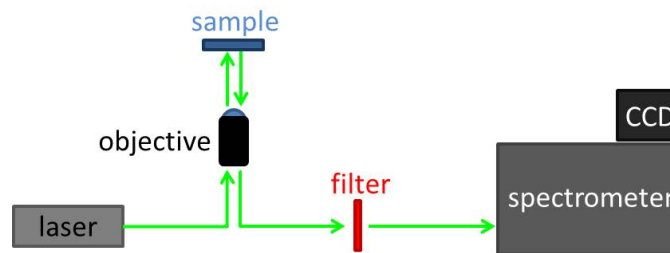


Figure 2.2: A schematic depiction of a Raman spectroscopy setup. From left to right, there is a laser, an objective to focus the laser on the sample, a filter to block the laser light, a spectrometer, and a CCD.

2.2 Reflectance Contrast

In this section, we will discuss reflectance contrast spectroscopy. Reflectance contrast is the experimental technique that we will use the most in this dissertation. First, we will explain the relationship between reflectance contrast and absorption. Next, we will describe the essential elements of the experimental setup. Finally, we will detail the experimental procedure and data processing.

2.2.1 Reflectance Contrast and Absorption

Reflectance contrast measures the light reflected by a sample compared to the light reflected by the substrate. For samples much thinner than the wavelength of the incident light and on a transparent substrate, the reflectance contrast is proportional to the absorption of the material. Solving Maxwell's equations for a thin dielectric film, we find [16]:

$$\frac{\Delta R}{R} = \frac{R_s - R_r}{R_r} = \frac{4}{n_{sub}^2 - 1} A \quad (2.3)$$

Where $\frac{\Delta R}{R}$ is the reflectance contrast, R_s is the reflected light from the sample, R_r is the reference signal from the substrate, n_{sub} is the index of refraction of the substrate, and A is the absorption of the sample. Therefore, reflectance contrast gives us an easy way to approximately measure the absorption of the material.

2.2.2 Experimental Setup

Reflectance contrast uses a broadband light source to measure the light reflected from the sample and the substrate. Typically the light source is a lamp, in our setup a tungsten-halogen lamp, although a supercontinuum or similar broadband laser light

source can be used. For a lamp, it is necessary to create a roughly collimated beam out of the diffuse light. This is done with a lens that focuses the light onto a very small pinhole. A second larger pinhole is placed before a second lens a focal length away from the first pinhole to create roughly parallel beams. The light enters into a microscope where it is focused onto the sample. When a lamp is used, an additional lens is placed just before the microscope to help focus the light to as small a spot as possible with typical spot size in the 2-3 μm range. The signal from the microscope is focused onto the entrance of a grating spectrometer paired with a liquid nitrogen cooled CCD. A schematic diagram of a reflectance contrast setup is depicted in Figure 2.3. A real setup would include mirrors for alignment and other optical elements.

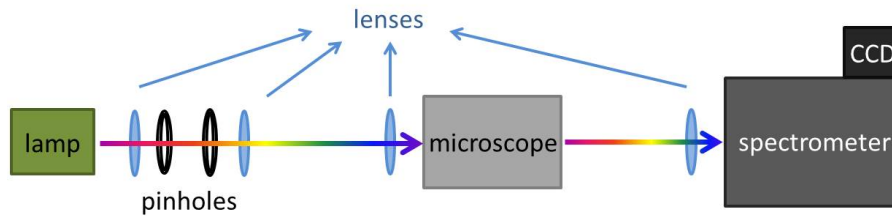


Figure 2.3: A schematic depiction of a reflectance contrast setup. From left to right, there is a lamp, a series of lenses and pinholes, a microscope, a spectrometer, and a CCD.

2.2.3 Measurement Procedure

In each measurement, the light reflected off of the sample is measured over the portion of the spectrum selected by the spectrometer, likely requiring a few spectra to measure the entire desired energy range. To get the reflectance contrast for a flake, we measure the reflected light from the flake and the substrate. Additionally, we measure a background spectrum with the lamp light blocked. Once we measure all the spectra,

we calculate the reflection contrast, $\frac{\Delta R}{R}$, using Equation 2.3 with the background spectrum subtracted from the sample and reference spectra. Long measurements will typically have a good signal to noise ratio. However, in some cases we smooth the reflectance contrast spectrum with a 5 or 10 point adjacent averaging.

2.3 Photoluminescence Spectroscopy

In this section, we will discuss photoluminescence spectroscopy in semiconductors. First, we will discuss the theory behind photoluminescence. We will then describe the photoluminescence spectroscopy experimental setup.

2.3.1 Photoluminescence in Semiconductors

In semiconductors, there is a gap between the valence and conduction band. When a semiconductor is excited by light with energy larger than or equal to the band gap, an electron from the valence band can be excited into the conduction band (see Figure 2.4(a)). The vacancy left behind in the valence band is a positively charged quasi-particle called a hole [10]. If the Coulomb forces are sufficient between the electron and hole, they can form a bound state called an exciton. When the electron and hole recombine, light is emitted with energy equal to the band gap minus the binding energy of the exciton [10]. This emitted light is called photoluminescence (PL). Figure 2.4(b) qualitatively shows the process of exciton creation and radiative recombination.

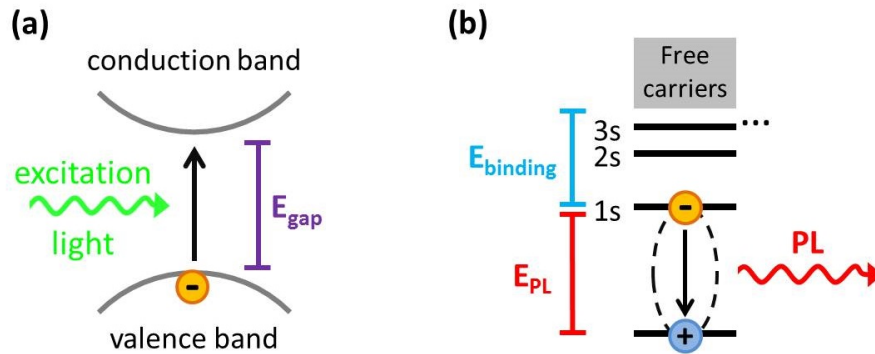


Figure 2.4: Schematic depiction of photoluminescence in semiconductors. **(a)** The valence and conduction band of a semiconductor with an electron in the valence band being excited into the conduction band by incoming light. The energy of the band gap is indicated in purple. **(b)** An exciton is shown radiatively recombining and emitting photoluminescence (PL). The energy of the PL and the binding energy of the exciton, E_{binding} , are indicated with respect to the energy levels of the exciton.

2.3.2 Experimental Setup

A photoluminescence spectroscopy setup is similar to a Raman spectroscopy setup. A laser with energy high enough to create excitons enters into a microscope, where it is focused on the sample. The light from the sample is collected in backscattering configuration and passes through a filter that blocks the reflected laser light. The remaining signal, the photoluminescence, then passes through a spectrometer to be spectrally dispersed and measured by a CCD. The essential elements of a photoluminescence setup are depicted in Figure 2.5. In a real setup, there would be additional optical elements, mirrors for alignment, *etc.* Our measurements were performed on a Renishaw inVia-Raman microscope.

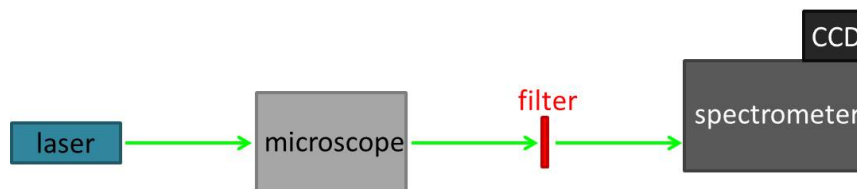


Figure 2.5: A schematic depiction of a photoluminescence spectroscopy setup. From left to right, there is a laser, a microscope to focus the laser on the sample, a filter to block the laser, a spectrometer, and a CCD.

2.4 Photoluminescence Excitation Spectroscopy

In this section, we will discuss an optical technique called photoluminescence excitation (PLE) spectroscopy. PLE incorporates elements of photoluminescence spectroscopy and reflectance contrast. We will describe the concept behind photoluminescence excitation spectroscopy, the elements of a typical experimental setup, and the measurement procedure.

2.4.1 Concept

In Chapter 2.3.1, we discussed photoluminescence in semiconductors. However, this picture was a bit simplistic. Firstly, a material will only absorb a certain percentage of the incident light. The amount of light absorbed as a function of excitation energy is the absorption of the material. The absorption of TMDCs is determined largely by the excitons, see Figure 1.11.

The second complicating factor is the efficiency of radiative recombination. For any excitation energy, there will be non-radiative relaxation channels that compete with radiative recombination and limit the efficiency [10]. Therefore, not all of the absorbed photons will be reemitted. Additionally, when we excite a semiconductor,

we do not necessarily know where in the band we are exciting, especially at high excitation energies when more transitions are accessible. In order to radiate at one part of the band, say the K-point like in TMDCs, the electron and hole must first relax to that part of the band. Thus, the quantum efficiency will depend on the relaxation pathways within the valence and conduction bands.

Photoluminescence excitation spectroscopy (PLE) allows us to probe these intricacies. In PLE, we measure the PL intensity as a function of the excitation wavelength. This is distinct from both reflectance contrast, which simply measures the light absorbed as a function of wavelength, and PL spectroscopy, which uses only a single excitation energy. If we compare the PLE with reflectance contrast, we can infer information about the relaxation pathways in the material, as we will discuss in Chapter 3.

2.4.2 Experimental Setup

In PLE, as in reflectance contrast, we use a broadband light source, either a lamp or a supercontinuum laser. In our setup, we used a supercontinuum laser. A laser provides two advantages: higher intensity and a collimated beam. However, supercontinuum lasers have high intensity pulses, which can easily damage samples. A lamp source would be unlikely to damage a sample, however, may not have sufficient power. The light, from either source, passes through a variable wavelength filter or, as in our setup, a monochromator (grating spectrometer). Either one allows us to select the excitation wavelength.

After the monochromator, the light passes through an adjustable neutral density filter, so we can select the power at each wavelength. The light is then focused onto

the sample with either an objective or a microscope with the signal collected in backscattering geometry. The signal passes through a filter which can block all the excitation wavelengths we use in the experiment but not the PL. This is typically done with a long pass filter with the edge close in wavelength to the sample PL. The closer the filter edge is to the PL wavelength, the closer we can get to resonant excitation. Finally, the light enters a grating spectrometer coupled to a CCD. The essential elements of a PLE setup are shown in Figure 2.6. Once again, we do not include mirrors and other standard optical elements.

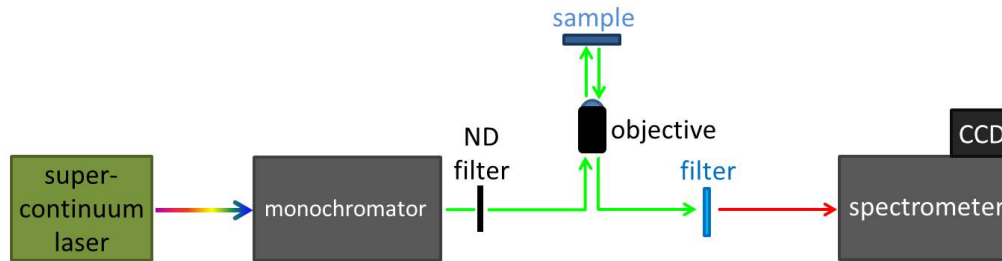


Figure 2.6: A schematic depiction of a photoluminescence excitation setup. The setup consists of a supercontinuum laser source, a monochromator to select the excitation wavelength, a variable ND filter to adjust the power, an objective to focus the laser on the sample, a filter to remove the excitation light from the signal, a spectrometer, and a CCD.

2.4.3 Measurement Procedure

A typical measurement has a few steps. First, we select the initial excitation wavelength and adjust the monochromator accordingly. The neutral density filter must be set such that the average power of the light is the desired value, then we measure the PL spectrum of the sample. We continue to the next excitation wavelength following the same steps. Once all of the spectra are taken, we can fit a peak or peaks to each

PL spectrum. Finally, we create a plot of the integrated intensity of the peak as a function of the excitation wavelength. This is the PLE spectrum for the sample.

2.5 STM and STS

In this section, we will discuss scanning tunneling microscopy (STM) and scanning tunneling spectroscopy (STS). First, we will address the theory behind STM and STS measurements. Next, we will briefly describe the fundamental features of a typical experimental setup. Both of these sections are guided by a textbook from Chen [22]. Finally, we will outline how the data is analyzed (more details in Chapter 5).

2.5.1 Concept

In both STM and STS, a conducting tip is brought close to the surface of a sample. A voltage difference is applied between the material and the tip. If the voltage is sufficient, electrons can tunnel between the surface of the sample and the tip. We are able to measure the tunneling current into or out of the sample. The tunneling current depends on the tip to surface distance, the bias voltage, and the sample's local density of states.

For STM measurements, the tip moves parallel to the sample (x-y plane) to create an image of the surface. The measurement is performed in what is known as constant current mode. In constant current mode, the height of the tip adjusts to keep the tunneling current at a constant value set by the user. The surface image is constructed by recording the height of the tip as a function of the x-y position.

In STS, the height of the tip is kept constant as the voltage is varied, *a.k.a*

constant height mode. We measure the tunneling current as a function of voltage and obtain an I-V curve. This measurement is performed at various x-y positions on the sample.

2.5.2 Experimental Setup

STM/STS experimental setups are fairly complicated. Here, we will only provide a broad overview of a few of the key elements. The conducting tip is one fundamental part of the setup. The tip must have a single atom at its apex in order to obtain a well defined STM image. We used mechanically cut tungsten tips. The height and position of the tip is controlled by a set of electronics using a Piezoelectric tube. Additionally, there are electronics that amplify the tunneling current before it is recorded. Finally, the setup is incredibly sensitive to vibrations, thus it must be designed to isolate the sample and tip from external vibrations. This is typically done with gas suspension or mechanical springs.

2.5.3 Data Processing

In STS measurements, we obtain I-V curves for a number of points on sample. The quantity of interest is dI/dV , which is related to the conductance of the material [22]. We take the derivative of our data with respect to voltage to obtain a dI/dV curve. Once we have the dI/dV curves, we can find the band gap of the sample from the onsets of the current. To do so, the data is fitted with a model to extract the current onset voltages. The model we use to fit the dI/dV curves, described in detail in Chapter 5, takes into account thermal broadening, the in-plane momentum dependence of the tunneling probability, and tip-induced band bending.

Chapter 3

Exciton Binding Energy in Monolayer MoS₂ and WS₂

In this chapter, we will discuss the experimental observation of the excited states and binding energy of the excitons in monolayer TMDCs. First, we will describe the non-local screening model we used for our two-dimensional system. Next, we will address how the binding energy can be determined experimentally. We will particularly focus on the optical techniques of reflectance contrast and photoluminescence excitation spectroscopy (PLE). We will present the results of these two measurements on WS₂ and MoS₂ and the binding energies we extract. Finally, we will compare our results with other published values.

3.1 Modeling the Exciton

In this section, we will discuss a theoretical model for excitons in two-dimensional materials. The presentation of this discussion is strongly guided by the preprint and

published version of a paper by Berkelbach *et al.* [23]. Professor Tim Berkelbach and Professor David Reichman developed this model and graciously collaborated with us to apply the model to our experimental results.

3.1.1 Hydrogenic Model

In quantum mechanics, the hydrogen atom, a bound state of an electron and proton, is a preferred system, because it can be analytically solved. The hydrogenic model is frequently used to describe Wannier excitons in inorganic semiconductors [10]. In three dimensions, the screened hydrogen Hamiltonian is given by:

$$H = \frac{P^2}{2\mu} + V_{eh}(r) = -\frac{\hbar^2 \nabla_r^2}{2\mu} - \frac{e^2}{\varepsilon r} \quad (3.1)$$

Where H is the Hamiltonian operator, P is the momentum operator, μ is the effective mass, V is the interaction potential, \hbar is the reduced Planck constant, e is the charge of an electron, ε is the dielectric screening constant, r is the distance between the electron and proton or hole, and the last two terms are the operators in real-space spherical coordinates.

However, excitons occur within a material with its own complicated set of potentials. Typically, the influence of the surrounding material is accounted for in two ways: dielectric screening and electron/hole effective mass. First, we treat the material as a slab of uniform dielectric screening of magnitude ε . This dielectric screening constant will be the value used for the Coulomb screening in Equation 3.1. The

reduced mass of the exciton, μ , is given by:

$$\mu = \frac{1}{m_e^{-1} + m_h^{-1}} \quad (3.2)$$

Where m_e is the effective mass of the electron, and m_h is the effective mass of the hole. For Wannier excitons, where the distance between electron and hole is larger than the lattice constant, the band structure of the lattice is incorporated into the mass of the electron and hole through the effective mass approximation (see Appendix A).

The energy levels in the hydrogen atom take discrete values determined by the principal quantum number, n , and the equation:

$$E_n^{3D} = -\frac{\mu e^4}{2\hbar^2 \epsilon^2} \frac{1}{n^2} \quad (3.3)$$

The energy spectrum resulting from this equation is known as the Rydberg series. Each energy state is referred to by its principal quantum number, n , and the orbital it occupies, s from the spherical symmetry. Therefore, the energy levels are denoted 1s, 2s, 3s, *etc.* We will use the term Rydberg series and the ns notation in our excitonic system as well.

When we restrict the hydrogen model to two dimensions, the Hamiltonian remains the same but the energy spectrum becomes:

$$E_n^{2D} = -\frac{\mu e^4}{2\hbar^2 \epsilon^2} \frac{1}{(n - 1/2)^2} \quad (3.4)$$

Therefore, in the hydrogen model, the binding energy in two dimensions is four times

that in three dimension, $E_b^{2D} = 4E_b^{3D}$.

3.1.2 Nonlocal Screening Model

Simply confining the hydrogen Hamiltonian to 2D is not valid for our system. The 2D hydrogen model assumes that the dielectric screening is a constant and the same value as in 3D. However, the material is now approximately limited to two dimensions, while the electric field between the electron and hole extends into all three dimensions. The limitation of the screening to a thin layer leads to nonlocal screening of the exciton, as we will explain using the field lines between the electron and hole (see Fig. 3.1). The field lines that extend out of the material experience little or no screening, since they do not pass through the sample, while field lines passing through the material will experience screening. Therefore, an electron and hole that are spatially close, and consequently have fewer field lines extending outside the material, will experience stronger screening than an electron and hole with greater separation.

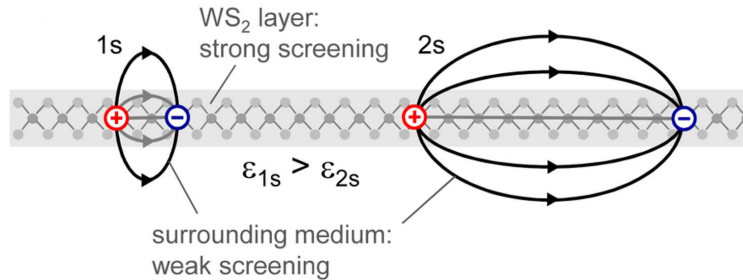


Figure 3.1: Qualitative depiction of the interaction between an electron and hole at smaller and larger separation in a 2D layer [24]. At larger separation, the electric field extends into the surrounding medium more than at small e-h separation and, therefore, undergoes reduced screening.

To incorporate distance dependence in the screening, we return to the Poisson's

equation to solve for the potential, $\phi(\mathbf{r})$, in terms of the charge density, $n(\mathbf{r})$. The charge density will include contributions from external, $n_{ext}(\mathbf{r})$, and induced, $n_{ind}(\mathbf{r})$, charge densities. Poisson's equation is:

$$\nabla^2\phi(\mathbf{r}) = -4\pi n(\mathbf{r}) = -4\pi[n_{ext}(\mathbf{r}) + n_{ind}(\mathbf{r})] \quad (3.5)$$

The induced charge density can be found using the polarization of the material, $n_{ind}(\mathbf{r}) = -\nabla \cdot \mathbf{P}(\mathbf{r})$. In the linear response regime, we introduce χ defined such that $\mathbf{P}(\mathbf{r}) = -\chi\nabla\phi(\mathbf{r})$. In 3D, solving Poisson's equation yields the Coulomb potential, $\phi(r) = e^2/\epsilon r$ and $\epsilon = 1 - 4\pi\chi$. To restrict to two dimensions, we create a two dimensional polarization and polarizability,

$$\mathbf{P}_{2D}(\boldsymbol{\rho}) = -\chi_{2D}\nabla_{\boldsymbol{\rho}}\phi(\boldsymbol{\rho}, z = 0) \quad (3.6)$$

Where ρ is the charge separation. Consequently, the induced charge density becomes:

$$n_{ind}(\mathbf{r}) = \delta(\mathbf{z})\chi_{2D}\nabla_{\boldsymbol{\rho}}^2\phi(\boldsymbol{\rho}, z = 0) \quad (3.7)$$

Where the charges are strictly confined to the plane of the material, set at $z = 0$. If we plug this back into Poisson's equation, Equation 3.5, we can solve for the Fourier transform of the potential:

$$\phi_{2D}(\mathbf{q}) = \frac{2\pi e}{q(1 + 2\pi\chi_{2D}q)} \quad (3.8)$$

Where we can define the 2D screening as $\epsilon_{2D}(q) = 1 + 2\pi\chi_{2D}q$. Note that the

dielectric screening now has q dependence unlike the 3D case [23]. If we take the Fourier transform to recover the real space interaction potential, we obtain [23],

$$V_{2D}(\rho) = e\phi(\rho) = \frac{e^2}{4\chi_{2D}} \left[H_0 \left(\frac{\rho}{2\pi\chi_{2D}} \right) - Y_0 \left(\frac{\rho}{2\pi\chi_{2D}} \right) \right] \quad (3.9)$$

Where H_0 is a Struve function, and Y_0 is a Bessel function of the second kind. While the potential takes a rather complicated form, we can understand the general behavior by looking at the trends for small and large ρ . At large ρ , the potential behaves as $1/\rho$, meaning we recover an unscreened Coulomb potential. Looking back to Figure 3.1, this makes sense, because at large enough distances a negligible number of the field lines are passing through the material. At smaller ρ , the potential behaves as $\log(\rho)$, a much weaker interaction due to increased screening. The crossover from the strongly screened to unscreened Coulomb interaction is $2\pi\chi_{2D}$, the 2D polarizability length.

Now that we have a 2D interaction potential we can use the variational method, as was done for excitons in semiconductor quantum wells [25, 26, 27], on our Hamiltonian to approximately solve for the exciton binding energy. We select a radially symmetric 2D test function,

$$\psi(\rho, a) = \sqrt{\frac{2}{\pi a^2}} e^{-\frac{\rho}{a}} \quad (3.10)$$

This test function is the ground state solution to the unscreened 2D hydrogen Hamiltonian. Variational analysis is performed using a as a tunable parameter, where a is an estimate of the exciton radius. To obtain the binding energy, we minimize the sum of kinetic and potential energy, $T(a) + V(a)$, where $T(a) = 1/(2\mu a^2)$ is the kinetic

energy of our test function.

In [23], this procedure is performed for the four most common TMDCs: MoS₂, MoSe₂, WS₂, and WSe₂. The table below, from the same paper, gives the reduced mass, 2D polarizability, binding energy from the non-local screening method, and binding energies calculated using the many-body Bethe-Salpeter equation (BSE) from several other references. While some of the BSE binding energy values are twice the nonlocal screening binding energies, Shi *et al.* [28] found that with high enough k -point sampling the BSE binding energies converge to values similar to the binding energies we find.

	μ (m_0)	χ_{2D} (Å)	Exciton binding energy (eV)	
			Theory	BSE
MoS ₂	0.25	6.60	0.54	1.03, ²⁰ 1.1, ²¹ 0.5, ²² 0.54 ²³
MoSe ₂	0.27	8.23	0.47	0.91 ²⁰
WS ₂	0.16	6.03	0.50	1.04, ²⁰ 0.54 ²³
WSe ₂	0.17	7.18	0.45	0.90 ²⁰

Figure 3.2: Monolayer TMDC reduced mass, 2D polarizability, exciton binding energy calculated from the nonlocal dielectric screening model, and exciton binding energy calculated using the BSE [23].

3.2 Experimental Observation

In this section, we will discuss the experimental observation of the exciton binding energy. One method involves measuring the transition energy of the lowest energy exciton state and the energy of the quasiparticle band gap. The photoluminescence or reflectance contrast gives the transition energy, and the band gap can be found

with scanning tunneling spectroscopy. The binding energy of the exciton is given by the equation [24]:

$$E_b(n) = E_g - E_{tr}(n) \quad (3.11)$$

Where n is the principal quantum number and takes only integer values, $E_b(n)$ is the binding energy of the n th state, E_g is the quasi-particle gap, and $E_{tr}(n)$ is the transition energy of the n th excitonic energy state. The n th state binding energy in the 2D hydrogen model (recall from Equation 3.4) is given by [23]:

$$E_b(n) = \frac{\mu e^4}{2\hbar^2 \varepsilon^2 (n - 1/2)^2} \quad (3.12)$$

If we cannot measure the band gap directly, as in optical measurements in TMDCs, we can measure the transition energy of multiple energy states to extrapolate to the band gap and ascertain the excitonic energy spectrum. Unfortunately, the transition energies of the higher excited states are not probed by photoluminescence, therefore, we first turn to absorption (reflection contrast) as a possible method to probe the excited exciton states.

3.2.1 Reflectance Contrast of TMDCs

If there was no interaction between electrons and holes, the absorption in a semiconductor would be a step function, 0 for energies below the band gap and nonzero for energies above the band gap. However, in TMDCs we have strong electron-hole interactions, which lead to exciton formation. For a semiconductor with a single band, we would expect to have an absorption peak for each discrete energy level of the exciton and a step function for the continuum limit of a free unbounded electron, *i.e.* the

band gap. The absorption features will have decreasing oscillator strength, which is proportional to the area of the absorption peaks, in addition to decreasing energy spacing between states/features. The absorption of a semiconductor with excitons is qualitatively shown in Figure 3.3, where the first 3 energy states are shown along with the band gap. In a real material, there are more excited exciton states.

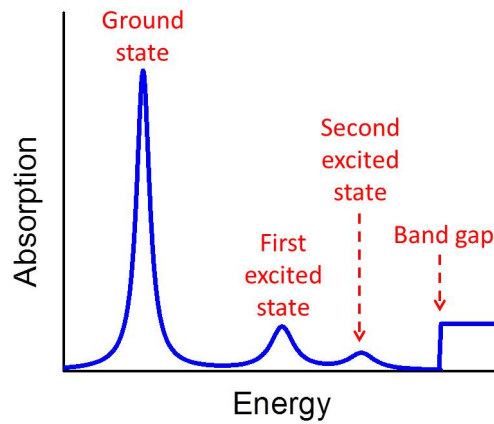


Figure 3.3: Qualitative graph of the absorption from a semiconductor with exciton formation in a single band. The peaks correspond to the ground, first excited, and second excited exciton states with a step function for the band gap.

If we can measure the absorption of a material and obtain a spectrum like the one above, then finding the binding energy would be simple. We would subtract the energy of the ground state exciton peak from the energy of the step function onset, *a.k.a.* the energy of the band gap.

However, in TMDCs there are many exciton transitions in different bands and at different points in k -space, including very broad higher energy features [19, 20]. Additionally, electron-phonon interactions broaden all the features [19]. Therefore, a typical TMDC will have an absorption/reflectance contrast spectrum like the one in

Figure 3.4 from a monolayer MoS₂ sample. We can still see the lowest energy (1s) state of the excitons, labeled A, B, and C in Figure 3.4, but the higher energy exciton states are not clearly visible due to the high spectral background. The spectrum in Figure 3.4 is found from Kramers-Kronig constrained variational analysis performed on the experimental reflectance contrast spectrum of a mechanically exfoliated monolayer MoS₂ sample on a fused silica substrate [18].

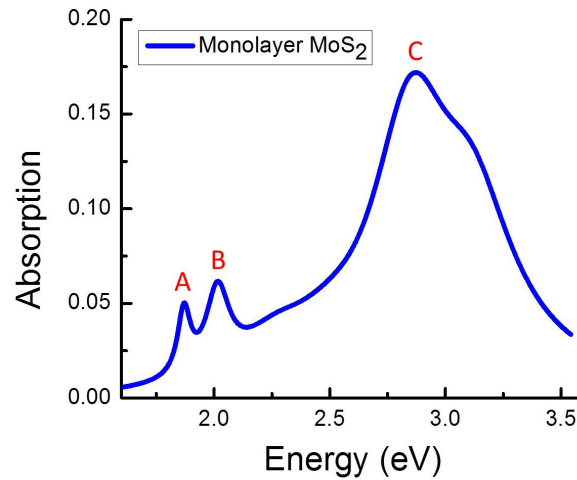


Figure 3.4: Absorption spectrum of monolayer MoS₂. The absorption is found by performing Kramers-Kronig constrained variational analysis on the measured reflectance contrast spectrum for a sample on fused silica.

How to observe the small absorption peaks from excited exciton states is the fundamental dilemma for experimentally probing the exciton binding energy of TMDCs. One easy potential solution is taking the derivative of the absorption to render small features more readily observable. We will use this strategy on WS₂.

In our following analysis, we use the reflectance contrast in lieu of absorption. Recall for thin materials on a transparent substrate, the reflectance contrast is proportional to the absorption [16] (see Chapter 2.2.1). Since we only need the overall

shape of the absorption to discern the excitonic features, the reflection contrast serves well as a substitute for absorption.

3.2.2 Reflectance Contrast of WS₂

We are able to observe the excited states of the WS₂ A exciton by taking the derivative of the reflection contrast with respect to energy, $\frac{d}{dE} \left(\frac{\Delta R}{R} \right)$. In a paper by Chernikov *et al.* [24], we measured the reflectance contrast of WS₂ on a silicon substrate with a 300 nm silicon dioxide epilayer (Si/SiO₂). The inset of Figure 3.5 is an example of a low temperature reflection contrast spectrum. The spectrum looks different from the absorption in Figure 1.11(d) due to the interference from the SiO₂ epilayer, but the exciton ground state peaks are still clearly visible. However, the higher energy excited states are not obvious. We took the derivative of the spectrum, plotted over a smaller energy range in Figure 3.5. Now we can clearly see an entire series of excited state features. The excited states are labeled using the Rydberg series convention with their energy quantum number, n , and orbital, s . A point of inflection in the derivative spectrum corresponds to a peak in the reflectance contrast.

Unfortunately, we are unable to observe the quasi-particle band gap. However, we can fit the nonlocal screening model (from Section 3.1.2) to the transition energies of the excited exciton states and extrapolate to the band gap. In Figure 3.6, we plot the experimental transition energies as a function of quantum number n alongside the hydrogen and nonlocal screening models fitted to the experimental data. To fit the nonlocal screening model, Professor Tim Berkelbach used the DFT calculated exciton reduced mass, $\mu = 0.16m_0$ where m_0 is the rest mass of an electron [23]. The model has two adjustable parameters: $\rho_0 = 2\pi\chi_{2D}$, the screening length, and E_g , the band

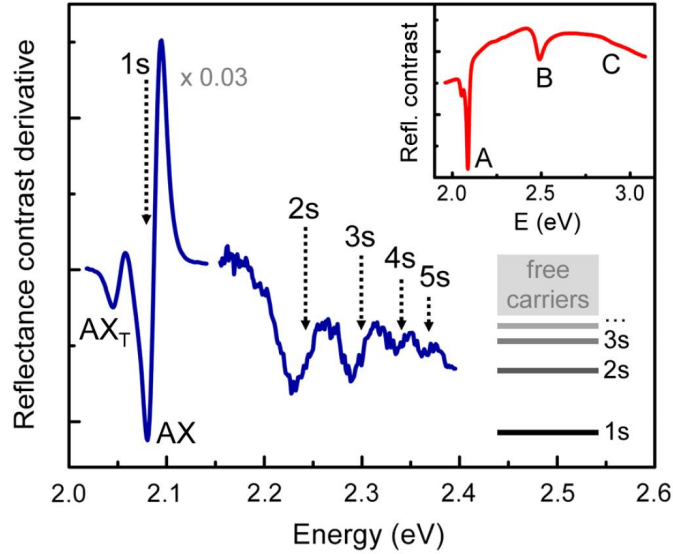


Figure 3.5: Derivative of the reflectance contrast spectrum of monolayer WS_2 [24]. The excited exciton states are labeled by their quantum number. The 1s feature has been scaled by a factor of 0.03. The inset shows the as-measured reflection contrast over a wider energy range with the A, B, and C excitons labeled.

gap. Minimizing the root-mean-squared deviation, the parameters that give the best fit are $\rho_0 = 75 \text{ \AA}$ and $E_g = 2.41 \text{ eV}$ [24]. We can see in Figure 3.6 that the nonlocal screening model fits the experimental data very well. The same band gap, $2.41 (\pm 0.04) \text{ eV}$, is obtained when the 2D hydrogen model is fitted to the data for $n = 3 - 5$.

The unscreened 2D hydrogen model is a good fit for $n \geq 3$ [24]. Higher energy exciton states are more spatially separated, therefore, more of the field lines pass outside of the material and are unscreened (look back at Figure 3.1 for a helpful depiction). Thus, for higher energy states, the behavior approaches that of the unscreened 2D hydrogen model. To investigate this trend, we examine the effective dielectric screening as a function of n , plotted in the inset of Figure 3.6. If we rewrite

Equation 3.12, the effective dielectric constant for the n th energy state, ε_n , is [24]:

$$\varepsilon_n = \sqrt{\frac{\mu e^4}{2\hbar^2 E_b(n)(n - 1/2)^2}} \quad (3.13)$$

To find the effective dielectric constant, we use the difference in energy between the calculated band gap and the experimental transition energies as the binding energy of the n th state, $E_b(n)$. In Figure 3.6, we can see that the effective dielectric quickly, asymptotically approaches 1. Furthermore, for $n \geq 3$ the effective dielectric screening remains roughly constant as n increases. This suggests that the screening no longer has strong electron-hole separation dependence.

Finally, we can calculate the binding energy of the A-exciton of WS₂. From the reflectance contrast we know that the transition energy of the 1s state is 2.09 eV in our sample, and from the fits to our experimental data we know that the band gap is 2.41(±0.04) eV. As stated in Equation 3.11, the binding energy for the n th state is the difference between the band gap and the transition energy of that state, $E_g - E_{tr}(n)$. Therefore, the exciton binding energy is 0.32(±0.04) eV [24]. The nonlocal screening model calculated *ab initio* a binding energy of 0.50 eV for pristine suspended monolayer WS₂ [23] (see Figure 3.2). The calculated value agrees with the experimental binding energy as well as we would expect since the substrate, with its additional screening, would reduce the exciton binding energy. The screening length from our experimental data, r_0 , does not agree well with the *ab initio* value, because the screening length partially accounts for the screening from the substrate.

With the nonlocal screening model, we also calculate the spatial extent of the 1s exciton wavefunction to be 30 Å [24]. The thickness of a single layer of WS₂ is about

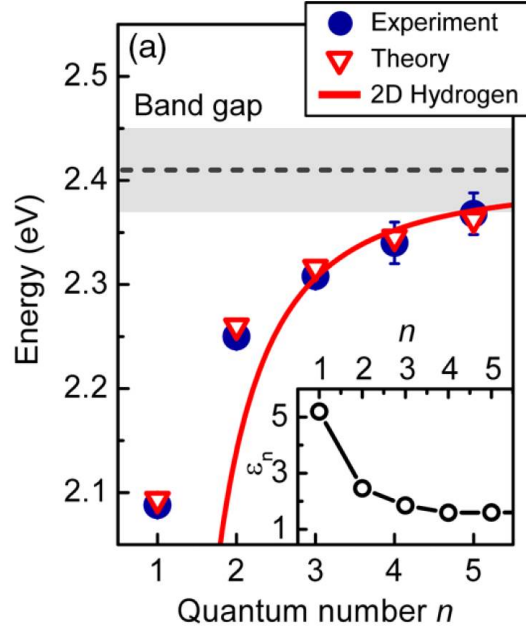


Figure 3.6: Transition energies of the excited states of the monolayer WS_2 A exciton as a function of quantum number n [24]. The experimental values are obtained from the derivative of the reflection contrast. The theory transition energies derive from fitting the nonlocal screening model to the experimental values for $n = 1 - 5$. The 2D hydrogen model curve is obtained by fitting to the experimental data for $n = 3 - 5$. The grey dashed line is the band gap from the nonlocal screening model, and the shaded grey area is the uncertainty. The inset shows the evolution of the effective dielectric constant with quantum number n .

6.5 Å, suggesting that the two-dimensional approximation is reasonable. Additionally, the large spatial spread implies a small distribution in reciprocal space. Therefore, the effective mass approximation is also reasonable because the distribution in k -space would be tightly centered on the K/K' -point and should not be affected much by the rest of the Brillouin zone.

We also investigate the effect of sample thickness on the exciton binding energy. In Figure 3.7(a), we show the derivative of the reflection contrast for monolayer, bilayer, four-layer, and bulk WS_2 . The A exciton 1s feature only shifts slightly in

energy with decreasing sample thickness. However, we see that in thinning from bulk to monolayer the energy of the 2s increases dramatically. The energy of the 1s and 2s states are plotted as a function of layer number in Figure 3.7(b). Using an anisotropic 3D hydrogen model and *ab initio* values for the material parameters, we can calculate the exciton binding energy in the bulk material. We find a bulk binding energy of 0.05 eV and a band gap of 2.1 eV [24], both in good agreement with experimentally obtained values [29]. The dashed lines in Figure 3.7(b) indicate the monolayer and bulk band gaps. It is clear that the band gap and binding energy increase in energy as the sample gets thinner.

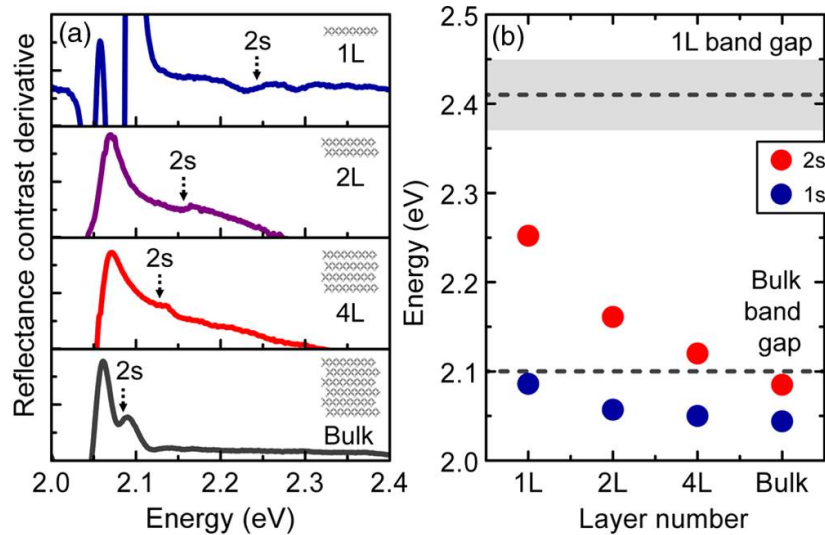


Figure 3.7: Thickness dependence of the band gap and exciton binding energy in WS₂ [24]. **(a)** Derivative of the reflectance contrast for monolayer (1L), bilayer (2L), four-layer (4L), and bulk WS₂. The A exciton 2s state is indicated with a dotted arrow. **(b)** Energy of the 1s and 2s features of WS₂ as a function of layer number. The upper and lower dashed lines indicate the monolayer and bulk quasiparticle band gaps, respectively.

After this comprehensive study on WS₂, it is easy to imagine that there is no need to explore other methods for obtaining the exciton binding energy. However,

WS₂ is a unique material even among TMDCs. It is easier to observe the WS₂ excited exciton states for two reasons. First, the WS₂ A exciton 1s state has a much sharper absorption feature than the other TMDCs. Secondly, compared to the other TMDCs the splitting between the A and B exciton in WS₂ is quite large, and the spectral background is low in the energy range just above the A exciton 1s peak (see Figure 1.11). Therefore, the excited exciton states are less likely to be obscured by the A or B exciton 1s peak or the background. We find that the other TMDCs do not have discernible signatures of the excited exciton states in reflectance contrast. Therefore, we need to investigate alternate methods for observing the Rydberg series and exciton binding energy.

3.2.3 PLE of TMDCs

The details of PLE measurements were presented in Chapter 2 section 4. For our present discussion recall that PLE measures the PL intensity as a function of the energy of the light used to excite the sample. If the number of photons emitted by the material depends solely on the number of photons absorbed, the PLE would have the same shape as the absorption. In Figure 3.8(a), we plot the PLE and absorption of monolayer MoS₂ and WS₂ on fused silica substrates. We can see that there are differences between the PLE and absorption spectra. To quantify the difference, we calculate the relative quantum efficiency (QE) in arbitrary units using the equation:

$$QE \propto \frac{PLE \times E_{exc}}{A} \propto \frac{\# \text{ A exciton photons emitted}}{\# \text{ photons absorbed}} \quad (3.14)$$

Where E_{exc} is the excitation energy, and A is the absorption. In an ideal system with fast relaxation to the lowest energy state and negligible nonradiative recombination, the quantum efficiency would be 1 and independent of energy. In Figure 3.8(b), we plot the relative QE from our PLE and absorption measurements. There is an order of magnitude decrease in the QE at higher energy in the range measured. This indicates that there are significant nonradiative decay channels with strong excitation energy dependence.

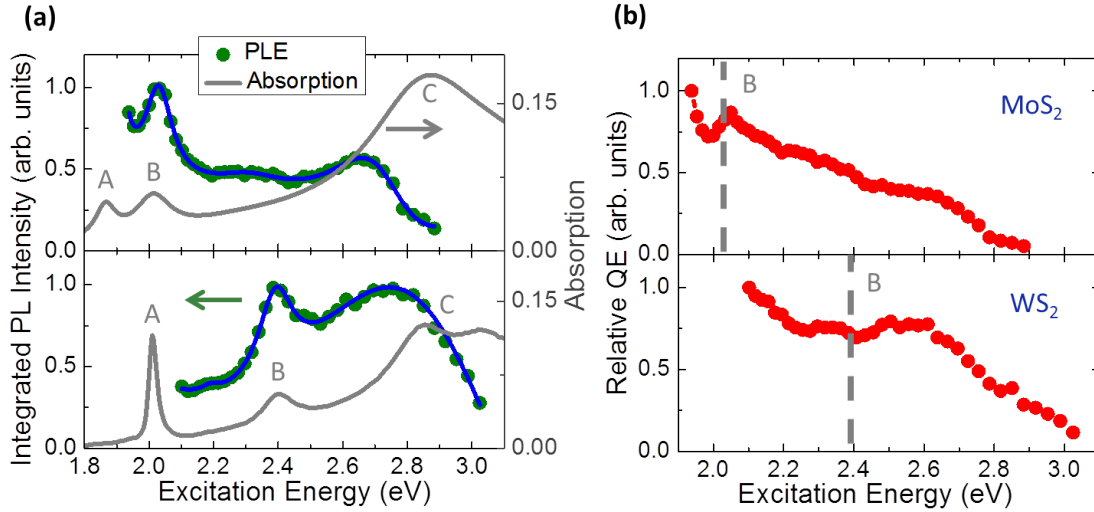


Figure 3.8: PLE, absorption, and relative QE of monolayer MoS₂ and WS₂ [30]. **(a)** Absorption (right axis) and PLE (left axis) of monolayer MoS₂ (top) and WS₂ (bottom) on fused silica. The PLE spectra are normalized to the intensity of the B exciton peak. The blue curves are a guide to the eye. **(b)** Relative QE of monolayer MoS₂ and WS₂. The relative QE is found by normalizing the PLE to the absorption and photon energy. The B exciton is marked by a dashed grey line. The QE is normalized to the highest value in range.

We did not investigate the source of this energy dependent decay channel. However, in the paper by Kozawa *et al.* [31] they observed the same QE reduction in their own PLE measurements and investigated the energy dependence of the absorption

and subsequent relaxation. Carvalho *et al.* [20] reported that higher energy photons are predominately absorbed near the Γ -point in the band nesting region, where the valence and conduction bands are parallel to one another enhancing the absorption. Kozawa *et al.* calculated the 2D band structure around the region of band nesting. Their calculations suggested there are local minima/maxima in the conduction/valence band near the band nesting region where the electron and hole are likely to relax, the Λ -point for electrons and Γ -point for holes. Radiative recombination is a slower process for indirect transitions, and it is a multi-phonon process to move from the Λ - or Γ -point to the K/K'-point of the Brillouin zone, where the A transition occurs. This could explain the reduced QE for higher energy visible photons.

The QE reduction at higher energy is useful for observing excited exciton states that are masked in the reflection contrast by the large C transition. In the PLE, the background from these higher energy transitions is reduced in the region where we would expect to see excited exciton states. Additionally, the excited exciton states should exhibit efficient relaxation into the ground state exciton, as has been seen in GaAs quantum wells [32], since the states are already at the K-point. Efficient excited state relaxation and reduced spectral background both suggest that PLE would be a promising method to observe the Rydberg series of the excitons in TMDCs.

Before we address the results of our PLE measurements on TMDCs, we will verify that the experimental conditions are appropriate. First, we demonstrate that we have linear power dependence in the range used in the experiment. We measure the PL counts as a function of power starting from the value used in our measurements and up to five times that value. As can be seen in Figure 3.9(a), the dependence is indeed linear. We also find that the PLE was power and sample independent. In

Figure 3.9(b), we plot the PLE taken at two different powers on two different samples of the same material on the same type of substrate.

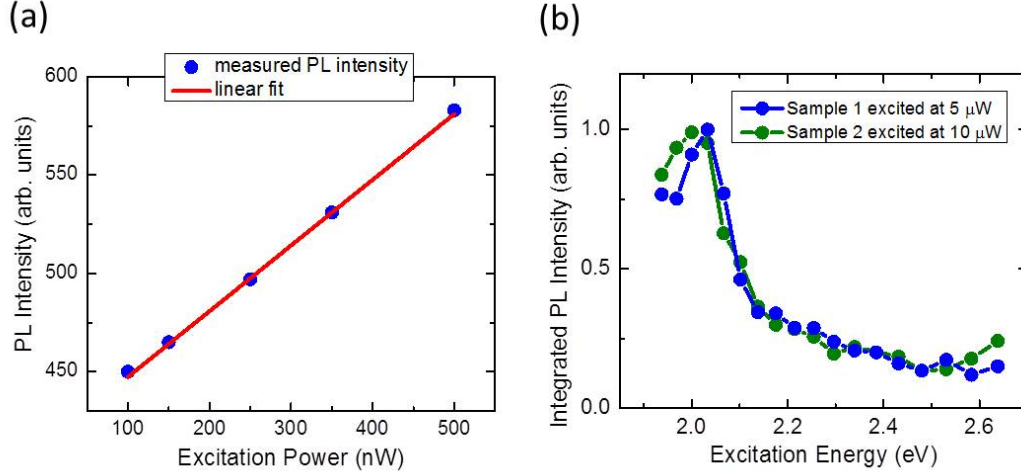


Figure 3.9: Power and sample dependence of PL and PLE [30]. (a) Monolayer MoS₂ PL intensity as a function of the laser excitation power. The red line is a linear fit to the data. (b) PLE of two different samples of monolayer MoS₂ on the same type of substrate (BN on Si/SiO₂) excited at different powers.

Furthermore, exciton-exciton annihilation should not be significant for the laser fluence we use. The paper by Sun *et al.* [33] investigated the carrier density dependence of the annihilation rate in MoS₂ for laser fluence from 8 to 46 $\mu\text{J}/\text{cm}^2$. The reported exciton density dependent annihilation rate was $k_A = (4.3 \pm 1.1) \times 10^{-2} \text{ cm}^2/\text{s}$. The laser fluence in our measurements is on order 0.01 $\mu\text{J}/\text{cm}^2$. MoS₂ absorbs about 10% of the light (the exact amount varies with energy). We assume that each absorbed photon will create an exciton, and we use an average excitation energy for the range in our PLE measurements ($\sim 2.5 \text{ eV}$). We obtain an exciton density of approximately $2 \times 10^9 \text{ excitons}/\text{cm}^2$ and, therefore, an annihilation rate of $k_A \approx 10^8 \text{ s}^{-1}$. The rate of annihilation ($\sim 10 \text{ ns}$) is much slower than the exciton emission lifetime ($\sim 10\text{-}100$

ps). Therefore, exciton-exciton annihilation is negligible in our measurements.

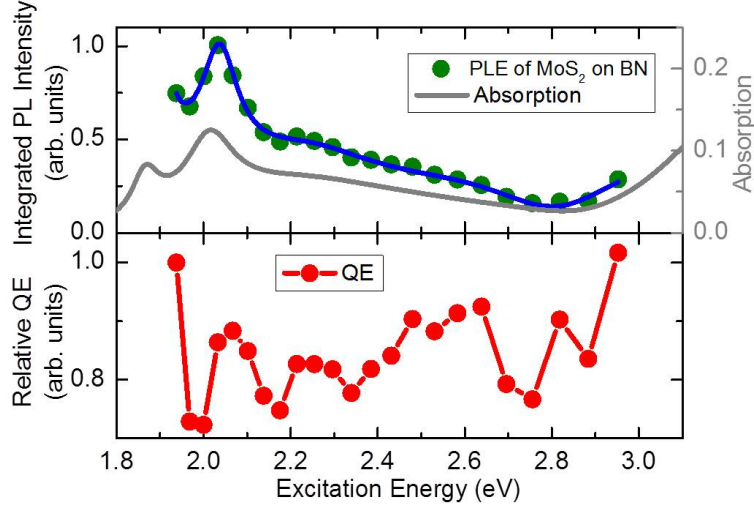


Figure 3.10: Absorption, PLE, and relative QE for monolayer MoS_2 on BN [30]. **(top)** Absorption (right axis) and PLE (left axis) of monolayer MoS_2 on a thin BN flake on a Si/SiO_2 substrate. The PLE spectrum is normalized to the intensity of the B exciton peak. The blue curve is a guide to the eye. **(bottom)** Relative QE from normalizing the PLE to the absorption and photon energy. The QE is normalized to the first data point.

We do find that different substrates change the PLE spectrum, see Figure 3.10 (top) where we plot the PLE for a monolayer MoS_2 sample on a thin (~ 20 nm) BN flake on a Si/SiO_2 substrate. The BN and SiO_2 epilayer (300 nm thick) produce interference which leads to a drastic change in the effective absorption of the MoS_2 . Using an approximate BN thickness from AFM and a simulation of the absorption, we obtain the effective absorption for the sample, also plotted in Figure 3.10 (top). When we calculate the relative QE, plotted in Figure 3.10 (bottom), we see the trend is very different from the sample on fused silica. However, the simulated absorption is quite sensitive to the thickness of the BN which has a level of uncertainty from the

AFM measurement. It is possible the differences in the QE arise from an inaccurate simulated absorption. As this sample provides the clearest excited exciton spectrum, we have reason to believe that it is a good sample (few defects, *etc.*). It is possible that this sample truly experiences more efficient relaxation into the A exciton from all points in the band.

3.2.3.1 PLE of WS₂

We first present the PLE of monolayer WS₂ since we can compare with the excited exciton states in the reflectance contrast. In Figure 3.12, we plot the PLE with the background subtracted of monolayer WS₂ on fused silica (as-measured spectrum shown in Figure 3.11). In Figure 3.12, we also plot the derivative of the room temperature reflectance contrast on the same sample; the reflectance contrast over a wider spectral range is included in the inset. We find the transition energies of the excited state excitons from the point of inflection in the derivative of the reflectance contrast. In the figure, we indicate the position of the 2s and 3s peaks by dashed lines. The features in the PLE spectrum align well with the excited states in the reflectance contrast, therefore, we feel confident assigning them to the Rydberg series of the A exciton. In the PLE, we are also able to see a small 4s peak that is not clear in the derivative of the room temperature reflectance contrast.

To extract the band gap, we can use the nonlocal screening model on states $n = 1 - 4$ or the 2D hydrogen model on the 3s and 4s states (recall that the 2D hydrogen model is a reasonable approximation for $n \geq 3$). From both methods we obtain a band gap of $2.33(\pm 0.05)$ eV and a binding energy of $0.32(\pm 0.05)$ eV, which agrees with our low temperature reflectance contrast results.

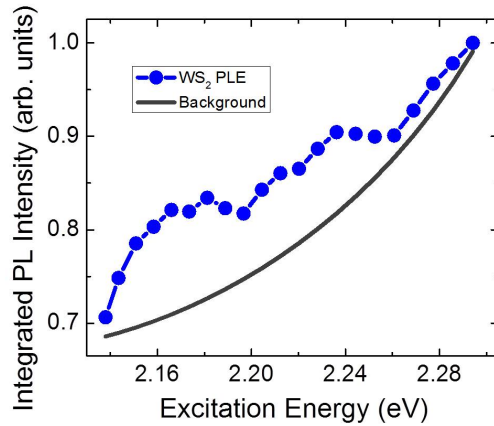


Figure 3.11: PLE of monolayer WS_2 on fused silica [30]. The PLE is normalized to the highest value in range. The background curve (dark grey line) is subtracted from the PLE for Figure 3.12.

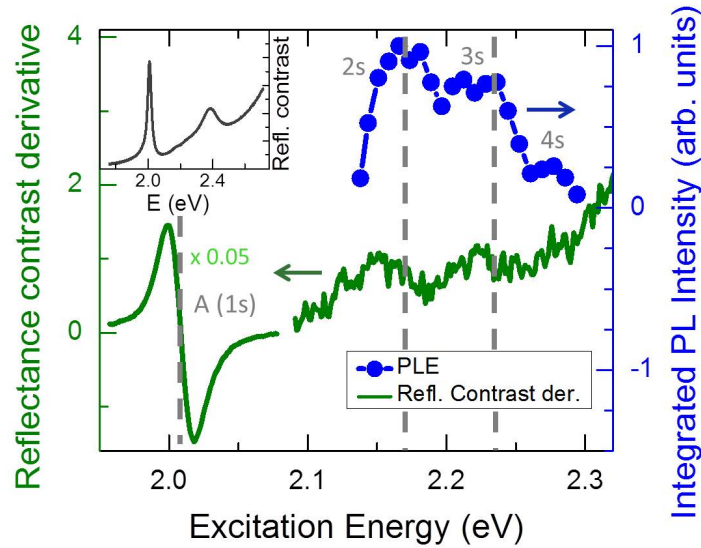


Figure 3.12: PLE (right axis) and derivative of the reflectance contrast (left axis) of monolayer WS_2 on fused silica [30]. The PLE has a smooth background subtracted (see Figure 3.12) and is normalized to the highest value in range. The 1s, 2s, and 3s energies are indicated by dashed grey lines. The reflectance contrast over a wider spectral range is given in the inset.

3.2.3.2 PLE of MoS₂

We now turn to MoS₂ which has excited exciton states that could not be discerned in the reflectance contrast. In Figure 3.13(a), we plot the the PLE of MoS₂ for two monolayer samples: one on fused silica and one on a thin (~ 20 nm) flake of BN on a Si/SiO₂ substrate (silicon with a 300 nm epilayer of SiO₂). MoS₂ on BN has a stronger PL signal which enhances the PLE features.

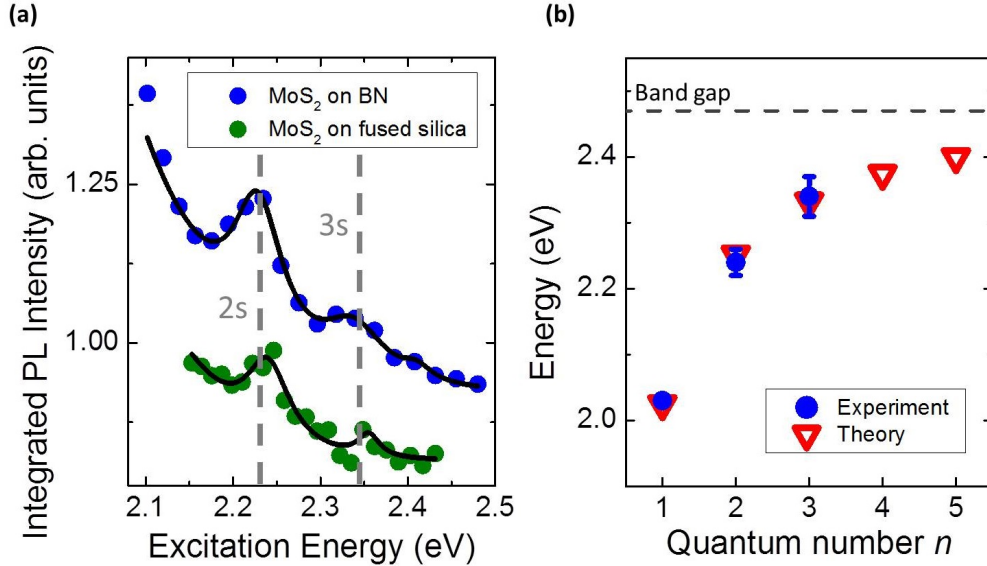


Figure 3.13: Excited exciton transition energies in monolayer MoS₂ from PLE and from theory [30]. **(a)** PLE of two monolayer MoS₂ samples: one on fused silica and one on a thin BN flake on a Si/SiO₂ substrate. The PLE is normalized to the highest value in range and vertically offset. The smooth black lines are guides to the eye, and the grey dashed lines roughly indicate the energies of the 2s and 3s excited state features. **(b)** Experimental and theoretical values for the transition energies of the Rydberg series of the MoS₂ B exciton. Experimental values are from the PLE spectra, and the theory values are found by fitting the nonlocal screening model to the experimental data. The calculated band gap is mark by a dashed grey line.

Much like the PLE of WS₂, we see two distinct peaks in the PLE of MoS₂ at 2.24 (± 0.02) eV and 2.34 (± 0.03) eV. The energies of these peaks vary slightly between

the two samples likely due to the sensitivity of the energy of the excited states to the dielectric environment [24]. In WS₂ the spin-orbit splitting of the A and B excitons is larger than in MoS₂. Therefore, the WS₂ A exciton excited states have transition energies less than that of the B exciton 1s, and their assignment to the Rydberg series of the A exciton is unambiguous. However, in MoS₂ the A and B splitting is much less, so we must carefully consider the assignment of the excited exciton states as they could be part of the Rydberg series of the A, B, or A and B excitons.

There are three possible assignments for the observed features: the peaks could be the A and B exciton 2s states, the A exciton 2s and 3s states, or the B exciton 2s and 3s states. We are able to exclude the A and B exciton 2s states assignment. If we assume that the A and B excitons have the same binding energy, the energy difference between the A and B 2s states would be the same as the energy difference between the 1s states. However, the energy difference between the two observed peaks is only about 0.1 eV compared to the 0.15 eV for the 1s states (see the absorption spectrum in Figure 3.8). Furthermore, the B exciton is calculated to have larger reduced mass [34, 35] (in Berkelbach's calculations $\mu_B = 0.28m_0$ compared to $\mu_A = 0.25m_0$ [23]) and, consequently, a larger binding energy. If we assume the mass scaling of the exciton binding energy in the 2D hydrogen model, we would expect the spacing between the 2s states to be 0.19 eV. This suggests an even greater discrepancy between the observed energy separation and what we would expect for the 2s states. Additionally, since the A and B exciton 1s states have similar oscillator strength in MoS₂, the 2s states should likewise have similar oscillator strengths. Instead, we observe a reduction by a factor of 2 between the integrated area of the observed peaks, a typical oscillator strength reduction between 2s and 3s states. Therefore, we conclude that the observed

features must be the 2s and 3s states of a single Rydberg series.

The observed PLE features could be the 2s and 3s states of the A exciton Rydberg series. This assignment yields a binding energy of $0.64(\pm 0.08)$ eV, see Figure 3.14 for the band gap and theory fit for this assignment. We cannot definitively exclude this assignment. However, the exciton binding energy is twice that of the A exciton in WS_2 . We have no reason to anticipate such a large difference in binding energy between the two materials from theoretical calculations [23, 28, 36] or from the binding energies measured in other TMDCs [24, 37, 38, 39, 40]. Additionally, it is much larger than the other experimentally obtained binding energies in MoS_2 [41, 42] (further comparison with other experimental work found in Chapter 3 section 3.2). Finally, as mentioned, the oscillator strengths are similar for the A and B exciton in MoS_2 . Therefore, we ought to see the excited states of the B exciton as well. The absence of these features in the PLE complicates this assignment.

Our preferred interpretation is that the peaks arise from the 2s and 3s states of the B exciton. Assuming a similar band gap and binding energy for the A exciton Rydberg series, the A exciton 2s and 3s transition energies would be 2.05 eV and 2.15 eV which are close to the energy of the B exciton 1s state. The B exciton 1s state would likely obscure the much smaller spectral features of the A exciton 2s and 3s, which is probably why we do not observe them. Additional support for this assignment comes from the oscillator strengths. The area of the PLE features is related to the oscillator strengths of the states. By fitting Lorentzian peaks to the Rydberg features (see Figure 3.15), we obtain oscillator strengths relative to the B exciton 1s peak of $0.22(\pm 0.07)$ and $0.10(\pm 0.08)$ for the 2s and 3s peaks, respectively. From reflectance contrast on WS_2 , we obtain oscillator strengths of $0.14(\pm 0.06)$ and

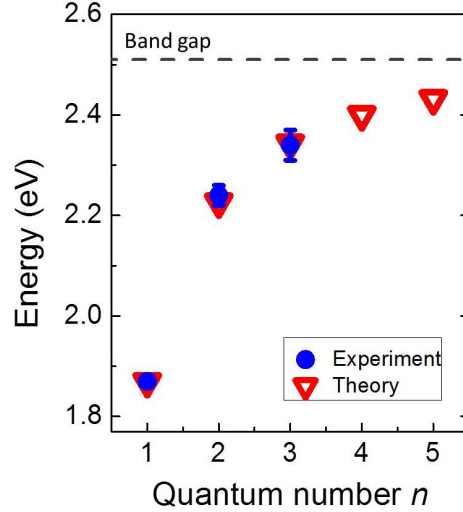


Figure 3.14: Experimental and theoretical values for the transition energies of the Rydberg series of monolayer MoS₂ if we assign the observed peaks to the A exciton Rydberg series [30]. The experimental values come from PLE, and the theory values come from fitting the nonlocal screening model to the experimental data. The calculated band gap is indicated by a dashed grey line.

0.06(\pm 0.03) for the 2s and 3s features relative to the 1s state which agree well with our observation in MoS₂. Our theoretical model also predicts oscillator strengths of 0.23 and 0.11 for the B exciton Rydberg series, in excellent agreement with the experimental results.

To fit the theoretical model to the experimental data, Professor Tim Berkelbach used the reduced mass from *ab initio* calculations, $\mu = 0.27m_0$. The adjustable parameters are the band gap and 2D polarizability; he found the best fit to the B exciton Rydberg series with $\chi_{2D} = 9.3 \text{ \AA}$ and $E_g = 2.47 \text{ eV}$. The polarizability is higher than calculated for a suspended sample [23] (see Figure 3.2) as was the case in the fit of the WS₂ reflectance contrast data [24]. The higher polarizability compensates for the screening from the substrate. In Figure 3.13(b), we plot the experimental values for the transition energies of the excitonic states alongside the energies from

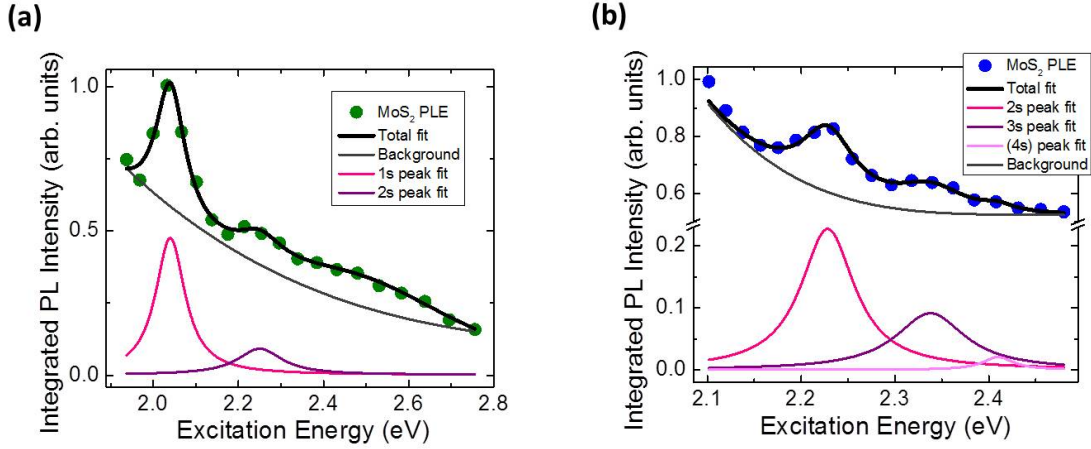


Figure 3.15: PLE of monolayer MoS₂ on a thin BN flake on a Si/SiO₂ substrate [30]. The PLE is normalized to the highest value in range. The grey line is the smooth background, the pink and purple lines are Lorentzian fits to the excitonic features, and the black lines are the sum of all the curves. From Figure (a), we find the ratio of the integrated area of the 1s and 2s features. From Figure (b), we find the ratio of the 2s and 3s integrated areas. In Figure (b), there is a break in the vertical axis along with a change in the scale. Additionally, we see a small peak that may be the 4s state.

the nonlocal screening fit. The agreement is very good. From the band gap, we find a binding energy of $0.44(\pm 0.08)$ eV for the MoS₂ B exciton. This value agrees well with the A exciton binding energy in WS₂. MoS₂ is predicted to have a larger binding energy than WS₂ (0.54 eV compared to 0.50 eV from the nonlocal screening model [23] and Figure 3.2) in addition to the expected difference in binding energy for A and B excitons. Finally, our binding energy agrees well with the calculated value, 0.54 eV for a suspended sample, when we consider the binding energy reduction due to screening from the substrate.

3.3 Conclusions

In this section, we will offer our final thoughts on the exciton binding energy in TMDCs. First, we will summarize the chapter. Next, we will compare our experimental exciton binding energy with the binding energy from theoretical calculations and other experimental techniques. Finally, we will comment on the importance of our research and describe some topics still open for investigation.

3.3.1 Summary

In this chapter, we experimentally investigated the exciton binding energy in monolayer MoS₂ and WS₂. First, we described a nonlocal screening model for an exciton in a 2D material. Next, we used reflectance contrast and PLE to probe the Rydberg series of the A and B exciton in WS₂ and MoS₂, respectively. We fit the nonlocal screening model to the transition energies of the Rydberg series to extract the band gap and exciton binding energy. The exciton binding energy in monolayer was a remarkable order of magnitude larger than the binding energy in bulk.

3.3.2 Comparison with Other Works

In this subsection, we will compare our experimental binding energy results for WS₂ and MoS₂ with the available literature to date. First, we will briefly note the wide range of published theoretical binding energy values. We will then compare our results with other published experimental results.

3.3.2.1 Theory Comparisons

There are a dozen different theoretical calculations for the binding energy in monolayer TMDCs. The majority are GW-BSE calculations [19, 28, 36, 43, 44, 45, 46, 47], a few are modified hydrogenic model calculations much like the nonlocal screening model [23, 48], and a few are alternate Hamiltonian formulations [34, 35]. The resulting binding energies vary from $\sim 0.1 - 1\text{eV}$. Our theoretical and experimental results fall towards the middle of this large range. However, the best measure of the accuracy of our results is comparison with other experimental binding energy values.

3.3.2.2 Experimental Comparisons

There have been a great deal of experimental studies on the exciton binding energy of monolayer TMDCs. We did not perform measurements on MoSe_2 or WSe_2 , but they should have comparable exciton binding energies to MoS_2 and WS_2 . The published exciton binding energy for monolayer MoSe_2 is about 0.55 eV (Ugeda *et al.*) [38], and the published binding energies for WSe_2 are 0.37 eV (He *et al.*) [37] and ~ 0.6 eV (Wang *et al.*) [40]. For MoSe_2 , the binding energy was obtained from direct STS measurement of the band gap and PL measurement on the same sample to obtain the 1s transition energy. The measurements were performed for a monolayer sample on bilayer graphene and another sample on bulk graphite. The He *et al.* paper [37] directly measured the band gap optically for samples on Si/SiO_2 and quartz without recourse to a particular theoretical model. The Wang *et al.* paper [40] used a BSE model fit to excited states observed with single- and two-photon PLE for a sample on Si/SiO_2 . All three values are reasonably similar to our values for MoS_2 and WS_2 (we do expect some variation from one material to another). We note that the papers

that directly measure the band gap and do not rely on a model are closer in value to the binding energies we measure. Additionally, the MoSe₂ paper uses samples on graphene/graphite which changes the dielectric environment and, therefore, the binding energy.

There have also been studies on the materials we examined, WS₂ and MoS₂. For WS₂, the paper by Ye *et al.* [39] reports an exciton binding energy of ~ 0.7 eV for a monolayer sample on fused quartz. They used one- and two-photon PLE to observe excited exciton states and fit the experimental results with a GW-BSE theory. This binding energy is twice what we measured, but it is likely that the discrepancy arises from the different theory models implemented.

For MoS₂, there are two experimental papers. The paper by Zhang *et al.* [41] uses STS and PL on a monolayer sample on graphite to obtain the band gap and 1s transition energy. In the STS data, they observe two possible thresholds and accordingly report two potential binding energies, 0.22 (± 0.1) eV and 0.42 (± 0.1) eV. The second value agrees very well with our results. Additionally, since the sample is on graphite we would expect a change in the exciton binding energy due to the dielectric screening. Therefore, the lower binding energy of 0.22 eV also might not be incompatible with our results. The second paper by Klots *et al.* [42] uses photocurrent measurements to find the transition energy and band gap for a suspended sample. From their measurement they obtain a binding energy of ≥ 0.57 eV. A suspended sample is expected to have a larger binding energy than a sample under the influence of screening from a substrate. Therefore, their results agree well with ours when the substrate screening is taken into account.

3.3.3 Impact and Future Work

Our work has practical and theoretical implications. The binding energy is an important quantity for implementing TMDCs in optoelectronic devices. Additionally, experimentally obtained excited exciton state transition energies offer a means for testing the accuracy of theoretical models.

There are many related topics still to be explored. The first, very simply, is low temperature PLE measurements on suspended samples. We expect that we would see more of the Rydberg series, as was the case with low temperature reflectance contrast measurements. It would also be interesting to see if WSe₂ and MoSe₂ samples have excited exciton features in their PLE spectra. Finally, we plan to investigate the sensitivity of the binding energy to the dielectric environment.

Chapter 4

Interlayer Interactions in WS₂/Graphene Heterostructures

In this chapter, we will discuss the interlayer interactions in WS₂ and graphene vertically stacked heterostructures. First, we will describe the samples and how they are prepared. Next, we will present the photoluminescence, Raman, and reflectance contrast experimental results on the heterostructures. In particular, we will focus on the graphene layer number dependence of these measurements and compare them with TMDC/TMDC heterostructures. We will use reflectance contrast to extract information about the rate of charge and energy transfer in heterostructures. Finally, we will explain the implications of our results and describe ongoing and future experimental plans.

4.1 Samples

In this section, we will describe the method used to create our heterostructure samples, depicted in Figure 4.1 and Appendix B. First, we exfoliate monolayer WS_2 onto a fused silica substrate. The thickness of the WS_2 flake is verified by Raman, PL, and reflectance contrast spectroscopy. Next, we exfoliate graphene onto a thin film of polypropylene carbonate (PPC) transferable polymer. We identify graphene flakes from monolayer to four-layers thick using Raman and reflectance contrast spectroscopy. We transfer each graphene flake onto a monolayer WS_2 flake such that half of the WS_2 flake is covered by the graphene flake while the other half remains uncovered. We make at least two heterostructures with each graphene thickness. After the transfer, the samples are cleaned with an acetone bath followed by an IPA rinse. Reflectance contrast measurements are taken in various spots on the WS_2 flake before and after the transfer to verify that the transfer process does not alter the reflectance.

4.2 Experimental Results

In this section, we will present our experimental results on a series of WS_2 /graphene heterostructures. First, we will discuss the quenching of the WS_2 photoluminescence when capped with graphene. Next, we will compare the Raman spectrum of graphene on and off of monolayer WS_2 . Finally, we will present reflectance contrast measurements on the heterostructure and component flakes. Specifically, we will explore the broadening of the excitonic features of WS_2 in the heterostructure reflectance contrast spectrum. We will relate the broadening to the exciton coherence lifetime and track the graphene-thickness dependence. We will compare our WS_2 /graphene results with

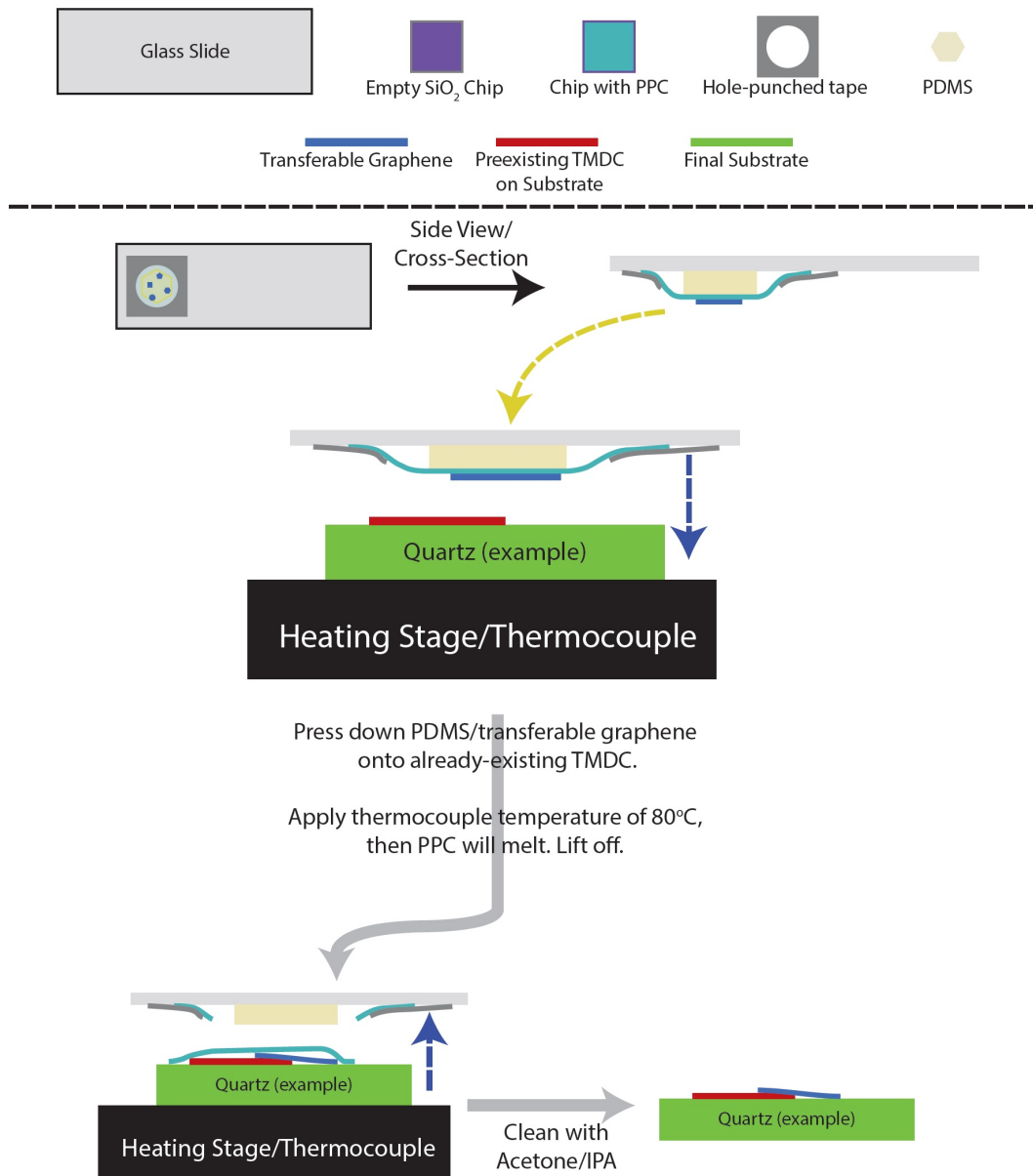


Figure 4.1: Schematic depiction of the polymer transfer technique used to assemble heterostructures. In brief, a flake is exfoliated onto PPC (see Appendix B) then transferred onto another flake. The flake on polymer is aligned onto the flake on the substrate. After making contact, the polymer is melted then rinsed off.

reflectance contrast measurements performed on TMDC/TMDC heterostructures.

4.2.1 Photoluminescence Quenching

We perform photoluminescence measurements using a Renishaw Raman inVia microscope and a 532 nm linearly polarized CW laser. We take PL maps on bare WS₂ (*i.e.* no graphene on top) and capped WS₂ (*i.e.* with graphene on top) regions of our samples. An example PL map is given in Figure 4.2(b). The bright tip is uncapped monolayer WS₂, and the darker red is the region capped with monolayer graphene. In Figure 4.2(a), we provide two representative PL spectra: one from the uncapped region and another from the capped region. In the inset of Figure 4.2(a), we plot the capped WS₂ spectrum with the scale selected to show the lineshape.

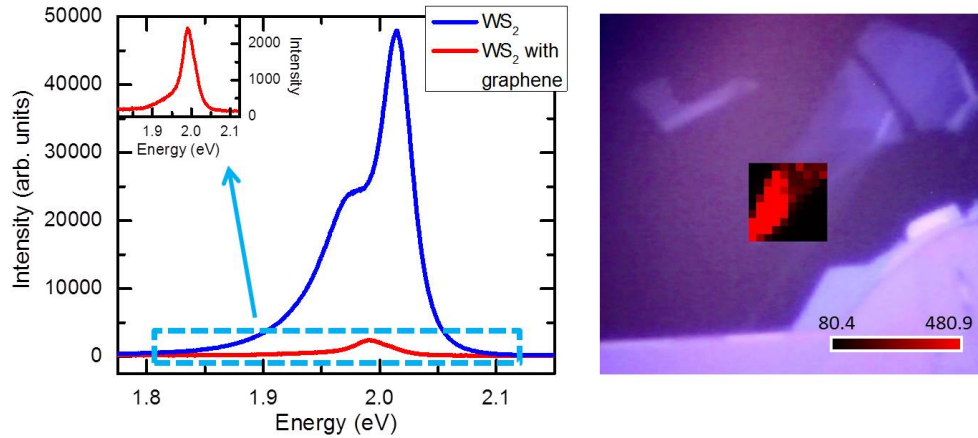


Figure 4.2: Quenching of monolayer WS₂ PL when capped with graphene. **(a)** PL spectra from monolayer WS₂ when uncapped and capped with monolayer graphene. The capped spectrum is also plotted in the inset to show the shape of the spectrum. **(b)** PL intensity map superimposed on an optical image of the sample. The bright red tip is monolayer WS₂, and the darker red region is where the WS₂ is capped with monolayer graphene. The scale bar gives the integrated intensity in arbitrary units.

The PL is quenched significantly when WS₂ is capped with graphene. To quantify the quenching, we define the quenching factor, ρ :

$$\rho = \frac{I_W}{I_{WG}} \quad (4.1)$$

Where I_W is the PL intensity of uncapped WS₂, and I_{WG} is the PL intensity of capped WS₂. For monolayer graphene on monolayer WS₂, we find a quenching factor of ~ 16 for the A exciton PL of WS₂. The quenching factor suggests an exciton coherence lifetime of about 1 ps assuming an uncapped emission lifetime of ~ 20 ps [49]. We will see in section 2.3 that this is an order of magnitude longer than the lifetime we extract from the reflectance contrast measurements. This is likely due to small pockets of imperfect contact in heterostructures; in AFM measurements on heterostructures we see tiny bubbles. In these regions of poor contact, the PL will not be quenched. Therefore, our PL measurements on the heterostructure will be disproportionately skewed by unquenched pockets, and the quenching factor from PL measurements will not be representative of the true quenching when the layers are in good contact.

We also note that the trion feature is much less pronounced in the PL spectrum from the heterostructure. For monolayer graphene capped WS₂, we find the the A trion feature has a quenching factor of ~ 42 , more that 2 times the quenching of the neutral exciton. This is likely due to static charge transfer when n-doped WS₂ is in contact with graphene. We will see a corresponding decrease in the trion feature in the reflectance contrast measurements in section 2.3.

For bilayer, trilayer, and four-layer graphene capped WS₂, we find A exciton quenching factors of ~ 14 , ~ 4 , and ~ 2.5 , respectively. This apparent decrease in

quenching is likely due to the decreasing quality of the contact from increasing rigidity of the graphene as the thickness increases.

4.2.2 Raman Spectroscopy of Graphene

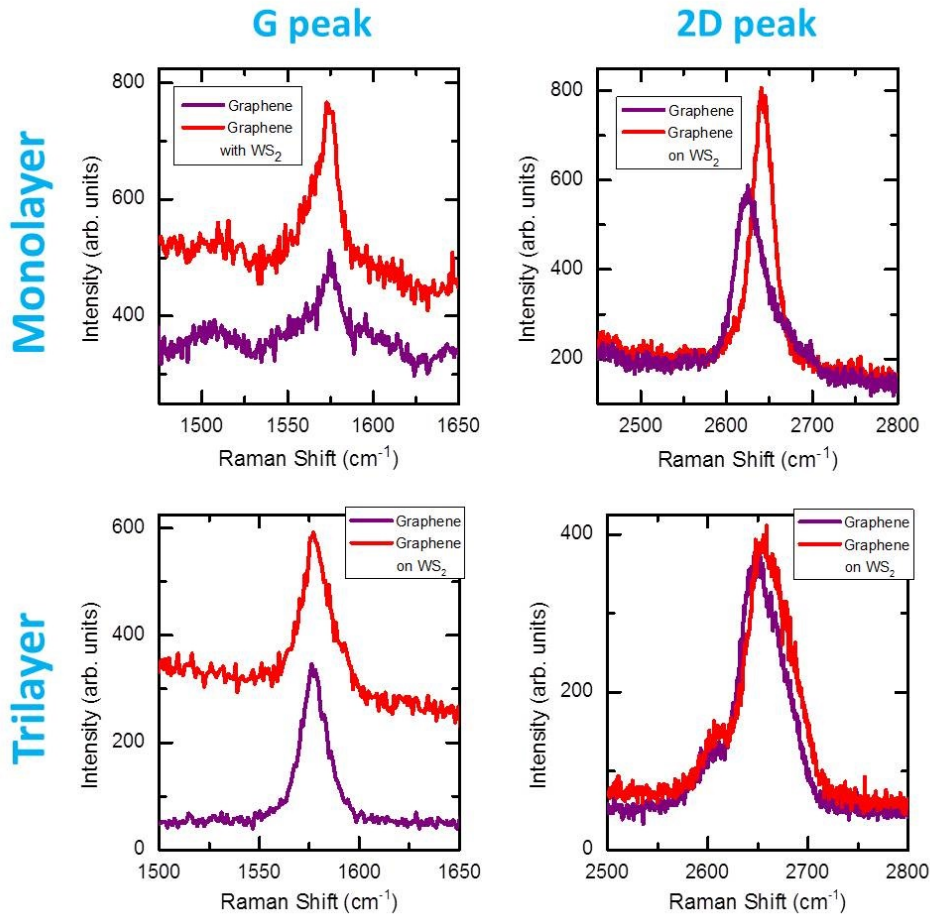


Figure 4.3: Raman spectroscopy of graphene in WS_2 /graphene heterostructures. Graphene G mode (left) and 2D mode (right) for monolayer (top) and trilayer (bottom) graphene on and off of monolayer WS_2 .

We perform Raman spectroscopy using the same laser and Renishaw inVia microscope as the PL measurements. We track the Raman modes of graphene on the

fused quartz substrate and on monolayer WS₂. In Figure 4.3, we give the Raman spectra for monolayer and trilayer graphene. The G and 2D peaks are plotted for graphene on and off of WS₂. The changes in the position and width of the Raman peaks for monolayer to four-layer thick graphene are given in Figure 4.4. We do not see a significant change in the position of the G peak, which is unexpected. The PL and reflectance contrast suggest static charge transfer, and the position of the G peak is sensitive to the doping in graphene [50]. It is possible that the change in the doping of graphene is insufficient to cause a discernible change in the energy of the G peak. We do see a shift and change in width for the 2D peak which has been associated with a change in the dielectric environment [50]. This is expected as the presence of WS₂ changes the dielectric environment.

Graphene thickness (L)	G peak shift (cm ⁻¹)	G peak change in width (cm ⁻¹)	2D peak shift (cm ⁻¹)	2D peak change in width (cm ⁻¹)
1	0 (± 1)	-1 (± 3)	14 (± 1)	-5 (± 1)
2	0 (± 1)	2 (± 3)	6 (± 2)	1 (± 1)
3	0 (± 1)	1 (± 2)	3 (± 2)	-3 (± 1)
4	0 (± 1)	4 (± 3)	2 (± 2)	2 (± 1)

Figure 4.4: Change in the peak position and width of the G and 2D modes of graphene from monolayer to four-layers thick on and off of monolayer WS₂. A positive peak shift indicates that the peak has a higher wavenumber when graphene is on WS₂ compared to on fused silica. A positive change in width indicates that the peak is wider when graphene is on WS₂. The values are given in cm⁻¹, and the numbers in parentheses are the uncertainties.

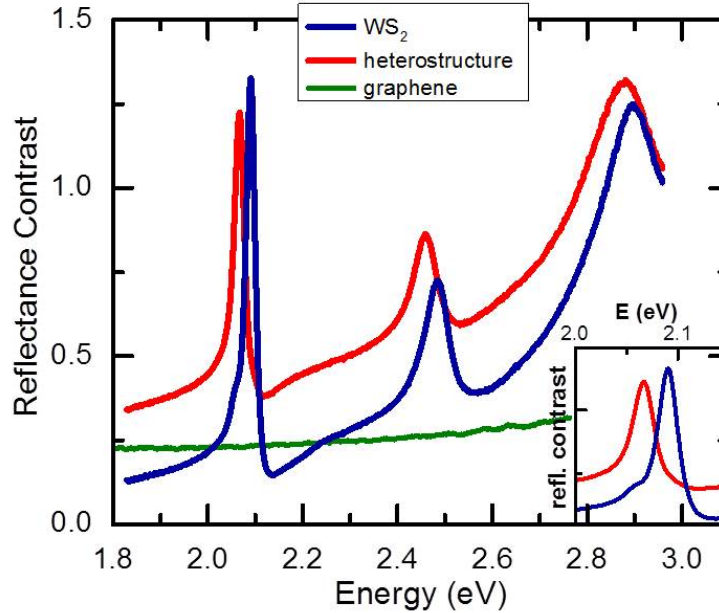


Figure 4.5: Low temperature reflectance contrast of a WS_2 /graphene heterostructure. Reflectance contrast is plotted for monolayer WS_2 (blue line), bilayer graphene (green line), and the heterostructure (red line). In the inset, we plot the A exciton feature for WS_2 and the heterostructure.

4.2.3 Reflectance Contrast of WS_2 /Graphene Heterostructures

We perform reflectance contrast on the individual layers and the heterostructure. The liquid-nitrogen cooled (~ 77 K) measurements in Figure 4.5 and the room temperature measurements in Figure 4.6 are both taken on the same sample with bilayer graphene. The essential features stay the same at room temperature, but the excitonic features are narrower when cooled.

There are a few differences between the individual layer spectra and the heterostructure spectrum. In a naïve estimation, we might expect that the heterostruc-

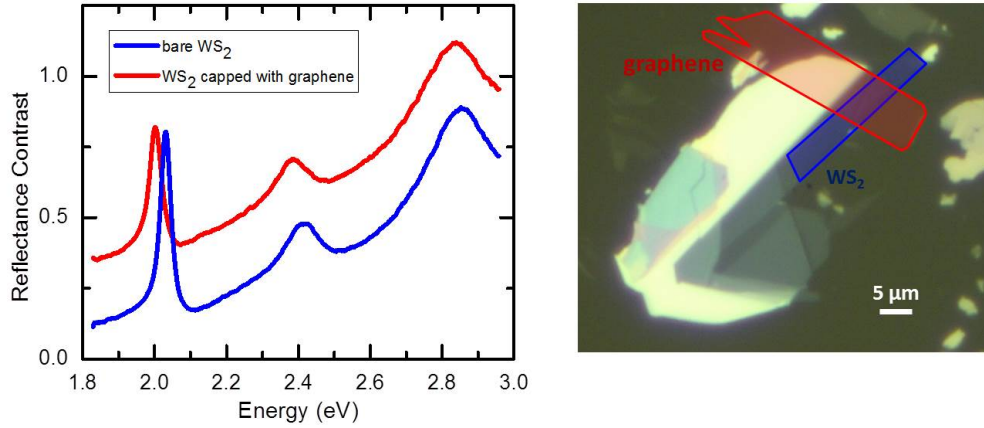


Figure 4.6: Room temperature reflectance contrast of a WS₂/graphene heterostructure. Reflectance contrast is plotted for monolayer WS₂ (blue line) and the heterostructure (red line). On the right is an optical image of the sample with the WS₂ and graphene regions indicated by outlines and shading.

ture spectrum should be similar to the sum of the two individual layer spectra. To test the reasonability of this assumption, we model the reflectance contrast for the system. First, we use dielectric functions for WS₂ and graphene that produce calculated reflectance contrast similar to our individual layer experimental results. We then sum the modeled reflectance spectra. Next, we calculate the heterostructure reflectance spectrum using the same dielectric functions for the WS₂ and graphene layers. These results are plotted in Figure 4.7. We can see that the two spectra are very similar. Therefore, in a heterostructure with negligible interlayer interactions, we would expect the heterostructure spectrum to be approximately the same as the sum of the constituent layer spectra. Any deviation between the summed spectrum and the heterostructure spectrum would arise from interlayer interactions.

We now compare the sum of the experimental reflectance contrast spectra of the individual layers and the experimental reflectance contrast spectrum of the het-

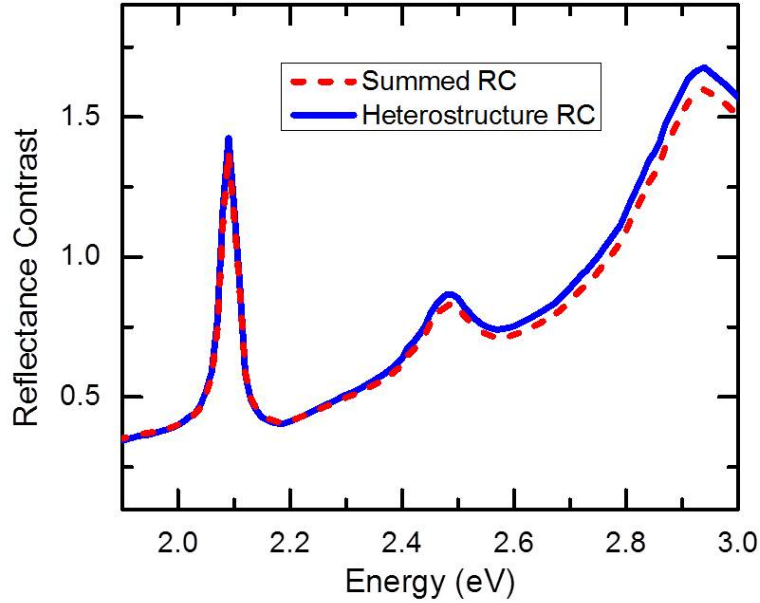


Figure 4.7: Calculated reflectance contrast of a WS_2 /graphene heterostructure. Reflectance contrast is modeled for the individual layers and the heterostructure. We plot the sum of the monolayer WS_2 and bilayer graphene calculated reflectance contrast spectra (dashed red line) and the heterostructure calculated reflectance contrast spectrum (blue line).

erostructure, see Figure 4.8. There are a few notable differences in the heterostructure spectrum: consistent spectral redshift, reduction of the trion, and broadening of the excitonic features. The spectral redshift is likely due to bandgap renormalization and change in the exciton binding energy due to dielectric screening. This effect is still under investigation, but preliminary results suggest we are able to track the 2s and 3s states of the WS_2 A exciton in the reflectance contrast of the heterostructure to obtain the bandgap and binding energy (as done in Chapter 3).

In the low-temperature WS_2 reflectance contrast, we can see a small peak on the low energy shoulder of the A exciton. This peak is from the trion (electron-electron-

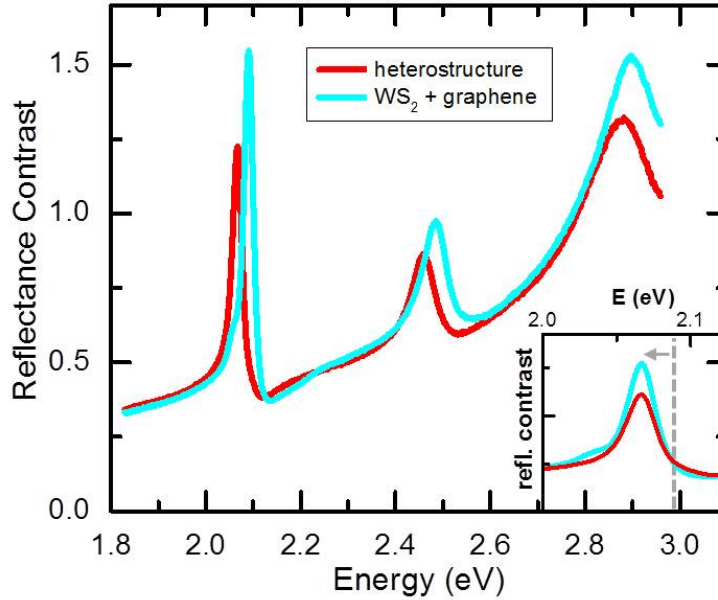


Figure 4.8: Sum of the experimental reflectance contrast of monolayer WS_2 and bilayer graphene (cyan line) and the experimental reflectance contrast of the heterostructure (red line). The inset shows the A exciton feature with the summed spectrum shifted.

hole bound state); the trion is much clearer in the derivative of the reflectance contrast as in Figure 4.9. In the derivative of the reflectance contrast of the heterostructure, we no longer see a feature indicative of the trion. This is compatible with our PL results. It is likely the result of reduced doping in WS_2 from static charge transfer as we have an n-doped WS_2 flake in contact with less-doped semimetal graphene. It is unclear why the change in the doping of graphene is not perceptible in the Raman spectrum.

In the inset of Figure 4.8, we can see that the width of the A exciton feature increases slightly when in contact with graphene. To quantitatively examine this

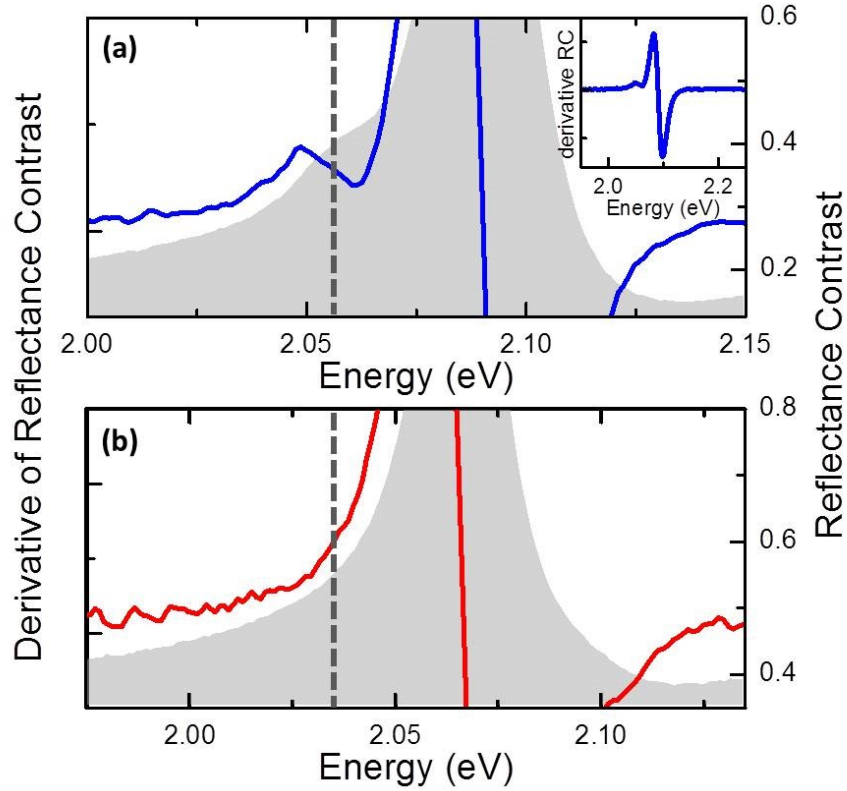


Figure 4.9: Derivative of the reflectance contrast of the monolayer WS_2 flake (top) and the heterostructure (bottom) with the reflectance contrast as a grey shaded area. The dashed grey line indicates the position of the trion peak in the WS_2 spectrum and where we would expect the feature in the heterostructure spectrum. The inset in the top plot is the derivative of the reflectance contrast shown over a larger energy range.

broadening, we convolute the summed spectrum (after redshifting it by hand) with a Lorentzian peak and fit to the heterostructure data. The heterostructure spectrum is plotted alongside the convoluted spectrum in Figure 4.10. From the width of the Lorentzian, we are able to find the broadening of the excitonic features. For the specific spectrum in Figure 4.10, we find a broadening of 6.5 meV for the A exciton and 10 meV for the B exciton when in contact with bilayer graphene.

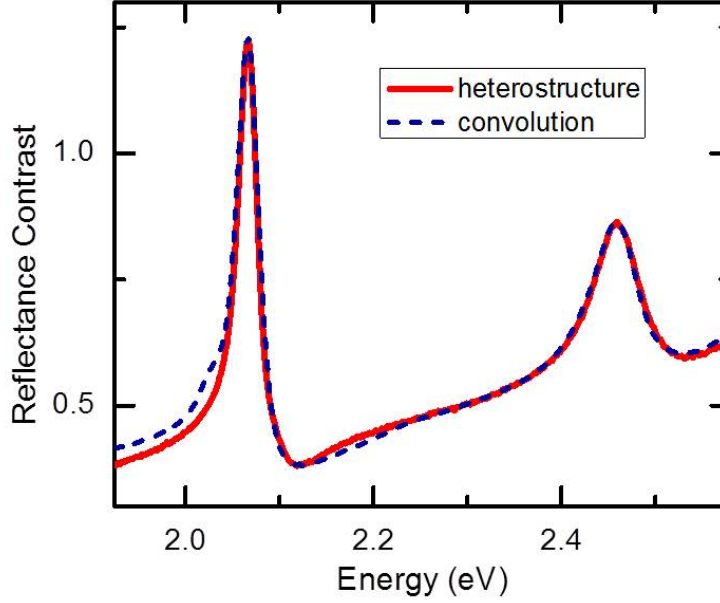


Figure 4.10: The summed reflectance contrast of monolayer WS₂ and bilayer graphene convoluted with a Lorentzian (dashed blue line) and the reflectance contrast of the heterostructure (red line).

We can relate this broadening to the coherence lifetime of the exciton with the equation:

$$\tau = \frac{\hbar}{\Delta\Gamma} \quad (4.2)$$

Where τ is the exciton coherence lifetime, and $\Delta\Gamma$ is the change in the width of the peak. From this equation we are able to obtain the lifetime of the exciton in the heterostructure. For WS₂ in contact with bilayer graphene, we find an A exciton coherence lifetime of about 100 fs.

4.2.4 Graphene Thickness Dependence

To investigate the graphene thickness dependence of the exciton coherence lifetime, we build heterostructures with graphene from one to four layers thick. For each sample we perform reflectance contrast measurements as shown in section 2.3. For all the samples we observe the same general behavior discussed in the previous section: redshift and broadening of the WS_2 excitonic features in the heterostructure. In Figure 4.11, we show the redshift of the WS_2 A and B exciton in the heterostructure as a function of the graphene thickness. There is surprisingly very little change in the redshift with increasing graphene thickness. As the graphene flake gets thicker, more of the space around the WS_2 layer would screen the exciton interactions. However, our results suggest that after the first layer of graphene the increased screening does not contribute to a significant change in the band gap or binding energy.

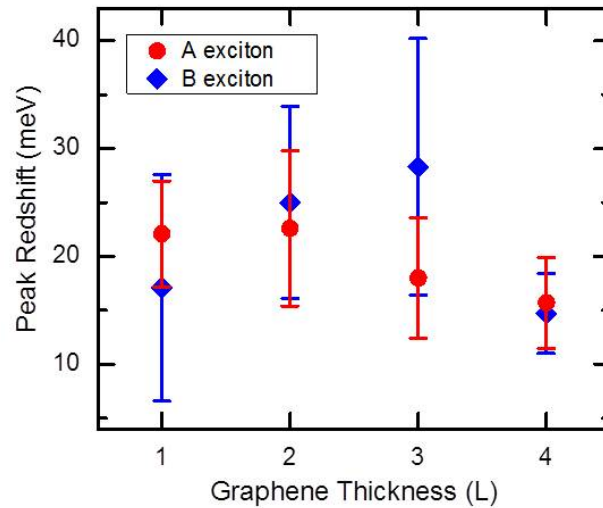


Figure 4.11: Redshift of the WS_2 A and B exciton reflectance contrast peaks in the heterostructure compared to uncapped WS_2 as a function of graphene flake thickness.

We also examine the trend in the broadening of the WS_2 A and B exciton in the heterostructure as a function of graphene thickness. We find that there is once again a very weak dependence on the thickness of the graphene, but potentially the broadening increases slightly with increasing thickness (see Figure 4.12). Additionally, the broadening of the B exciton is consistently about 5 meV more than that of the A exciton.

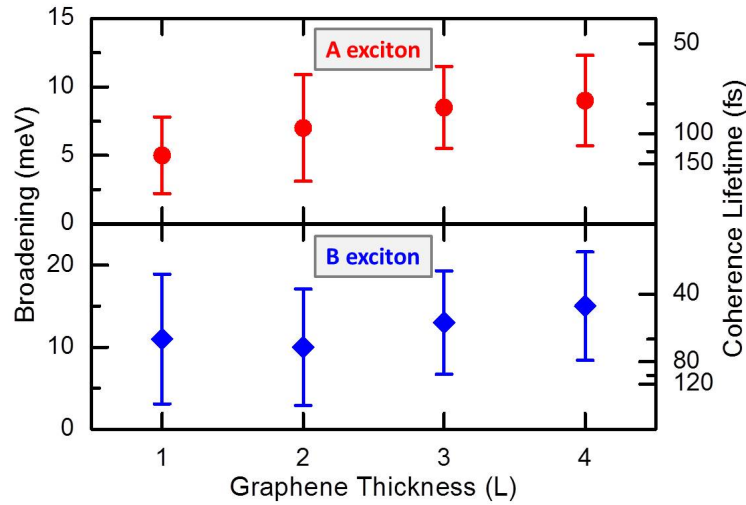


Figure 4.12: Broadening of the WS_2 A and B exciton reflectance contrast peaks in the heterostructure compared to uncapped WS_2 as a function of graphene thickness.

4.2.5 Reflectance Contrast of TMDC/TMDC Heterostructures

We will now examine heterostructures composed of monolayer TMDCs vertically stacked. We pair the materials by chalcogen, *i.e.* MoS_2 with WS_2 and MoSe_2 with WSe_2 . As in our WS_2 /graphene study, we perform reflectance contrast measurements

(see Figure 4.13) on these samples and find the heterostructure spectrum to be similar to the sum of the individual layer responses. While we do not see significant redshifts of the excitonic peaks (less than 10 meV) as we do in the $\text{WS}_2/\text{graphene}$ heterostructures, we see more significant broadening. We observe broadening of the A and B excitons in both layers of 20-35 meV, 2 or 3 times the broadening in the $\text{WS}_2/\text{graphene}$ heterostructures. Using Equation 4.2, we find an exciton coherence lifetime of 20-35 fs in TMDC/TMDC heterostructures.

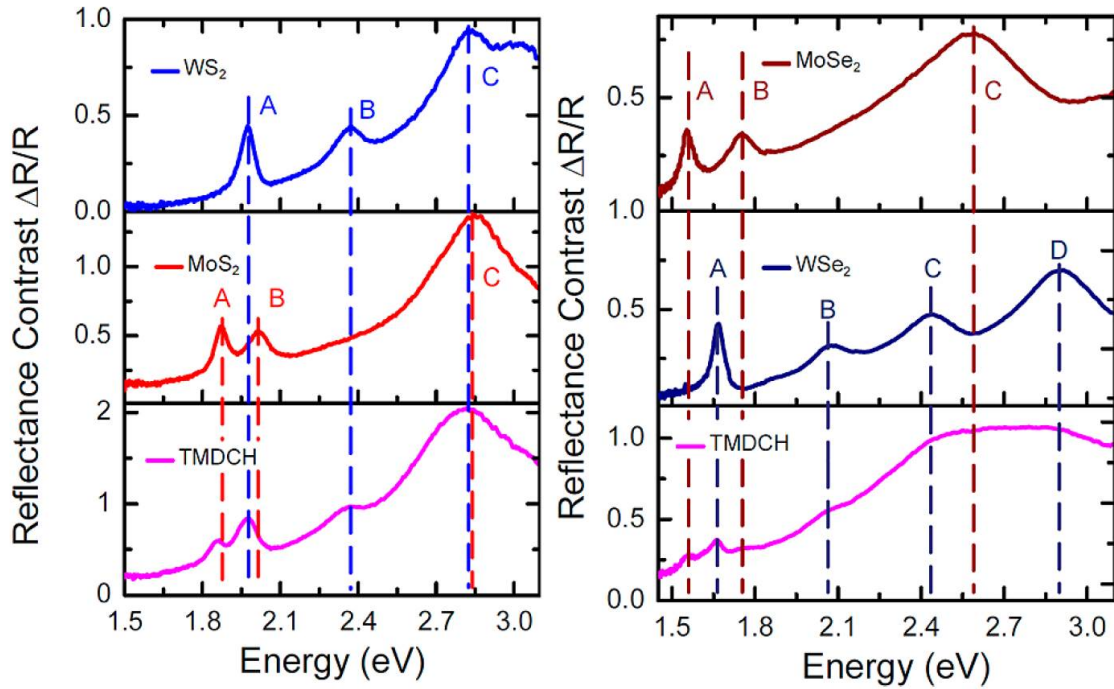


Figure 4.13: Reflectance contrast of TMDC/TMDC heterostructures [51]. **(Left)** Reflectance contrast of monolayer WS_2 , monolayer MoS_2 , and the heterostructure. **(Right)** Reflectance contrast of monolayer MoSe_2 , monolayer WSe_2 , and the heterostructure. The A and B exciton positions of the individual monolayers are indicated by dashed lines.

4.3 Sources of Broadening

In this section, we will present the possible sources of exciton peak broadening in our heterostructure reflectance contrast spectra. We will argue that the dominant sources of broadening are charge and energy transfer. We will then discuss charge and energy transfer more in depth in TMDC/graphene, TMDC/TMDC, and general 2D/2D heterostructures.

In our heterostructures, there are a few different mechanisms that could cause broadening. These possible sources of broadening are: inhomogeneous broadening, enhanced phonon broadening, change in doping, scattering within or between layers, and energy transfer. We argue that we may exclude a few of these possibilities.

First, higher inhomogeneity in the heterostructure region is doubtful since the entire sample undergoes the same processing. Therefore, we have no reason to expect more inhomogeneous broadening in the heterostructure region than the rest of the flake. Enhanced phonon broadening would be unlikely to produce the magnitude of broadening we observe. At low temperature, the phonon broadening within the layer itself is about 25 meV. Therefore, we would not anticipate an additional 10 meV broadening from a second layer. As mentioned in section 2.3, we do see indications of a change in the doping of WS_2 . However, in a previous work by Chernikov *et al.* [52] we found that a reduction in the n-doping in WS_2 , as we see in the heterostructure, leads to a narrowing of the excitonic features. Ergo, the change in doping in our system should lead to narrower peaks rather than broader peaks as we observe. Finally, we are able to exclude increased scattering within the layer from a change in the WS_2 band structure from direct to indirect gap. We do not observe indirect gap PL in the heterostructure, and theory does not predict a change in the band structure [53].

Therefore, we do not expect a significant change in the scattering within the layer. Thus, we can conclude that the broadening in WS₂/graphene heterostructures arises from charge and/or energy transfer, and the fastest that charge or energy transfer can occur in the heterostructure is the 65-130 fs time scale that we extract.

4.3.1 Energy Transfer

To estimate the rate of energy transfer we expect in our system, we use a model from a paper by Gordon and Gartstein [54]. They provide an equation for energy transfer from a point dipole to a thin dielectric slab. For a dipole at a height d above a dielectric material of thickness t , the energy transfer rate with respect to the radiative rate of the donor (Γ/Γ_0) is given by the equation:

$$\frac{\Gamma}{\Gamma_0} = \frac{3}{2(kh)^3} \text{Im} \int_0^\infty dx (x^2 e^{-2x}) \frac{(\beta^2 - 1)(1 - e^{-2x\delta t/d})}{(\beta + 1)^2 - (\beta - 1)^2 e^{-2x\delta t/d}} \quad (4.3)$$

Where h is Planck's constant, k is the donor emission wavenumber, $\beta = \sqrt{\varepsilon_{\parallel}\varepsilon_{\perp}}$, and $\delta = \sqrt{\varepsilon_{\parallel}/\varepsilon_{\perp}}$ in terms of the in-plane (ε_{\parallel}) and out-of-plane (ε_{\perp}) dielectric functions of the acceptor slab. For our system, the height d of the donor, the WS₂ exciton, is 0.325 nm which is half the thickness of a single layer of WS₂ [8]. The thickness of the acceptor is given by $h = n(0.35)$ nm, where n is the number of layers of graphene and 0.35 nm is the thickness of a single layer of graphene [55]. For our samples the average emission wavenumber of WS₂ is 617 nm. At the emission energy of WS₂, the in-plane and out-of-plane components of the dielectric function of graphene are $5.6 + 7.3i$ and 2.35, respectively [55]. The relative energy transfer rate for monolayer graphene is 1.52×10^6 , which means for a 1 ns radiative lifetime we would obtain

~ 1 fs energy transfer rate. This is 1-2 orders of magnitude faster than the rate we find from the reflectance contrast broadening. However, this energy transfer model is overly simplistic and probably inaccurate on the donor-acceptor distance scale in our system. We are able to conclude that energy transfer is likely a significant source of broadening.

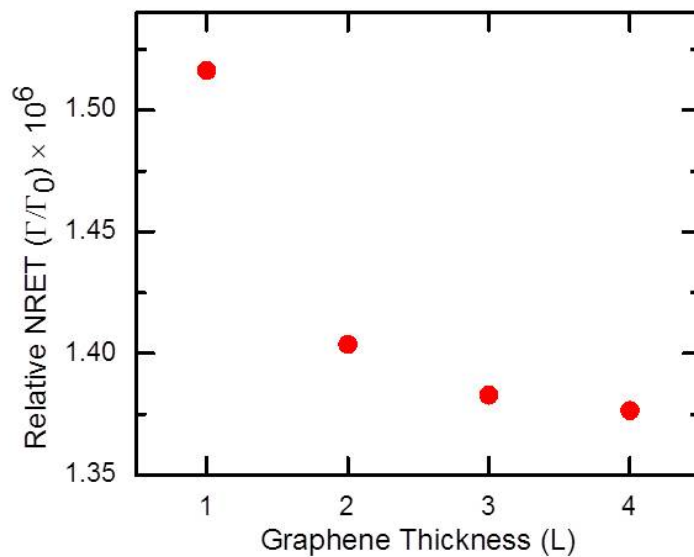


Figure 4.14: Relative energy transfer rate for monolayer WS_2 on graphene from one to four layers thick. The rate is calculated using Equation 4.3.

We calculate the relative energy transfer rate as a function of the graphene flake thickness, shown in Figure 4.14. The calculation predicts decreasing energy transfer with increasing graphene thickness. However, the change in the energy transfer with graphene thickness is not significant, much like the broadening in our samples.

4.3.2 Charge Transfer

Charge transfer is the other dominant mechanism of broadening of the excitonic features. We can imagine that tunneling from one quantum well to another that is less than a nm away should be a fairly fast process. However, the rate of charge transfer is slowed by the fact that a charge and momentum conserving charge transfer process is likely not possible in our system. Since the lattice sizes in WS_2 and graphene are different, the K-point in WS_2 and graphene correspond to different in-plane momenta. The band gap of graphene at the momentum of the K-point of WS_2 is over 5 eV. So long as the graphene Dirac point falls anywhere within the band gap of WS_2 , there would not be an energy and momentum conserving charge transfer process. Therefore, charge transfer would be a phonon-assisted process and, consequently, slower.

In TMDC/TMDC heterostructures, the broadening is almost entirely from charge transfer. For the lowest energy exciton in the heterostructure, energy transfer from that layer to the other layer is not possible as the energy of that exciton falls below the band gap of the other layer. Therefore, the broadening of the lowest energy exciton arises solely from charge transfer. We conclude that the charge transfer process in TMDC/TMDC heterostructures occurs at the fastest on a 20-35 fs time scale. In another work [56], they found an upper bound on the charge transfer time constant of 50 fs from transient absorption measurements. Thus, we have a range of 20-50 fs for the charge transfer process in TMDC/TMDC heterostructures. This is a few times faster than charge transfer could possibly occur in WS_2 /graphene heterostructures.

4.4 Conclusions

In summary, we constructed heterostructures composed of monolayer WS₂ and graphene from one to four layers thick. We performed reflectance contrast measurements on the heterostructures and observed spectral broadening of the WS₂ excitonic features when capped with graphene. This spectral broadening was attributed to charge and energy transfer between the layers. We were able to extract a lower bound on the charge and energy transfer time of 65-130 fs. These results are important for understanding the limitations and capabilities of TMDCs and graphene in devices.

In the future, we plan to perform experiments to distinguish between charge and energy transfer in TMDC/graphene heterostructures. We will accomplish this by inserting an insulating hexagonal boron nitride (BN) flake between the WS₂ and graphene layers. The BN flake will suppress charge transfer but allow energy transfer. Therefore, we can perform the same measurements, and the broadening would arise solely from energy transfer. Additionally, by building heterostructures with different BN thicknesses we can investigate the distance dependence of energy transfer between a 2D donor to a 2D acceptor (a subject of theoretical interest [57]).

Chapter 5

Scanning Tunneling Microscopy and Spectroscopy of MoS₂/WS₂ Heterostructures

In this chapter, we will investigate the band gap and band alignment of MoS₂/WS₂ heterostructures using scanning tunneling microscopy (STM) and spectroscopy (STS). We will experimentally observe the energies associated with the band edge for the conduction and valence bands in monolayer MoS₂, WS₂, and the heterostructure. From our results, we will confirm the predicted type II band alignment in the heterostructure.

First, we will describe the samples used in our measurements. Next, we will present a model of the tunneling current. Finally, we will discuss our data and its interpretation.

5.1 Samples

For our STM/STS studies, we use exfoliated flakes assembled in a vertically stacked heterostructure, like the heterostructure samples used in Chapter 4. Our samples are on fused silica to facilitate reflectance contrast measurements as well. However, unlike the samples used solely for optical studies, in order to perform STM/STS measurements the flakes need to be in contact with a conducting material. To fulfill this requirement, gold is deposited on top of the flakes to create electrical contact. An optical image of a sample as well as a schematic depiction are given in Figure 5.1. It is essential that we have heterostructures of both stacking orders, *i.e.* MoS₂ on top of WS₂ and WS₂ on top of MoS₂, as we will discuss later in this chapter.

5.1.1 Sample Preparation

In this section, we give the step by step sample fabrication process. The method has 3 general steps: exfoliate component flakes, assemble the heterostructure, and create electrical contacts. First, we exfoliate the bottom material onto a fused silica substrate and then search for sufficiently large monolayer flakes. Next, the top material in the heterostructure is exfoliated onto PPC (see Appendix B). We search the PPC for a monolayer sample of adequate size which is transferred onto the first flake using the polymer transfer technique (see Chapter 4 section 1). The thickness of the flakes is verified using Raman and PL spectroscopy. AFM is performed on the heterostructure to verify that the two materials are in good contact (see Figure 5.2).

Once we have a heterostructure, we use a chemical-free gold coating (shadow mask) method. We take a transmission electron microscopy (TEM) grid and cut it

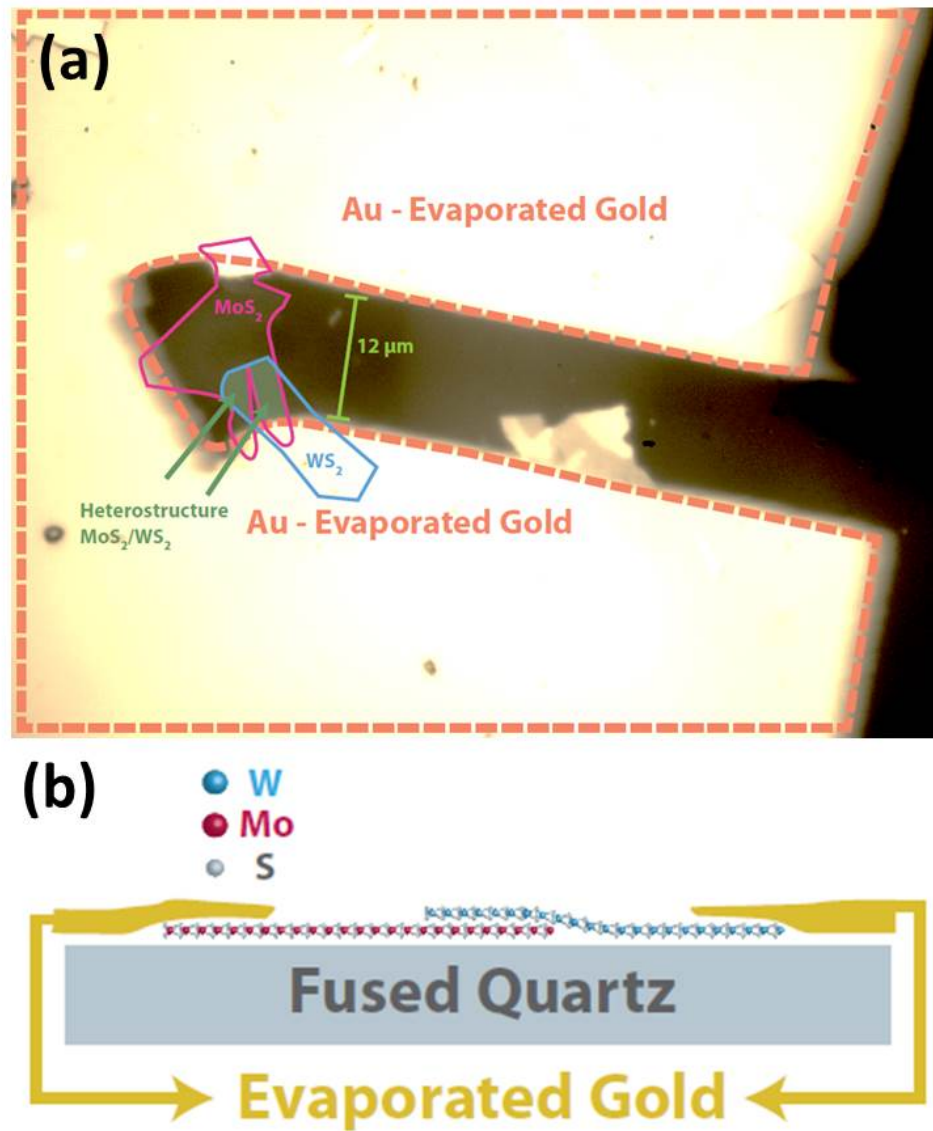


Figure 5.1: Optical image and schematic depiction of the samples. (a) Optical image of a typical sample used in our study. The MoS₂ monolayer region is indicated by a dark pink border, the WS₂ monolayer region by a blue border, and the heterostructure region is shaded lightly. The gold is indicated by a dashed light pink border. (b) Depiction of the sample from a side view. In this example, we have WS₂ (in blue) on top of MoS₂ (in pink) on fused silica. The evaporated gold contacts are shown on top of the edges of the monolayer flakes.

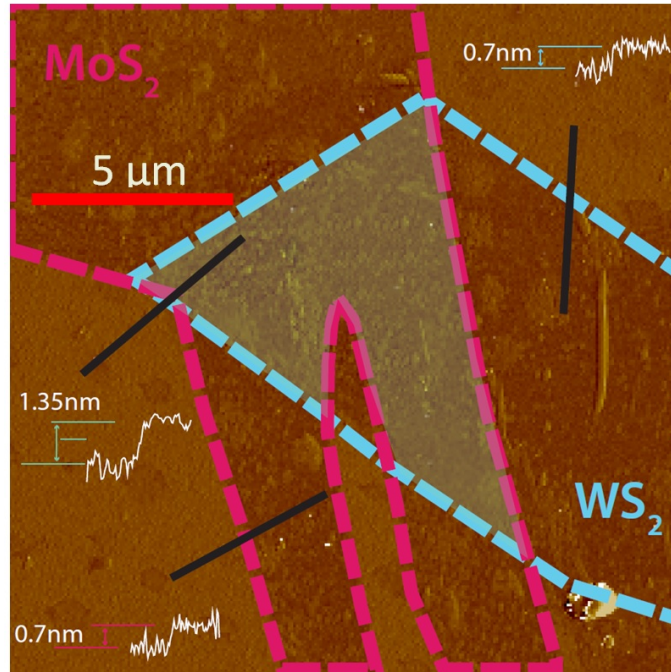


Figure 5.2: AFM image of a typical MoS₂/WS₂ heterostructure. The monolayer MoS₂ flake is outlined by a dashed pink line, the monolayer WS₂ flake is outlined by a dashed blue line, and the heterostructure region is shaded at the center.

in half with a razor. The grid serves as a shadow mask shielding a region of 10-15 μm in width. The position of the grid is controlled by placing it on a piece of PDMS which can be nudged with tweezers to move the grid with micron precision. The grid is placed such that it covers all but the edges of the flakes. Once in place, the sample and TEM grid are put into a thermal evaporator to deposit gold on the surface. After the deposition, the TEM grid is removed leaving behind an exposed (not gold coated) area that can be measured in STM/STS. The gold on the edges of the monolayer flakes will provide electrical contact. Finally, the samples are annealed for two hours in ultra-high vacuum (UHV) at 450 K. The gold deposition is depicted in Figure 5.3.

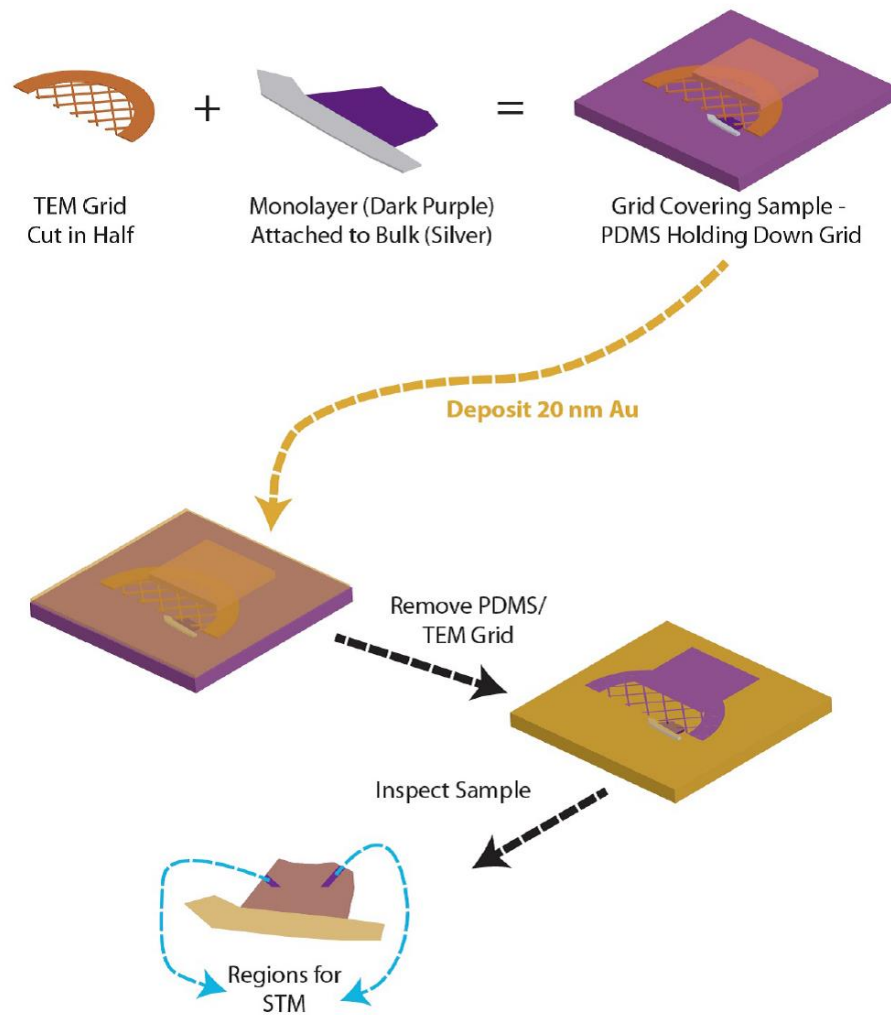


Figure 5.3: Schematic depiction of the process used to create gold contacts on our samples. The basic steps are: cut a TEM grid, place it over the sample, and evaporate gold onto the surface.

5.2 STS Model

While the onset of tunneling current is fairly obvious by eye in the STS measurements, to extract the band gap with reasonable accuracy we need a model of the tunneling current to fit to the experimental data. In the first subsection, we will summarize the

essential elements of the model we will use for the tunneling current. In the following two subsections, we will provide two corrections to the model. First, we will discuss the thermal broadening of the gap. Second, we will present a model of the tip-induced band bending. We will estimate the scale of both effects in our measurements.

5.2.1 Model of Tunneling Current

To model the tunneling current at the K/K'-point in monolayer TMDCs, we use the Bardeen approach. In the Bardeen approach, the tunneling current out of the sample is given by the equation:

$$I = \frac{4\pi e}{\hbar} \int_{-\infty}^{\infty} \left(\frac{1}{1 + e^{\frac{\varepsilon - eV}{kT}}} - \frac{1}{1 + e^{\frac{\varepsilon}{kT}}} \right) \rho_S(E_F - eV + \varepsilon) \rho_T(E_F + \varepsilon) T(z, V) d\varepsilon \quad (5.1)$$

Where ρ_S is the local density of states (LDOS) of the sample, ρ_T is the LDOS of the conducting tip, and T is the tunneling probability. The first term in parentheses, for simplicity we will refer to this term as f , provides the thermal broadening (discussed in depth in section 2.2). In low temperature measurements, f is approximately a constant.

The tunneling probability can be found using a model of an electron in a one-dimensional quantum well. From this simple model, we can write the tunneling probability in the form:

$$T \sim e^{-2z\sqrt{\frac{2m}{\hbar^2} \left(\frac{\Phi_S + \Phi_T}{2} - \frac{|eV|}{2} + E \right)}} \quad (5.2)$$

Where z is the height of the tip, m is the free electron mass, Φ_S is the work function of the sample, Φ_T is the work function of the tip, V is the bias voltage, and E is the energy of the electron. The energy of the electron depends on the in-plane momentum,

k_{\parallel} , and effective mass of the electron, m^* : $E = \frac{\hbar^2 k_{\parallel}^2}{2m^*}$. Therefore, the larger the in-plane momentum the lower the tunneling probability. The momentum dependence of the tunneling probability will be an important consideration in analyzing the data from TMDCs.

The quantity of interest is typically the change in the tunneling current as a function of the change in the bias voltage, dI/dV . We treat the tip LDOS as a constant allowing us to write Equation 5.1 (for the conduction band) as:

$$\frac{dI}{dV} \sim \int_{-\infty}^{\infty} \left(\left(\frac{e^{\frac{\varepsilon - eV}{kT}}}{(1 + e^{\frac{\varepsilon - eV}{kT}})^2} \right) \rho_S T + fT \frac{\partial \rho_S}{\partial V} + f \rho_S \frac{\partial T}{\partial V} \right) d\varepsilon \quad (5.3)$$

The LDOS for a single parabolic band is a step function. Therefore, the derivative of ρ_S with respect to bias voltage, $\frac{\partial \rho_S}{\partial V}$, is a delta function centered at the energy of the current onset, *i.e.* the energy of the conduction band minimum. Plugging the delta function into the second term of Equation 5.3, we can write:

$$\frac{dI}{dV} \sim \int_{-\infty}^{\infty} \left(\left(\frac{e^{\frac{\varepsilon - eV}{kT}}}{(1 + e^{\frac{\varepsilon - eV}{kT}})^2} \right) \rho_S T + f \rho_S \frac{\partial T}{\partial V} \right) d\varepsilon + [fT]_{E_{onset}} \quad (5.4)$$

Where fT is evaluated at the current onset energy, E_{onset} . We will fit Equation 5.4 to our experimental data in Chapter 5 section 3.2.

We plot and fit to the logarithm of the experimental dI/dV curve. Before we use the model to fit our experimental data, we need to consider its limitations. At higher voltages/currents our model will no longer be accurate, because we only consider tunneling from a single band. Therefore, we should only fit our model to lower current data. However, when the current is too low we need to consider the signal-to-noise ratio. To avoid high background and strong defect effects, the fitted

region begins at the voltage where the current is a factor of five higher than the average background current plus 3 sigma (standard deviation) of the background. We confine the fit to a 500 mV window to avoid the region where contributions to the tunneling current from other bands is appreciable. For the heterostructure, we need to observe two current onsets, one from each material, in either the conduction or valence band depending on the stacking orientation. In this situation the fitting range is 1 V rather than 500 mV, but otherwise the procedure is the same. All of these voltages and regions are labeled in Figure 5.4.

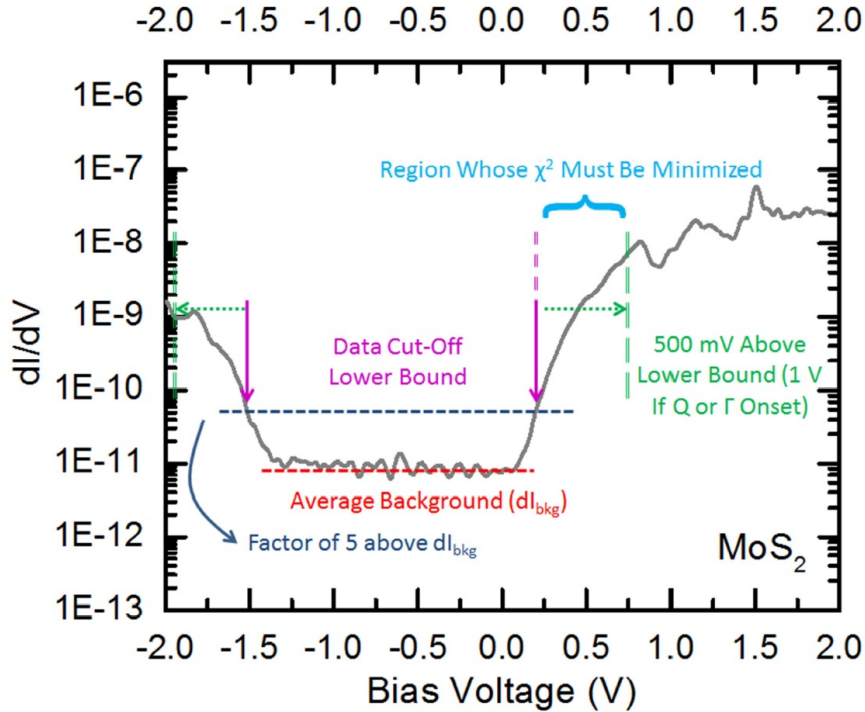


Figure 5.4: Region of the STS data to which the model is fitted. The region where the χ^2 of the model is reduced is indicated with cyan brackets and dotted green arrows.

5.2.2 Thermal Broadening

To account for thermal broadening, we follow the arguments presented by Chen [22]. As previously mentioned, the sample LDOS is a step function, and at low temperature f can be treated as a constant. Therefore, at low temperature the second derivative of the current, derivative of Equation 5.4 with respect to V , is a delta function. At room temperature with non-negligible thermal broadening, we expect the second derivative to be a peak of finite width rather than a delta function. To quantify the effect of thermal broadening, we perform the integral in Equation 5.1 assuming everything is a constant except the sample LDOS and the thermal broadening term f . The equation for the current becomes:

$$I \sim \int_{-\infty}^{\infty} \left(\frac{1}{1 + e^{\frac{\varepsilon - eV}{kT}}} - \frac{1}{1 + e^{\frac{\varepsilon}{kT}}} \right) \rho_S d\varepsilon \quad (5.5)$$

We evaluate the integral and take the second derivative with respect to bias voltage.

We obtain the equation:

$$\frac{d^2 I}{dV^2} \sim e^x \frac{(x - 2)e^x + x + 2}{(e^x - 1)^3} \quad (5.6)$$

Where $x = \frac{\varepsilon - eV}{kT}$. This equation is a peak with width $5.4kT$ (135 meV at room temperature). The width gives us the effect of thermal broadening in the energy of the band .

5.2.3 Tip-Induced Band Bending

When a bias voltage is applied to a sample, the charges will rearrange to reduce the electric field. Therefore, the actual applied voltage to the sample will be less than the voltage we measure; this is known as tip-induced band bending (TIBB). Thus, a corrective factor should be added to or subtracted from the measured voltage of the band edge. To evaluate the magnitude of TIBB, we perform calculations using SEMITIP version 6 created by R. Feenstra and the Film2 package [58, 59, 60]. The parameters we use are given in Figure 5.5. In the heterostructure calculations, we treat the bottom layer as the substrate with a relative dielectric constant of 4-6 from [61] and use the tip height of 0.6 nm from the surface. The total TIBB effect is approximately 30 meV for both monolayers and the top layer in the heterostructure. This value should be subtracted from the as-measured band gap. The bottom layer in the heterostructure only experiences 5 meV band bending, which is negligible.

5.3 Experimental Results

In this section, we will examine our STM/STS measurements on MoS₂/WS₂ heterostructures. The measurements are done at room temperature using an Omicron variable-temperature STM with mechanically-cut tungsten tips. First, we will present an example STM measurement. Next, we will provide STS measurements from heterostructures with two different stacking orientations. Finally, we will analyze the STS measurements to extract the band gap of the two individual monolayers and the band alignment in the heterostructure.

<i>Value –{MoS₂, WS₂}</i>	<i>Parameter Definition</i>
10	Tip Radius (nm)
0.6	Thickness of Total Film (nm)
0.5	Contact Potential (eV) ^{7,8}
1	Number of Different Semiconductor Regions
{2.2, 2.4}	Band Gap (eV)
{0.35, 0.3}	Conduction Band Effective Mass
0.44	Light Hole Effective Mass
{0.14, 0.4}	Spin-Orbit Splitting (eV)
1	Degeneracy Indicator (1 = Degenerate)
0	Inversion Indicator (0 = Include Possible Inversion)
4	Dielectric Constant in Film ⁹
3.8	Dielectric Constant in Substrate
300	Temperature (K)
1	Number of Different Types of Surfaces
2.00E+12	Density of Charge Carriers (cm ⁻²)

Figure 5.5: Parameters used for the TIBB calculations.

5.3.1 STM Results

The STM measurements are taken in constant current mode with a 1.5 V bias voltage (see Chapter 2 section 5 for details about STM/STS measurements). In Figure 5.6, we present a STM image of monolayer WS₂. We indicate the lattice in a few areas and provide a profile of the height to verify the lattice constant. Additionally, we show the 2D fast Fourier transform which is done using the program *Gwyddion*.

5.3.2 STS Results

STS measurements are performed in constant height mode with 80 spectra taken at different positions on each monolayer and heterostructure region. Random groups

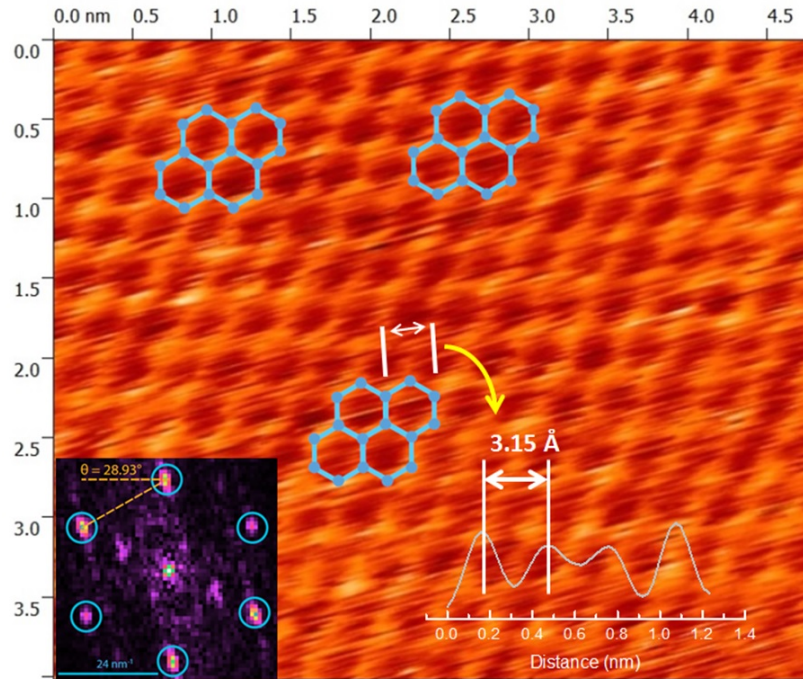


Figure 5.6: STM image of monolayer WS_2 over a 5 nm by 4 nm region. We have highlighted the lattice in a few regions with an overlay of hexagons in blue. In the bottom right, we provide a height profile along the path indicated by the double-sided arrow. In the profile, we use the maxima to verify the lattice constant. In the bottom left, we provide a 2D fast Fourier transform.

of 16 are averaged in order to improve the signal-to-noise ratio and compare reproducibility. These averaged data sets are plotted in Figure 5.7 for monolayer MoS_2 , monolayer WS_2 , and the heterostructure for a sample with MoS_2 on WS_2 (top) and a sample with WS_2 on MoS_2 (bottom).

The fitting procedure described in section 1.1 is performed for all these data sets and plotted in Figure 5.7. We use a work function of the tungsten tip of 4.5 eV and the work functions for the two TMDCs given in Figure 5.8. The fit is performed by adjusting the energy of the band edge or current onset to reduce the χ^2 . From these fits, we are able to extract the band gap for monolayer MoS_2 and WS_2 . We find

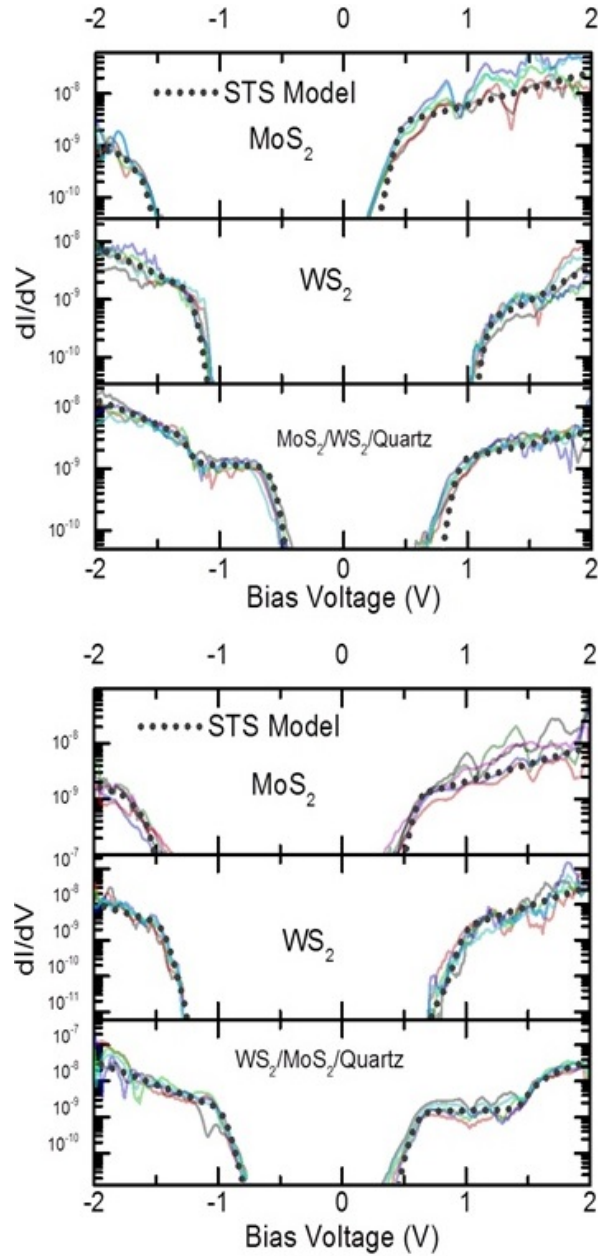


Figure 5.7: Monolayer and heterostructure STS experimental data. The top set of data is from a sample with MoS₂ on top of WS₂, and the bottom set of data is from a sample with WS₂ on top of MoS₂. The experimental data, solid lines of various colors, are averages of 16 spectra. Additionally, the model fit to the experimental data is plotted as a dotted grey line.

band gaps of 2.18 (± 0.05) eV and 2.40 (± 0.06) eV for MoS₂ and WS₂, respectively, when adjusted for TIBB.

To ensure that the observed band gap is indeed the gap of the material at the K-point, we must consider the entire band structure. In the paper by Zhang *et al.* [62], they found that the minimum at the Q-point (directly between Γ and K) in the conduction band lies close in energy to the K-point, as predicted [53, 63]. Additionally, recall that the tunneling probability depends on the in-plane momentum, as discussed in section 2.1. The in-plane momentum at the Q-point is lower than at the K-point which means that tunneling is more likely at the Q-point. In the paper by Zhang, they found that in STS measurements taken with the tip too far from the sample the current from the K-point was not be discernible, so the apparent onset of current came from the Q-point. To ensure that we performed our measurements with an appropriate tip height, we examine our MoS₂ results. In the paper by Zhang *et al.*, they measured the energy difference between the K- and Q-point in monolayer MoS₂ to be ~ 250 meV. If the current we measure in the conduction band is from the Q-point, the K \rightarrow Q gap would be the experimentally obtained 2.18 (± 0.05) eV. This would require the K \rightarrow K band gap to be less than 2 eV. Given the MoS₂ A exciton 1s transition energy of 1.86 eV, we would obtain a binding energy of ~ 100 meV. This value is dramatically less than the binding energy experimentally obtained for other TMDCs [24, 37, 39, 40] and for MoS₂ [41, 42] including our own results [30]. Therefore, we feel confident that the current onset in our measurements arises from tunneling at the K-point. Since our measurement conditions were the same for all of our measurements, we can safely assume that we are able to observe the K-point current for MoS₂, WS₂, and the top layer in the heterostructure.

5.3.3 Band Alignment

In this subsection, we will discuss the experimental observation of the band alignment in the heterostructure. To aid in this discussion, a simple diagram has been provided in Figure 5.8(a). STS measurements predominantly probe the tunneling current from the top layer. However, when the bias voltage is such that tunneling can occur only from the bottom layer, we will observe current from the bottom layer. For example, for the configuration with MoS₂ on top, in the dI/dV curves (top of Figure 5.7) we see current from the conduction and valence bands in the top layer (MoS₂). Additionally, we probe the WS₂ valence band since its energy lies within the band gap of MoS₂. In the other stacking order, we measure current from the valence and conduction band of the top layer (WS₂) and the conduction band of the bottom layer (MoS₂).

In the heterostructures, we find band gaps of 2.16 (± 0.04) eV and 2.38 (± 0.06) eV for MoS₂ and WS₂, respectively, as the top layers. These values agree to within uncertainty with the values we find for the isolated monolayers. This is surprising as we would expect the change in the dielectric environment to lead to a change in the band gap. The negligible change in the band gap is likely due to similar dielectric functions for the TMDCs and fused silica. Additionally, we note that there is a shift in the position of the current onsets. In the paper by Ugeda *et al.* [38], they speculate that such shifts are due to electrostatic processes and charge transfer.

Now we turn our attention to the band gap of the heterostructure, *i.e.* the gap from the valence band of WS₂ to the conduction band of MoS₂. In the heterostructure with MoS₂ on top we find a gap of 1.45 (± 0.06) eV, but in the heterostructure with WS₂ on top we find a band gap of 1.56 (± 0.06) eV. There is an apparent discrepancy between the two heterostructure band gap values. However, we must

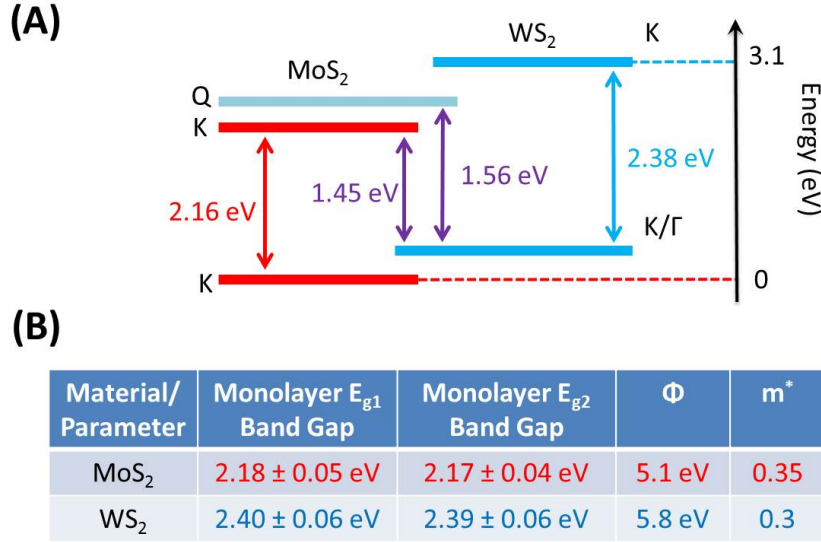


Figure 5.8: Experimental band gaps and band alignment in MoS₂/WS₂ heterostructures. **(a)** Schematic diagram of the experimental band gaps and band alignment in the heterostructure. MoS₂ is in red, WS₂ in cyan, and the heterostructure band gap in purple. The energy between the K- and Q-point in the MoS₂ conduction band is also given. **(b)** Table of the measured band gaps from the two samples, work function, effective mass, and K-point in-plane momentum for MoS₂ and WS₂.

consider tunneling from other points in the band structure as we did in the monolayer case. For the top layer we see the same band gap as the isolated monolayer, so we must be probing the K-point. For the bottom layer, we are unable to observe the band gap and verify if we are probing the K-point. Additionally, the tip is twice as far from the bottom layer as the top layer and the isolated monolayers. Therefore, it is possible that the observed current comes from areas in the band with lower in-plane momentum and, consequently, higher tunneling probability; calculations from Equation 5.2. suggest the additional tip distance may lower the tunneling probability by 1-2 orders of magnitude. We must consider where the measured current may be coming from in the valence band of WS₂ and the conduction band of MoS₂ when they

are the bottom layer. For the valence band of WS_2 , we may be probing the Γ -point. However, the Γ - and K-point are calculated to be within 25 meV of one another when in a heterostructure with MoS_2 [64]. We fit the valence band current with contributions from both the Γ - and K-point but are unable to fit with two distinct onsets. Therefore, we conclude that the Γ - and K-point are degenerate to within our uncertainty. Thus, to within our experimental uncertainty the band gap for the heterostructure is 1.45 (± 0.06) eV. For the conduction band of MoS_2 , we are likely probing the Q-point. From the apparent difference in the observed heterostructure band gap, we infer that the difference in energy between the Q-point and K-point in MoS_2 when in a heterostructure with WS_2 is 110 meV.

5.4 Conclusions

In this section, we will offer our final thoughts on MoS_2/WS_2 heterostructures. First, we will summarize the chapter. Next, we will address how our results compare to other works. Finally, we will consider the implications of our results for the future of TMDC-based devices.

5.4.1 Summary

From our STM/STS measurements, we were able to report the monolayer band gap of MoS_2 and WS_2 , 2.18 (± 0.05) eV and 2.40 (± 0.06) eV, respectively. The novel result is the band alignment in WS_2/MoS_2 heterostructures. The heterostructure band gap, 1.45 (± 0.06) eV, is particularly important in light of recent reports of the charge transfer exciton [64, 65, 56, 66, 67].

5.4.2 Comparison with Other Works

Our band gap results for both MoS₂ and WS₂ agree well with those in the literature [24, 41]. We found the energy difference between the Q- and K-point in MoS₂ to be 110 meV which is less than was previously reported [62], ~ 250 meV. However, the energy of the Q-point is likely reduced when in a heterostructure.

Our value for the heterostructure band gap agrees well with theoretical predictions [53, 64]. In several different studies [64, 65, 56, 66, 67] on heterostructures epitaxially grown and assembled from exfoliated flakes, a new PL feature has been observed at ~ 1.35 eV. This luminescence has been attributed to the charge transfer exciton. If this PL is indeed from the charge transfer exciton, then the binding energy would be about 100 meV which is less than a third of the binding energy for monolayer and bilayer flakes. The lower binding energy could arise from the greater spatial separation of the electron and hole or might suggest that the PL is from a different source, such as defects.

5.4.3 Impact and Future Work

This work is an important step towards TMDC heterostructure devices. We have confirmed that we do obtain the desired type II band alignment. More importantly, we confirm that both layers remain direct gap in the heterostructure. This information will be vital in the analysis of optical and electrical characterization of the heterostructure.

Our future plans involve characterizing the new PL feature others have observed in heterostructures. Thus far, we have been unable to observe this new PL feature. However, if we are able to obtain a sample that produces this new PL peak, we

will perform temperature- and power-dependence PL measurements, PLE, and spin-resolved PL spectroscopy to characterize the PL feature, decipher its origin, and understand its formation.

Chapter 6

Conclusion

In this chapter, we will present a summary of the previous 3 chapters. Next, we will describe the related ongoing and future projects. We will then give final remarks about this field, this dissertation, and graduate school in general.

6.1 Summary

In this dissertation, we have discussed the remarkable TMDCs. Our research has focused on how excitons in TMDCs behave alone in monolayers and interacting with another layer in a heterostructure. First, we probed the exciton excited state spectrum and exciton binding energy of monolayer MoS₂ and WS₂ using reflectance contrast and photoluminescence excitation spectroscopy (PLE). Next, we examined how the lifetime of the exciton is affected by the presence of an additional layer in WS₂/graphene heterostructures and TMDC/TMDC heterostructures. Finally, to relate this change in the exciton coherence lifetime to the band structure, we performed scanning tunneling microscopy/spectroscopy (STM/STS) on MoS₂/WS₂ heterostructures.

To investigate the exciton excited state spectrum, we used two different optical spectroscopy techniques: reflectance contrast and PLE spectroscopy. We were able to observe signatures of the excited exciton states in monolayer WS₂ and monolayer MoS₂ due to the increased absorption of the layer when excited resonantly with an excited state. From the energies of the excited states, we were able to extrapolate to the band gap and obtain the binding energy by fitting our experimental data with the nonlocal screening model. We found a binding energy of 0.44 eV and 0.32 eV for monolayer MoS₂ and WS₂, respectively, which is an order of magnitude larger than the bulk material.

Next, we investigated excitonic behavior in heterostructures. We assembled monolayer WS₂/graphene heterostructures using a polymer transfer technique to place graphene flakes from one- to four-layers thick on top of exfoliated monolayer WS₂. We used reflectance contrast to infer the decrease in the coherence lifetime of the excitons in WS₂ when in contact with graphene. The broadening of the excitonic peaks in the reflectance spectrum is inversely proportional to the exciton coherence lifetime yielding a lifetime in the range of 65-130 fs with no strong dependence on the thickness of the graphene. The lifetime gives us a lower bound on the charge and energy transfer time constant between WS₂ and graphene in the heterostructure. In TMDC/TMDC heterostructures (exfoliated monolayer MoS₂ on WS₂ and MoSe₂ on WSe₂), we found a charge transfer time constant of 20-50 fs between TMDC layers.

To further investigate TMDC/TMDC heterostructures, we performed scanning tunneling microscopy and spectroscopy (STM/STS) on MoS₂/WS₂ heterostructures. Fitting a model to the dI/dV curves, we were able to observe the relative energies of the valence and conduction bands in the two materials. We verified that the het-

erostructure has type II band alignment as predicted, i.e. the valence band maximum in one material (WS_2) and the conduction band minimum in the other (MoS_2).

All of this work has contributed to the progress of TMDCs and the field of layered materials in general. Now that we understand the nature of the exciton and how it interacts with its environment, we can move towards practical application of TMDCs in real world devices.

6.2 Ongoing and Future Experiments

In this section, we will discuss ongoing and future projects related to the work presented in this dissertation. We will begin with our ongoing efforts to investigate the influence of the dielectric environment on the exciton binding energy. Next, we will present our plan to distinguish between charge and energy transfer in heterostructures. We will then outline our plans to understand interlayer excitons. Finally, we will briefly mention the other layered materials that we are optically investigating.

6.2.1 Dielectric Environment and Binding Energy

In Chapter 3, we discussed how the reduced screening and dimensionality in monolayer flakes leads to an order of magnitude higher binding energy. This is a startling example of the influence the dielectric environment can have. One advantage of 2D materials is the incredible sensitivity they have to the environment around them. We should be able to observe a change in the dielectric environment by tracking the energy of the excited exciton states as a proxy for the binding energy. We have begun a preliminary investigation using the WS_2 /graphene heterostructures from our study

in Chapter 4. In a few samples we are able to see the 2s and 3s excited states of the WS₂ A exciton and record how their energy relative to the 1s state changes with the addition of a graphene layer on top. We also plan to make heterostructures with BN on top to compare with graphene.

6.2.2 Charge vs. Energy Transfer in Heterostructures

In TMDC/TMDC heterostructures (TMDCHs), we were able to distinguish between charge and energy transfer, because the broadening of the lowest energy exciton is only due to charge transfer. However, we did not have a way to distinguish between charge and energy transfer for the higher energy excitons in TMDCHs or in WS₂/graphene heterostructures. Additionally, 2D donor to 2D acceptor resonant energy transfer is a topic of theoretical interest [57]. It would be beneficial to be able to experimentally probe solely energy transfer in our heterostructures. To accomplish this task, we are currently working on assembling heterostructures with a thin flake of insulating hexagonal boron nitride (h-BN) between the layers for both the TMDC/TMDC and WS₂/graphene heterostructures. The h-BN layer will prevent charge transfer but allow energy transfer. Once we successfully make the samples we can use reflectance contrast, as before, to observe the broadening solely from energy transfer. Additionally, by varying the thickness of the BN layer we can probe the distance dependence of energy transfer.

6.2.3 Interlayer Excitons

Some studies have observed a new low energy PL feature in TMDCHs which they attribute to a charge transfer (CT)/interlayer exciton [66, 67, 68, 69, 70]. An interlayer

exciton is an exciton with the electron and hole localized in two different layers. We have not been able to observe a new low energy PL peak in our samples, but we are working to obtain epitaxially grown CVD samples in the hope of observing this PL feature. Once we have a sample with this new PL feature, we plan to perform power- and temperature-dependence PL measurements to distinguish between defect PL and CT exciton PL. We will also use polarization-resolved PL spectroscopy to observe whether spin is conserved in the charge transfer process. We also hope to observe the orientation of the exciton dipole as in this paper [71] on excitons in monolayer and bilayer MoS₂. Finally, we will perform PLE spectroscopy to understand the formation of the CT exciton and how it relates to excess energy and relaxation pathways.

6.2.4 Other Layered Materials

There is a whole library of other layered materials worth exploring. Currently, we are using reflectance contrast to observe the band structure of one- and few-layer phosphorene, a hexagonal honeycomb lattice made of phosphorous atoms. Phosphorene research has only just begun [72, 73, 74], and monolayer phosphorene is predicted to have a visible range band gap and high mobility. If we successfully obtain reflectance contrast results, we will try to measure the exciton binding energy and other excitonic properties.

6.3 Final Remarks

It has been such an honor playing my small part in this dynamic and interesting field. I have grown so much from this experience both as a scientist and a person. I will

refrain from rehashing my acknowledgements, but I would like to reiterate how much I truly appreciate the support of my peers, collaborators, advisor, friends, and family.

I would also like to thank anyone reading this dissertation. I hope it has been an engaging and illuminating read.

Bibliography

- [1] Novoselov, K. S.; Jiang, D.; Schedin, F.; Booth, T. J.; Khotkevich, V. V.; Morozov, S. V.; Geim, A. K. “Two-dimensional atomic crystals”. *Proc. Natl. Acad. Sci. U. S. A.*, **2005**, *102*, 1045110453.
- [2] Shen, C.-C.; Hsu, Y.-T.; Li, L.-J.; Liu, H.-L. “Charge Dynamics and Electronic Structures of Monolayer MoS₂ Films Grown by Chemical Vapor Deposition”. *Applied Phys. Exp.*, **2013**, *6*, 125801.
- [3] Geim, A. K.; Novoselov, K. S. “The rise of graphene”. *Nat. Mater.*, **2007**, *6*, 183-191.
- [4] Cooper, D. R.; DAnjou, B.; Ghattamaneni, N.; Harack, B.; Hilke, M.; Horth, A.; Majlis, N.; Massicotte, M.; Vandsburger, L.; Whiteway, E.; Yu, V. “Experimental Review of Graphene”. *ISRN Condensed Matter Physics*, **2012**, *2012*, 501686.
- [5] Cao, T.; Wang, G.; Han, W.; Ye, H.; Zhu, C.; Shi, J.; Niu, Q.; Tan, P.; Wang, E.; Liu, B.; Feng, J. “Valley-selective circular dichroism of monolayer molybdenum disulphide”. *Nat. Communications*, **2012**, *3*, 887.

- [6] Mak, K. F.; Lee, C.; Hone, J.; Shan, J.; Heinz, T. F. "Atomically Thin MoS₂: A New Direct-Gap Semiconductor". *Phys. Rev. Lett.*, **2010**, *105*, 136805.
- [7] Suzuki, R.; Sakano, M.; Zhang, Y. J.; Akashi, R.; Morikawa, D.; Harasawa, A.; Yaji, K.; Kuroda, K.; Miyamoto, K.; Okuda, T.; Ishizaka, K.; Arita, R.; Iwasa, Y. "Valley-dependent spin polarization in bulk MoS₂ with broken inversion symmetry". *Nat. Nanotech.*, **2014**, *9*, 611-617.
- [8] Frindt, R. F. "Single crystals of MoS₂ several molecular layers thick". *J. Appl. Phys.*, **1966**, *37*, 1928-1929.
- [9] Neto, A. H. C.; Guinea, F.; Peres, N. M. R.; Novoselov, K. S.; Geim, A. K. "The electronic properties of graphene". *Rev. of Mod. Phys.*, **2009**, *81*, 109-162.
- [10] Klingshirn, C. F. "Semiconductor Optics"; Springer Books, New York, 4th Edition, 2012.
- [11] Ferrari, A. C.; Meyer, J. C.; Scardaci, V.; Casiraghi, C.; Lazzeri, M.; Mauri, F.; Piscanec, S.; Jiang, D.; Novoselov, K. S.; Roth, S.; Geim, A. K. "Raman Spectrum of Graphene and Graphene Layers". *Phys. Rev. Lett.*, **2006**, *97*, 187401.
- [12] Wall, M. "The Raman Spectroscopy of Graphene and the Determination of Layer Thickness". *Thermo Scientific*, **2011**, 52252.
- [13] Lee, C.; Yan, H.; Brus, L. E.; Heinz, T. F.; Hone, J.; Ryu, S. "Anomalous Lattice Vibrations of Single- and Few-Layer MoS₂". *ACS Nano*, **2010**, *4*, 2695-2700.
- [14] Berkdemir, A.; Gutiérrez, H. R.; Botello-Méndez, A. R.; Perea-López, N.; Elías, A. L.; Chia, C.-I.; Wang, B.; Crespi, V. H.; Lopez-Urías, F.; Charlier, J.-C.;

- Terrones, H.; Terrones, M. "Identification of individual and few layers of WS₂ using Raman Spectroscopy". *Sci. Reports*, **2013**, *3*, 1755.
- [15] Tonndorf, P.; Schmidt, R.; Böttger, P.; Zhang, X.; Börner, J.; Liebig, A.; Albrecht, M.; Kloc, C.; Gordan, O.; Zahn, D. R. T.; de Vasconcellos, S. M.; Bratschitsch, R. "Photoluminescence emission and Raman response of monolayer MoS₂, MoS₂, and WSe₂". *Opt. Express*, **2013**, *21* (4), 4908-4916.
- [16] Mak, K. F.; Sfeir, M. Y.; Wu, Y.; Lui, C. H.; Misewich, J. A.; Heinz, T. F. "Measurement of the optical conductivity of graphene". *Phys. Rev. Lett.*, **2008**, *101*, 196405.
- [17] Mak, K. F.; Ju, L.; Wang, F.; Heinz, T. F. "Optical spectroscopy of graphene: From the far infrared to the ultraviolet". *Solid State Comm.*, **2012**, *152*, 1341-1349.
- [18] Li, Y.; Chernikov, A.; Zhang, X.; Rigosi, A.; Hill, H. M.; van der Zande, A. M.; Chenet, D. A.; Shih, E.-M.; Hone, J.; Heinz, T. F. "Measurement of the optical dielectric function of monolayer transition-metal dichalcogenides: MoS₂, MoSe₂, WS₂, and WSe₂". *Phys. Rev. B*, **2014**, *90*, 205422.
- [19] Qiu, D. Y.; da Jornada, F. H.; Louie, S. G. "Optical spectrum of MoS₂: Many-body effects and diversity of exciton states". *Phys. Rev. Lett.*, **2013**, *111*, 216805.
- [20] Carvalho, A.; Ribeiro, R. M.; Neto, A. H. C. "Band Nesting and the Optical Response of Two-Dimensional Semiconducting Transition Metal Dichalcogenides". *Phys. Rev. B*, **2013**, *88*, 115205.

- [21] Yardley, J. T.; Hagadorn, A. "Characterization of the Chemical Nature of the Black Ink in the Manuscript of The Gospel of Jesus's Wife through Micro-Raman Spectroscopy". *Harvard Theological Review*, **2014**, *107*, 162-164.
- [22] Chen, C. J. "Introduction to Scanning Tunneling Microscopy"; Oxford University Press: New York, 2nd Edition, 2008.
- [23] Berkelbach, T. C.; Hybertsen, M. S.; Reichman, D. R. "Theory of Neutral and Charged Excitons in Monolayer Transition Metal Dichalcogenides". *Phys. Rev. B*, **2013**, *88*, 045318.
- [24] Chernikov, A.; Berkelbach, T. C.; Hill, H. M.; Rigosi, A.; Li, Y.; Aslan, O. B.; Reichman, D. R.; Hybertsen, M. S.; Heinz, T. F. "Exciton Binding Energy and Nonhydrogenic Rydberg Series in Monolayer WS₂". *Phys. Rev. Lett.*, **2014**, *113*, 076802.
- [25] Stébé, B.; Munsch, G.; Stauffer, L.; Dujardin, F.; Murat, J. "Excitonic trion X^- in semiconductor quantum wells". *Phys. Rev. B*, **1997**, *56*, 12454.
- [26] Stébé, B.; Feddi, E.; Ainane, A.; Dujardin, F. "Optical and magneto-optical absorption of negatively charged excitons in three- and two-dimensional semiconductors". *Phys. Rev. B*, **1998**, *58*, 9926.
- [27] Esser, A.; Runge, E.; Zimmermann, R.; Langbein, W. "Photoluminescence and radiative lifetime of trions in GaAs quantum wells". *Phys. Rev. B*, **2000**, *62*, 8232.

- [28] Shi, H.; Pan, H.; Zhang, Y.-W.; Yakobson, B. I. “Quasiparticle band structures and optical properties of strained monolayer MoS₂ and WS₂”. *Phys. Rev. B*, **2013**, *87*, 155304.
- [29] Beal, A.; Liang, W. “Excitons in 2H-WSe₂ and 3R-WS₂”. *J. Phys. C: Solid State Phys.*, **1976**, *9*, 2459.
- [30] Hill, H. M.; Rigosi, A. F.; Roquelet, C.; Chernikov, A.; Berkelbach, T. C.; Reichman, D. R.; Hybertsen, M. S.; Brus, L. E.; Heinz, T. F. “Observation of Excitonic Rydberg States in Monolayer MoS₂ and WS₂ by Photoluminescence Excitation Spectroscopy”. *Nano Lett.*, **2015**, *15* (5), 2992-2997.
- [31] Kozawa, D.; Kumar, R.; Carvalho, A.; Kumar, A. K.; Zhao, W.; Wang, S.; Toh, M.; Ribeiro, R. M.; Castro Neto, A. H.; Matsuda, K.; Eda, G. “Photo-carrier relaxation pathway in two-dimensional semiconducting transition metal dichalcogenides”. *Nat. Commun.*, **2014**, *5*, 4543.
- [32] Huber, R.; Schmid, B. A.; Kaindl, R. A.; Chemla, D. S. “Femtosecond THz studies of intra-excitonic transitions”. *Phys. Status Solidi B*, **2008**, *6*, 10411048.
- [33] Sun, D.; Rao, Y.; Reider, G. A.; Chen, G.; You, Y.; Brezin, L.; Harutyunyan, A. R.; Heinz, T. F. “Observation of Rapid Exciton-Exciton Annihilation in Monolayer Molybdenum Disulfide”. *Nano Lett.*, **2014**, *14*, 5625.
- [34] Berghäuser, G.; Malic, E. “Analytical approach to excitonic properties of MoS₂”. *Phys. Rev. B*, **2014**, *89*, 125309.

- [35] Steinhoff, A.; Rösner, M.; Jahnke, F.; Wehling, T. O.; Gies, C. “Influence of Excited Carriers on the Optical and Electronic Properties of MoS₂”. *Nano Lett.*, **2014**, *14* (7), 37433748.
- [36] Ramasubramaniam, A. “Large excitonic effects in monolayers of molybdenum and tungsten dichalcogenides”. *Phys. Rev. B*, **2012**, *86*, 115409.
- [37] He, K.; Kumar, N.; Zhao, L.; Wang, Z.; Mak, K. F.; Zhao, H.; Shan, J. “Tightly Bound Excitons in Monolayer WSe₂”. *Phys. Rev. Lett.*, **2014**, *113*, 026803.
- [38] Ugeda, M. M.; Bradley, A. J.; Shi, S.-F.; da Jornada, F. H.; Zhang, Y.; Qiu, D. Y.; Ruan, W.; Mo, S.-K.; Hussain, Z.; Shen, Z.-S.; Wang, F.; Louie, S. G.; Crommie, M. F. “Giant bandgap renormalization and excitonic effects in a monolayer transition metal dichalcogenide semiconductor”. *Nat. Mater.*, **2014**, *13*, 10911095.
- [39] Ye, Z.; Cao, T.; O'Brien, K.; Zhu, H.; Yin, X.; Wang, Y.; Louie, S. G.; Zhang, X. “Probing excitonic dark states in single-layer tungsten disulphide”. *Nature*, **2014**, *513*, 214218.
- [40] Wang, G.; Marie, X.; Gerber, I.; Amand, T.; Lagarde, D.; Bouet, L.; Vidal, M.; Balocchi, A.; Urbaszek, B. “Non-linear Optical Spectroscopy of Excited Exciton States for Efficient Valley Coherence Generation in WSe₂ Monolayers”. **2016**, *arXiv:1404.0056 [condmat.mtrl-sci]*; accessed Oct 3, 2014.
- [41] Zhang, C.; Johnson, A.; Hsu, C.-L.; Li, L.-J.; Shih, C.-K. “Direct Imaging of Band Profile in Single Layer MoS₂ on Graphite: Quasiparticle Energy Gap, Metallic Edge States, and Edge Band Bending”. *Nano Lett.*, **2014**, *14* (5), 24437.

- [42] Klots, A. R.; Newaz, A. K. M.; Wang, B.; Prasai, D.; Krzyzanowska, H.; Lin, J.; Caudel, D.; Ghimire, N. J.; Yan, J.; Ivanov, B. L.; Velizhanin, K. A.; Burger, A.; Mandrus, D. G.; Tolk, N. H.; Pantelides, S. T.; Bolotin, K. I. “Probing excitonic states in suspended two-dimensional semiconductors by photocurrent spectroscopy”. *Sci. Rep.*, **2014**, *4*, 6608.
- [43] Cheiwchanchamnangij, T.; Lambrecht, W. R. L. “Quasiparticle band structure calculation of monolayer, bilayer, and bulk MoS₂”. *Phys. Rev. B*, **2012**, *85*, 205302.
- [44] Feng, J.; Qian, X.; Huang, C.-W.; Li, J. “Strain-engineered artificial atom as a broad-spectrum solar energy funnel”. *Nat. Photonics*, **2012**, *6*, 866872.
- [45] Komsa, H.-P.; Krasheninnikov, A. V. “Effects of confinement and environment on the electronic structure and exciton binding energy of MoS₂ from first principles”. *Phys. Rev. B*, **2012**, *86*, 241201.
- [46] Hüser, F.; Olsen, T.; Thygesen, K. S. “How dielectric screening in two-dimensional crystals affects the convergence of excited-state calculations: Monolayer MoS₂”. *Phys. Rev. B*, **2013**, *88*, 245309.
- [47] Molina-Sánchez, A.; Sangalli, D.; Hummer, K.; Marini, A.; Wirtz, L. “Effect of spin-orbit interaction on the optical spectra of single-layer, double-layer, and bulk MoS₂”. *Phys. Rev. B*, **2013**, *88*, 045412.
- [48] Wu, F.; Qu, F.; MacDonald, A. H. “Exciton band structure of monolayer MoS₂”. *Phys. Rev. B*, **2015**, *91*, 075310.

- [49] You, Y.; Zhang, X.-X.; Berkelbach, T. C.; Hybertsen, M. S.; Reichman, D. R.; Heinz, T. F. “Observation of biexcitons in monolayer WS_2 ”. *Nat. Phys.*, **2015**, *11*, 477-481.
- [50] Yan, J.; Zhang, Y.; Kim, P.; Pinczuk, A. “Electric Field Effect Tuning of Electron-Phonon Coupling in Graphene”. *Phys. Rev. Lett.*, **2007**, *98*, 166802.
- [51] Rigosi, A. F.; Hill, H. M.; Li, Y.; Chernikov, A.; Heinz, T. F. “Probing Inter-layer Interactions in Transition Metal Dichalcogenide Heterostructures by Optical Spectroscopy: MoS_2/WS_2 and $\text{MoSe}_2/\text{WSe}_2$ ”. *Nano Lett.*, **2015**, *15*, 5033.
- [52] Chernikov, A.; van der Zande, A.; Hill, H. M.; Rigosi, A. F.; Velauthapillai, A.; Hone, J.; Heinz, T. F. “Electrical Tuning of Exciton Binding Energies in Monolayer WS_2 ”. *Phys. Rev. Lett.*, **2015**, *115*, 126802.
- [53] Komsa, H. P.; Krasheninnikov, A. V. “Electronic Structures and Optical Properties of Realistic Transition Metal Dichalcogenide Heterostructures from First Principles”. *Phys. Rev. B*, **2013**, *88*, 085318.
- [54] Gordon, J. M.; Garstein, Y. N. “Dielectric polarization, anisotropy and nonradiative energy transfer into nanometre-scale thin semiconducting films”. *J. Phys.: Condens. Matter.*, **2013**, *25*, 425302.
- [55] Weber, J. W.; Calado, V. E.; van de Sanden, M. C. M. “Optical constants of graphene measured by spectroscopic ellipsometry”. *Appl. Phys. Lett.*, **2010**, *97*, 091904.

- [56] Hong, X.; Kim, J.; Shi, S. F.; Zhang, Y.; Jin, C.; Sun, Y.; Tongay, S.; Wu, J.; Zhang, Y.; Wang, F. "Ultrafast Charge Transfer in Atomically Thin MoS₂/WS₂ Heterostructures". *Nat. Nanotechnol.*, **2014**, *9*, 682-686.
- [57] Hernández-Martínez, P. L.; Govorov, A. O.; Demir, H. V. "Förster-Type Nonradiative Energy Transfer for Assemblies of Arrayed Nanostructures: Confinement vs Stacking Dimension". *J. Phys. Chem. C*, **2014**, *118*, 4951-4958.
- [58] Feenstra, R. M. "Electrostatic Potential for a Hyperbolic Probe Tip near a Semiconductor". *J. Vac. Sci. Technol. B*, **2003**, *21*, 2080.
- [59] Feenstra, R. M.; Meyer, G.; Rieder, K.-H. "Transport limitations in tunneling spectroscopy of Ge(111)c(28) surfaces". *Phys. Rev. B*, **2004**, *69*, 081309.
- [60] Feenstra, R. M.; Gaan, S.; Meyer, G.; Rieder, K.-H. "Low-temperature tunneling spectroscopy of Ge(111)c(2x8) surfaces". *Phys. Rev. B*, **2005**, *71*, 125316.
- [61] Chang, J. W.; Register, L. F.; Banerjee, S. K. "Ballistic Performance Comparison of Monolayer Transition Metal Dichalcogenide MX₂ (M = Mo, W; X = S, Se, Te) Metal-Oxide-Semiconductor Field Effect Transistors". *J. Appl. Phys.*, **2014**, *115*, 084506.
- [62] Zhang, C.; Chen, Y.; Johnson, A.; Li, M.-Y.; Li, L.-J.; Mendell, P. C.; Feenstra, R. M.; Shih, C.-K. "Probing Critical Point Energies of Transition Metal Dichalcogenides: Surprising Indirect Gap of Single Layer WSe₂". *Nano Lett.*, **2015**, doi: 10.1021/acs.nanolett.5b01968.
- [63] Kosmider, K.; Fernandez-Rossier, J. "Electronic Properties of the MoS₂-WS₂ Heterojunction". *Phys. Rev. B*, **2013**, *87*, 075451.

- [64] Chiu, M.-H.; Zhang, C.; Shiu, H. W.; Chu, C.-P.; Chen, C.-H.; Chang, C.-Y. S.; Chen, C.-H.; Chou, M.-Y. et al. "Determination of Band Alignment in Transition Metal Dichalcogenides Heterojunctions". *Nat. Commun.*, **2015**, *6*, 7666.
- [65] Yu, Y.; Hu, S.; Su, L.; Huang, L.; Liu, Y.; Jin, Z.; Puzos, A. A.; Geohegan, D. B.; Kim, K. W.; Zhang, Y.; Cao, L. "Equally Efficient Interlayer Exciton Relaxation and Improved Absorption in Epitaxial and Nonepitaxial MoS₂/WS₂ Heterostructures". *Nano Lett.*, **2015**, *15* (1), 486491.
- [66] Rivera, P.; Schaibley, J. R.; Jones, A. M.; Ross, J. S.; Wu, S.; Aivazian, G.; Klement, P.; Ghimire, N. J.; Yan, J.; Mandrus, D. G.; Yao, W.; Xu, X. "Observation of Long-Lived Interlayer Excitons in Monolayer MoSe₂-WSe₂ Heterostructures". *Nat. Commun.*, **2015**, *6*, 6242.
- [67] Fang, H.; Battaglia, C.; Carraro, C.; Nemsak, S.; Ozdol, B.; Kang, J. S.; Bechtel, H. A.; Desai, S. B.; Kronast, F.; Unal, A. A. *et al.* "Strong Interlayer Coupling in van der Waals Heterostructures Built from Single-Layer Chalcogenides". *Proc. Natl. Acad. Sci. U.S.A.*, **2014**, doi:10.1073/pnas.1405435111.
- [68] Gong, Y.; Lin, J.; Wang, X.; Shi, G.; Lei, S.; Lin, Z.; Zou, X.; Ye, G.; Vajtai, R.; Yakobson, B. I.; Terrones, H.; Terrones, M.; Tay, B. K.; Lou, J.; Pantelides, S. T.; Liu, Z.; Zhou, W.; Ajayan, P. M. "Vertical and in-plane heterostructures from WS₂/MoS₂ monolayers". *Nat. Mater.*, **2014**, *13*, 1135-1142.
- [69] Chiu, M.-H.; Li, M.-Y.; Zhang, W.; Hsu, W.-T.; Chang, W.-H.; Terrones, M.; Terrones, H.; Li, L.-J. "Spectroscopic Signatures for Interlayer Coupling in MoS₂-WSe₂ van der Waals Stacking". *ACS Nano*, **2014**, *8* (9), 9646-9656.

- [70] Tongay, S.; Fan, W.; Kang, J.; Park, J.; Koldemir, U.; Suh, J.; Narang, D. S.; Liu, K.; Ji, J.; Li, J.; Sinclair, R.; Wu, J. "Tuning Interlayer Coupling in Large-Area Heterostructures with CVD-Grown MoS₂ and WS₂ Monolayers". *Nano Lett.*, **2014**, *14* (6) 3185-3190.
- [71] Schuller, J. A.; Karaveli, S.; Schiros, T.; He, K.; Yang, S.; Kymissis, I.; Shan, J.; Zia, R. "Orientation of luminescent excitons in layered nanomaterials". *Nat. Nanotechnol.*, **2013**, *8*, 271-276.
- [72] Tran, V.; Soklaski, R.; Liang, Y.; Yang, L. "Layer-controlled band gap and anisotropic excitons in few-layer black phosphorus". *Phys. Rev. B*, **2014**, *89*, 235319.
- [73] Zhang, S.; Yang, J.; Xu, R.; Wang, F.; Li, W.; Ghufraan, M.; Zhang, Y.-W.; Yu, Z.; Zhang, G.; Qin, Q.; Lu, Y. "Extraordinary Photoluminescence and Strong Temperature/Angle-Dependent Raman Responses in Few-Layer Phosphorene". *ACS Nano*, **2014**, *8*, 9590-9596.
- [74] Favron, A.; Gaufres, E.; Fossard, F.; Phaneuf-L'Heureux, A.-L.; Tang, N. Y.-W.; Lévesque, P. L.; Loiseau, A.; Leonelli, R.; Francoeur, S.; Martel, R. "Photooxidation and quantum confinement effects in exfoliated black phosphorus". *Nat. Mater.*, **2015**, *14*, 826-832.

Appendix A

Effective Mass Approximation

For this brief discussion on the effective mass approximation, we will borrow from the discussion presented in [10]. In order to mathematically describe a single particle, we want to create a wave packet that is a function of \mathbf{k} centered around and within a range of a specific \mathbf{k}_0 . We use a superposition of infinite Bloch waves, $e^{i\mathbf{k}\cdot\mathbf{r}}u_{\mathbf{k}}(\mathbf{r})$, where $e^{i\mathbf{k}\cdot\mathbf{r}}$ is a plane wave and $u_{\mathbf{k}}(\mathbf{r})$ has the periodicity of the lattice, *i.e.* $u_{\mathbf{k}}(\mathbf{r} + \mathbf{R}) = u_{\mathbf{k}}(\mathbf{r})$ for all lattice vectors \mathbf{R} . This wave packet will take the form,

$$\psi_{\mathbf{k}_0}(\mathbf{r}) = \sum_{\mathbf{k}} c_{\mathbf{k}} e^{i\mathbf{k}\cdot\mathbf{r}} u_{\mathbf{k}}(\mathbf{r}) \quad (\text{A.1})$$

We would like to keep \mathbf{k} fairly localized, extending only a fraction of the Brillouin zone. This requires that in real space the wavefunction will extend larger than the unit cell. This is called a Wannier function.

If we exert a force on the wave packet, we change the energy according to the equation:

$$dE(\mathbf{k}) = \mathbf{F} \cdot d\mathbf{s} = \mathbf{F} \cdot \mathbf{v}_g dt \quad (\text{A.2})$$

Where \mathbf{v}_g is the group velocity defined by:

$$v_g = \frac{1}{\hbar} \frac{dE}{dk} \quad (\text{A.3})$$

Multiplying both sides of the above equation by $\hbar dk$, we can write it in the form $dE(\mathbf{k}) = \hbar \mathbf{v}_g d\mathbf{k}$. If we plug this into Equation 1.15, we obtain:

$$\mathbf{F} = \hbar \frac{d\mathbf{k}}{dt} \quad (\text{A.4})$$

Therefore the acceleration of the wave packet, $\mathbf{a} = \frac{d\mathbf{v}_g}{dt}$, would be:

$$\mathbf{a} = \frac{1}{\hbar} \frac{\partial^2 E}{\partial k \partial t} = \frac{1}{\hbar} \frac{\partial^2 E}{\partial k^2} \frac{d\mathbf{k}}{dt} = \frac{1}{\hbar^2} \frac{\partial^2 E}{\partial k^2} \mathbf{F} \quad (\text{A.5})$$

If we compare this with the usual form of Newton's law, $\mathbf{a} = \frac{1}{m} \mathbf{F}$, we can get an equation for the effective mass of the electron and hole:

$$\frac{1}{m_{eff}} = \frac{1}{\hbar^2} \frac{\partial^2 E}{\partial k^2} \quad (\text{A.6})$$

This equation says that we can find the effective mass from the curvature of the band. Additionally, for a free electron we would recover $m_{eff} = m_0$. For a nearly parabolic band, the mass near the extrema will be approximately constant. Thus, in semiconductors we often treat the electrons and holes as free particles with the mass a constant given by equation A.6 applied to the region of the extremum. We used the effective mass approximation in the nonlocal screening model in Chapter 3.

Appendix B

Polymer Transfer Technique

To create the samples in Chapter 4 and 5, we used the polymer transfer technique. The second half of the technique, the process of transferring the flake on polymer onto the flake on the substrate, is explained and shown in Chapter 4 section 1. In Figure B1, we provide a schematic depiction of the the first half of the polymer transfer technique. We coat a silicon chip with PPC. Next, we punch a hole in a piece of scotch tape which we place on the PPC. We exfoliate as usual onto the polymer. Finally, we peel the polymer off of the silicon chip and place the polymer onto a stiffer polymer polydimethylsiloxane (PDMS).

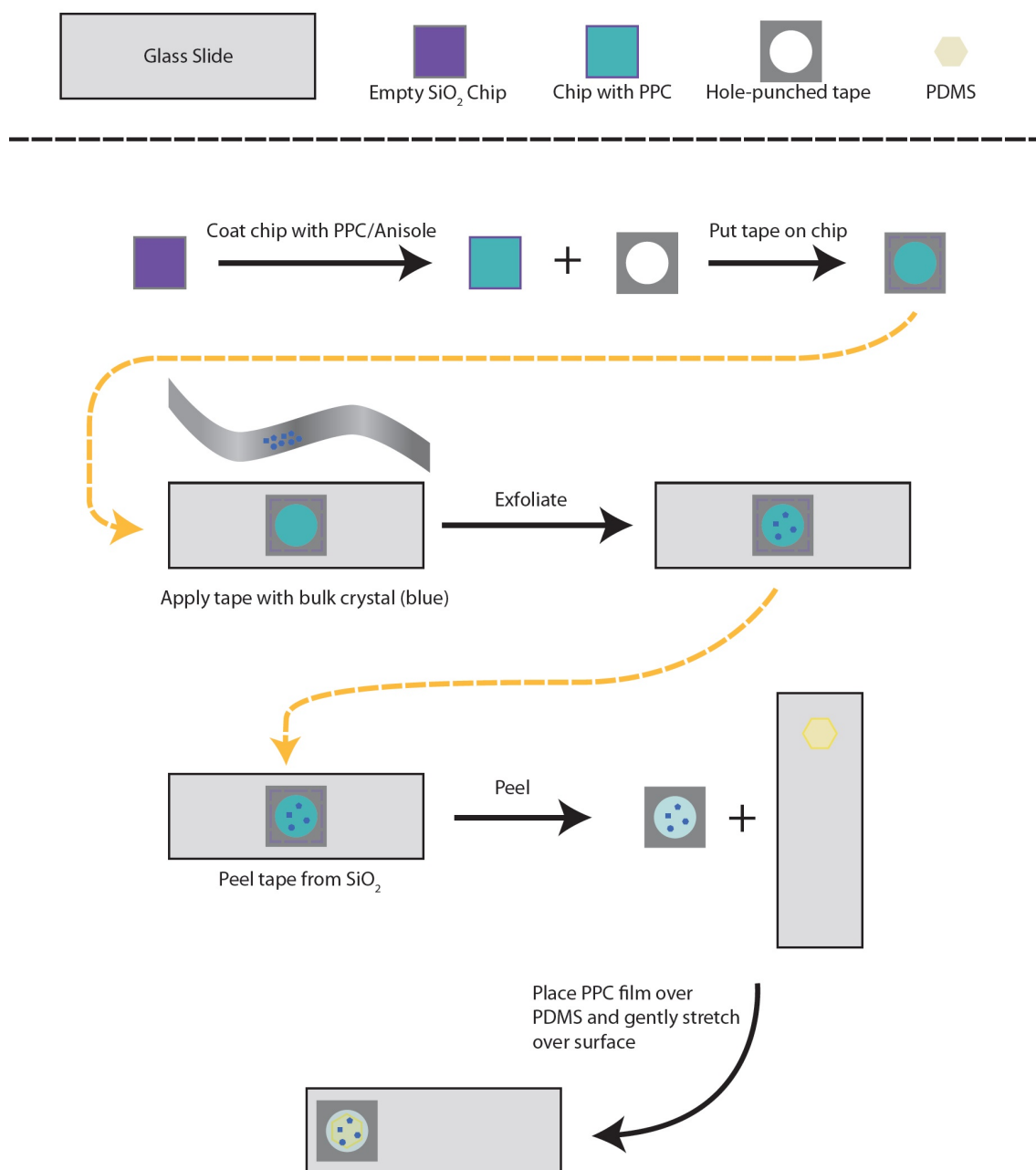


Figure B.1: Schematic depiction of exfoliating onto PPC for the polymer transfer technique used to assemble heterostructures. We coat a silicon chip with PPC, exfoliate onto the PPC, and peel and place the PPC onto PDMS